

1

2 Analysis report on the $ep \rightarrow e' p' \pi^+ \pi^-$ reaction in the CLAS
3 detector with a 2.039 GeV beam for $0.4 \text{ GeV}^2 < Q^2 < 1.0 \text{ GeV}^2$
4 and $1.3 \text{ GeV} < W < 1.825 \text{ GeV}$

5 **G. Fedotov^{a,b}, V. Burkert^c, R. Gothe^b, V. Mokeev^{a,c}, Iu. Skorodumina^{a,b}**

6 ^a*Moscow State University,
7 Vorob'evy gory, 119899 Moscow, Russia*

8 ^b*University of South Carolina,
9 712 Main Street, Columbia, South Carolina, 29208*

10 ^c*Thomas Jefferson National Accelerator Facility,
11 12000 Jefferson Avenue, Newport News, Virginia, 23606*

12

February 16, 2018

¹³ Contents

¹⁴	1 Physics motivation	4
¹⁵	2 Event selection	8
¹⁶	2.1 Particles identification	9
¹⁷	2.1.1 Electron identification	9
¹⁸	2.1.2 Hadron identification	16
¹⁹	2.1.3 Timing correction	17
²⁰	2.2 Momentum corrections	22
²¹	2.2.1 Electron momentum correction	22
²²	2.2.2 Proton momentum correction (Energy loss)	23
²³	3 Other cuts and corrections	26
²⁴	3.1 Fiducial cuts	26
²⁵	3.1.1 Fiducial cuts for negatively charged particles	26
²⁶	3.1.2 Fiducial cuts for positively charged particles	27
²⁷	3.2 Data quality check	29
²⁸	3.3 Vertex cut	31
²⁹	3.4 Exclusivity cut	35
³⁰	3.5 Missing energy cut	39
³¹	3.6 Binning and kinematical coverage	39
³²	4 Cross section calculation	43
³³	4.1 Kinematical variables	43

34	4.2	Cross section formula	50
35	4.3	Radiative corrections	53
36	4.4	Efficiency evaluation	54
37	4.5	Filling kinematical cells with zero acceptance	56
38	4.6	Combination of various topologies	59
39	5	Correction for binning effects	61
40	6	Systematical errors	64
41	6.1	Errors due to normalization, electron identification, and electron detection efficiency	64
42	6.2	Errors due to the different ways of combining topologies	65
43	6.3	Errors due to the integration over different final hadron variables	65
44	6.4	Systematical error summary	66
45	7	Conclusions	68
46	Appendix A: Measured cross sections		70
47	Bibliography		119

⁴⁹ Chapter 1

⁵⁰ Physics motivation

⁵¹ In this analysis note new set of differential and fully integrated cross sections for the exclusive
⁵² reaction $ep \rightarrow e'p'\pi^+\pi^-$ from data of the e1e run collected with the CLAS detector in
⁵³ the kinematic area of $1.3 \text{ GeV} < W < 1.825 \text{ GeV}$ and $0.4 \text{ GeV}^2 < Q^2 < 1.0 \text{ GeV}^2$ is
⁵⁴ presented. In each bin of W and Q^2 nine single-differential cross sections are obtained.
⁵⁵ They consist of: a) three distributions over invariant masses of the final hadron pairs; b)
⁵⁶ three CM-angular distributions over polar angles θ of the final π^+ , π^- , and p' , and c) three
⁵⁷ CM-angular distributions over the angles α between two planes. One plain is defined by
⁵⁸ the three-momenta of all final hadrons. Another plane is defined by the three-momenta
⁵⁹ of virtual photon and one of the final hadrons for the three different choices of this final
⁶⁰ hadron. More detailed information about kinematical variables is in Sect. 4.1. These data
⁶¹ were obtained for the first time in the kinematic area $Q^2 < 0.6 \text{ GeV}^2$ and $W > 1.55 \text{ GeV}$.
⁶² At $0.6 \text{ GeV}^2 < Q^2 < 1.0 \text{ GeV}^2$ similar $\pi^+\pi^-p$ single-differential cross sections have already
⁶³ been measured with CLAS [1]. However, in this data set these cross sections are obtained
⁶⁴ in Q^2 -bins of bin sizes, which are roughly a factor of six smaller than those achieved in [1].

⁶⁵ The studies of exclusive $\pi^+\pi^-$ electroproduction off protons represent an important avenue
⁶⁶ in the investigation of the N^* spectrum and structure via analyses of experimental data
⁶⁷ on exclusive meson electroproduction with CLAS. The CLAS detector has provided the dominant
⁶⁸ portion of all data on meson electroproduction in the resonance excitation region. The
⁶⁹ studies of transition helicity amplitudes from the proton ground state to its excited states
⁷⁰ represent a key aspect of the N^* program with CLAS [2, 3]. Data on meson electroproduction
⁷¹ off nucleons in the N^* region obtained with CLAS open an opportunity to determine
⁷² the Q^2 evolution of the $\gamma_v N \rightarrow N^*$ electrocouplings both in comparative and combined
⁷³ analyses of various meson electroproduction channels. The electroexcitation amplitudes for
⁷⁴ the low-lying resonances $\Delta(1232)3/2^+$, $N(1440)1/2^+$, $N(1520)3/2^-$, and $N(1535)1/2^-$ have
⁷⁵ been determined over a wide range of Q^2 in a comprehensive analysis of JLab-CLAS data
⁷⁶ on differential cross sections, longitudinally polarized beam asymmetries, and beam-target
⁷⁷ asymmetries for single pion electroproduction off protons [4]. Recently $\gamma_v N \rightarrow N^*$ elec-

78 electrocouplings of several higher-lying nucleon resonances: $N(1675)5/2^-$, $N(1680)5/2^+$, and
 79 $N(1710)1/2^+$ have become available for the first time for $1.5 \text{ GeV}^2 < Q^2 < 4.5 \text{ GeV}^2$ from
 80 the analysis of exclusive π^+ electroproduction off the proton [5]. Electrocouplings for the
 81 $N(1440)1/2^+$ and $N(1520)3/2^-$ resonances for $Q^2 < 0.6 \text{ GeV}^2$ have been determined from
 82 the data [6] on exclusive $\pi^+\pi^-$ electroproduction off the proton [7]. The recent analysis [8] of
 83 the CLAS data on $\pi^+\pi^-$ electroproduction off protons [1] provided the results on electrocou-
 84 plings of these states in a wider Q^2 -range up to 1.5 GeV^2 . Furthermore, electrocouplings of
 85 the $\Delta(1620)3/2^-$ resonance that decays preferentially to the $N\pi\pi$ final states have become
 86 available from this analysis for the first time. Consistent results for the $\gamma_vp \rightarrow N^*$ elec-
 87 trocouplings of the $N(1440)1/2^+$ and $N(1520)3/2^-$ resonances, that have been determined
 88 in independent analyses of the dominant meson electroproduction channels $N\pi$ and $\pi^+\pi^-p$
 89 with completely different non-resonant contributions, demonstrated the reliable extraction
 90 of these fundamental quantities. This success also supports the capability of the reaction
 91 models, that have been developed for the extraction of the resonance parameters from the
 92 analyses of data on single- [4] and double-pion [9] electroproduction off protons, to provide
 93 reliable information on the N^* parameters from independent studies of either of these major
 94 exclusive channels.

95 The CLAS results on the $\gamma_vp \rightarrow N^*$ electrocouplings [2, 4, 5, 7, 8, 10] have had a stimulat-
 96 ing impact on the theory of the excited nucleon state structure, in particular, on QCD-based
 97 approaches. The light cone sum rule (LCSR) approach [11, 12] for the first time provided
 98 access to the quark distribution amplitudes (DAs) inside the $N(1535)1/2^-$ resonance from
 99 analysis of the CLAS results on the $\gamma_vp \rightarrow N^*$ electrocouplings of this state [4]. Confronting
 100 the quark DAs of excited nucleon states determined from the experimental results on the
 101 $\gamma_vp \rightarrow N^*$ electrocouplings to the LQCD expectations, makes it possible to explore the
 102 emergence of the resonance structure starting from the QCD Lagrangian. The moments of
 103 the $N(1535)1/2^-$ quark DAs derived from the CLAS data are consistent with the LQCD
 104 expectations [12]. The Dyson-Schwinger Equations of QCD (DSEQCD) provide a concep-
 105 tually different avenue for relating the $\gamma_vp \rightarrow N^*$ electrocouplings to the fundamental QCD
 106 Lagrangian [13–15]. The DSEQCD approach allows to evaluate the contribution of the three
 107 bound dressed quarks, the so-called quark core, to the structure of excited nucleon states
 108 starting from the QCD Lagrangian. A successful description of the nucleon elastic form
 109 factors and the CLAS results on the $N \rightarrow \Delta$, $N \rightarrow N(1440)1/2^+$ electromagnetic transition
 110 form factors [2, 4, 7, 10] at photon virtualities $Q^2 > 2.0 \text{ GeV}^2$ has been recently achieved
 111 within the DSEQCD framework [13, 15, 16]. This successful description of the form factors
 112 that correspond to distinctively different structures achieved with the same dressed quark
 113 mass function strongly underlines:

- 114 • the relevance of dynamical dressed quarks with the properties predicted by the DSE-
 115 QCD approach [17] as constituents of the quark cores for the structure of the ground
 116 and excited nucleon states;
- 117 • the capability of the DSEQCD approach [13, 15] to map out the dressed quark mass

¹¹⁸ function from the experimental results on the Q^2 evolution of the nucleon elastic and
¹¹⁹ $p \rightarrow N^*$ transition form factors ($\gamma_v p \rightarrow N^*$ electrocouplings) from a combined analysis.

¹²⁰ Physics analyses of the CLAS results [4, 7, 10] on the $\gamma_v p \rightarrow N^*$ electrocouplings revealed
¹²¹ the structure of excited nucleon states at photon virtualities $Q^2 < 5.0$ GeV 2 as a complex
¹²² interplay between meson-baryon and quark degrees of freedom. The relative contributions
¹²³ from the meson-baryon cloud and the quark core are strongly dependent on the quantum
¹²⁴ numbers of the excited nucleons. Analyses of the $A_{1/2}$ electrocouplings of the $N(1520)3/2^-$
¹²⁵ resonance [18, 19] demonstrated that this amplitude is dominated by quark core contributions
¹²⁶ in the entire range of $Q^2 < 5.0$ GeV 2 measured by CLAS. However, the recent analysis [20]
¹²⁷ of the first CLAS results [5] on the $N(1675)5/2^-$ $\gamma_v p \rightarrow N^*$ electrocouplings suggested a
¹²⁸ dominance of the meson-baryon cloud. Pronounce differences in the structure of the N^* states
¹²⁹ of different quantum numbers demonstrate different manifestations of the non-perturbative
¹³⁰ strong interaction in generation of excited nucleons as the bound systems of an infinite
¹³¹ amount of quarks and gluons. The studies of $\gamma_v p \rightarrow N^*$ electrocouplings for all prominent
¹³² nucleon resonances offer unique information on many facets of the non-perturbative strong
¹³³ interaction and motivate the extension of the studies of $\gamma_v p \rightarrow N^*$ electrocouplings over full
¹³⁴ spectrum of excited nucleons.

¹³⁵ Currently the results on resonance electrocouplings in mass range above 1.6 GeV are
¹³⁶ rather limited. The recent studies of single pion electroproduction [5] delivered the results on
¹³⁷ electrocouplings of only those high mass states, which have a substantial branching fraction
¹³⁸ for decays to the $N\pi$ final states. Several high-lying nucleon excitations, as $\Delta(1620)1/2^-$,
¹³⁹ $\Delta(1700)3/2^-$, and $N(1720)3/2^+$, decay preferentially to $N\pi\pi$ final states making the channel
¹⁴⁰ of $\pi^+\pi^-$ electroproduction off the proton the major source of information on electrocouplings
¹⁴¹ of these states. In the future these electrocouplings can be checked in independent analyses
¹⁴² of KY exclusive electroproduction channels [21]. The data on electrocouplings of high-lying
¹⁴³ resonances, which decay both to the $N\pi$ and the $N\pi\pi$ final states, in $\pi^+\pi^-$ electroproduction
¹⁴⁴ channel will make it possible to test the consistency of these results with those from inde-
¹⁴⁵ pendent analyses of single pion electroproduction, offering a sensitive check of the reliability
¹⁴⁶ of the resonance parameter extraction.

¹⁴⁷ The experimental data on $\pi^+\pi^-$ electroproduction off protons presented in this analysis
¹⁴⁸ note will be analyzed within the framework of the meson-baryon reaction model JM [7–
¹⁴⁹ 9], which is currently the only available approach worldwide for the extraction of resonance
¹⁵⁰ electrocouplings from this exclusive channel. The aforementioned approach already provided
¹⁵¹ reliable results on electrocouplings of all resonances in mass range below 1.65 GeV with
¹⁵² sizable decays to the $N\pi\pi$ final states. The analysis of experimental data presented in this
¹⁵³ note eventually will allow us to:

- ¹⁵⁴ • determine the evolution of the electrocouplings of most nucleon resonances in mass
¹⁵⁵ range up to 1.825 GeV with photon virtualities Q^2 up to 1.0 GeV 2 with bin sizes in Q^2
¹⁵⁶ much smaller than previously achieved in any experiments. For high-lying resonances

157 that decay preferentially to the $N\pi\pi$ final states this information will be obtained for
158 the first time;

- 159 • explore electrocouplings of all orbital excitations ($L=1$) of the $[70,1^-]$ spin-flavor $SU(6)$ -
160 supermultiplet in a combined analysis of the results from both $N\pi$ and $N\pi\pi$ channels.

161 Studies of the combined CLAS preliminary results on $\pi^+\pi^-$ photo- and electroproduction
162 [1] within the framework of the JM meson-baryon reaction model have provided further
163 convincing evidences for the existence of the new baryon state $N'(1720)3/2^+$ [22]. So far,
164 it is the only candidate state, for which information on the internal structure has become
165 available from results on $\gamma_vp \rightarrow N^*$ electrocouplings at $Q^2 < 1.5$ GeV 2 . However, right now,
166 only four data points for this new state's electrocouplings are available. From the data of
167 this analysis note, the $N'(1720)3/2^+$ electrocoupling values will become available at the set
168 of additional Q^2 bins of bin size at least a factor of six smaller than available from the old
169 CLAS experiment [1]. The expected results will for the first time offer a deep insight to the
170 structure of the new baryon state $N'(1720)3/2^+$.

171 The expected results will extend considerably the available information on the interplay
172 between meson-baryon cloud and quark core contributions to the structure of excited nucleon
173 states in particular in mass range from 1.6 to 1.8 GeV.

¹⁷⁴ **Chapter 2**

¹⁷⁵ **Event selection**

¹⁷⁶ The data reported in this analysis were taken during the e1e run periods in the Hall B during
¹⁷⁷ November 2002 - January 2003 that included several configurations (hydrogen and deuterium
¹⁷⁸ targets as well as two different beam energies of 1 GeV and 2.039 GeV). The torus current
¹⁷⁹ was 2250 A and the mini torus current 5995 A. This particular analysis is concentrated on
¹⁸⁰ the data obtained with the 2 cm long liquid hydrogen target located at -0.2 cm along z-axis,
¹⁸¹ a 2.039 GeV polarized electron beam, and the CLAS detector. The run numbers' range of
¹⁸² this experimental setup is 36118 - 36512. There is a gap in the run numbering between runs
¹⁸³ 36160 and 36387, which coincides with Christmas and New Year of 2002-2003 and is most
¹⁸⁴ likely connected to a database server glitch (there are no entries in the database nor files
¹⁸⁵ on the silo associated with run numbers in this gap). Totally about 1.5 billion triggers over
¹⁸⁶ a month of a beamtime were accumulated. The list of full and empty target runs that are
¹⁸⁷ used in the analysis is presented in Tab. 2.1.

Full target runs	Empty target runs
36117–36122, 36125–36129, 36133–36142	35124
36144, 36145, 36147–36150, 36152–36154	36428
36156, 36158–36160, 36429–36434	36495
36437, 36441–36447, 36449, 36450	
36452–36454, 36458–36467, 36469	
36473–36478, 36480–36482, 36484–36492	
36497–36503, 36505–36511	

Table 2.1: List of the runs that are used in the analysis.

¹⁸⁸ 2.1 Particles identification

¹⁸⁹ In this analysis the first in time particle that gives signals in all four parts of the CLAS
¹⁹⁰ detector is chosen as electron candidate for each event. To identify hadrons only signals in
¹⁹¹ drift chambers and time-of-flight system are required.

¹⁹² All data accumulated during the run is stored in BOS [23] files. For all events selected
¹⁹³ for analysis the number of geometrically reconstructed particles (*gpart*) was required to be
¹⁹⁴ greater than zero. The *gpart* variable is extracted from variable *NPGP* in HEVT bank
¹⁹⁵ according to 2.1.1.

$$NPGP = (\text{Number of final reconstructed particles}) \times 100 + gpart \quad (2.1.1)$$

¹⁹⁶ One more requirement is that the status word (*stat*) is greater than zero (variable *Status*
¹⁹⁷ in EVNT bank).

¹⁹⁸ Then, as mentioned above, for electron candidates signals in all four detectors are required
¹⁹⁹ (all variables *DCStat*, *CCStat*, *SCStat*, *ECStat* from EVNT bank must be greater than
²⁰⁰ zero). For hadrons only the variables *DCStat* and *SCStat* from EVNT bank are required
²⁰¹ to be greater than zero.

²⁰² Finally the corresponding charge for all particle candidates (variable *Charge* from EVNT
²⁰³ bank) is required to be plus or minus one depending on the particle candidate's type.

²⁰⁴ 2.1.1 Electron identification

²⁰⁵ Firstly electromagnetic calorimeter (EC) and Čerenkov counter (CC) responses need to be
²⁰⁶ checked, to select good electrons from the electron candidates.

²⁰⁷ EC cuts

²⁰⁸ On the hardware level the calorimeter threshold was set to cut off events as close as possible
²⁰⁹ to the kinematic edges of the W and Q^2 domain covered by the measurement, but far enough
²¹⁰ to keep the low energy contamination within reasonable limits. To select good electrons more
²¹¹ precisely an additional calorimeter threshold cut on the software level is applied. This cut
²¹² accounts for the minimal momentum of the scattered electron that can be reconstructed
²¹³ ($P_{e'} > 0.461$ GeV) and is chosen according to [24].

²¹⁴ Then an additional cut (the so-called sampling fraction cut) was applied to eliminate in
²¹⁵ part pion contamination. To develop this cut the fact that electrons and pions have differ-
²¹⁶ ent energy deposition patterns in EC was used. An electron produces an electromagnetic
²¹⁷ shower, where the deposited energy is proportional to the electron momentum, while a π^-

as minimum ionizing particle loses a constant amount of energy per scintillator (2 MeV/cm) independently of its momentum. In Fig. 2.1 total energy deposited in EC divided by the particle momentum is shown as function of particle momentum. The six plots represent six CLAS sectors. Events between the red curves are selected as good electron candidates for further analysis. The vertical red line at $P_{e'} = 0.461$ GeV shows EC threshold cut. The upper and lower red curves are obtained in the following way: x-slices of 2D histograms are fit by Gaussians. In this way points that correspond to the positions of the fit maxima $\pm 3\sigma$ are obtained. These points determine the upper and lower boundaries for the cut. Finally, to obtain smooth curves, all points are fit by a second order polynom.

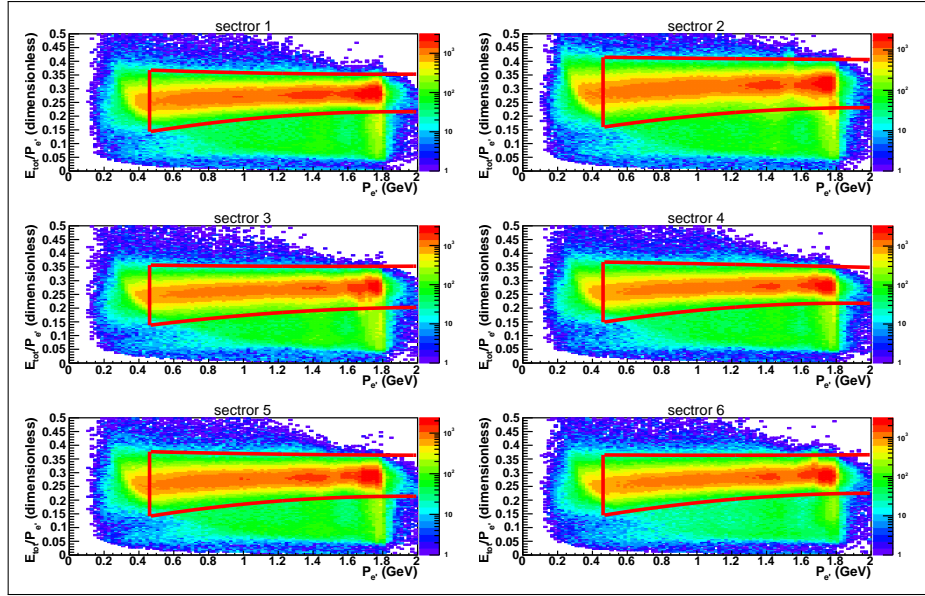


Figure 2.1: Sampling fraction distributions for the data. Six plots correspond to six CLAS sectors. Events between red curves are selected for further analysis.

Both cuts on minimal electron energy and on sampling fraction are applied both to experimental and Monte Carlo events. Since the Monte Carlo simulation does not reproduce electromagnetic showers good enough, the sampling fraction cuts for the simulation, obtained using the same procedure as for the data, look slightly different (see Fig. 2.2).

In Fig. 2.3 the energy deposited in the outer part of EC versus the energy deposited in the inner part of EC is shown before (left plot) and after (right plot) final electron identification. As it is seen in this plot the spot in the left bottom corner that corresponds to the pion contamination disappears that verifies the reliability of the electron selection.

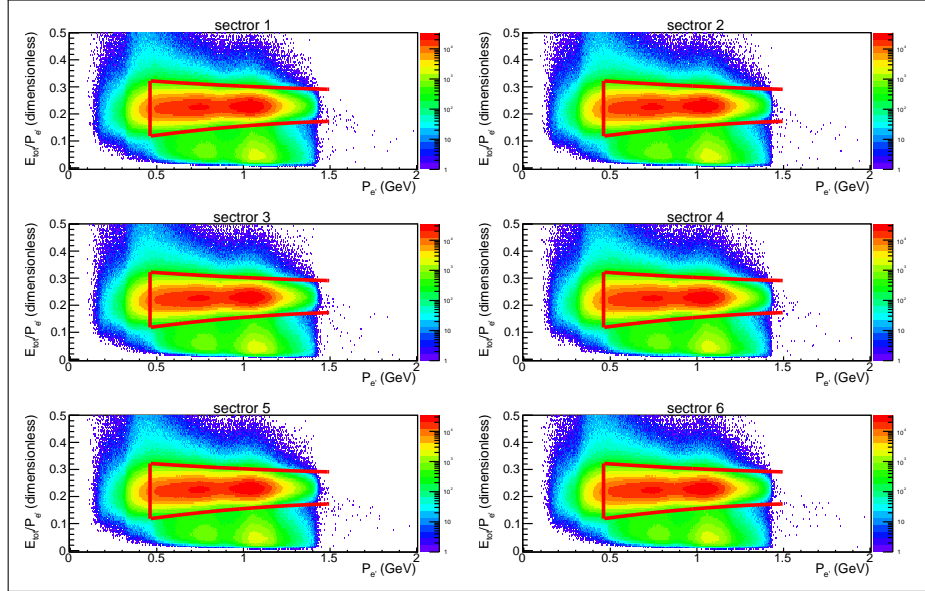


Figure 2.2: Sampling fraction distributions for Monte Carlo. Six plots correspond to six CLAS sectors. Events between red curves are selected for further analysis.

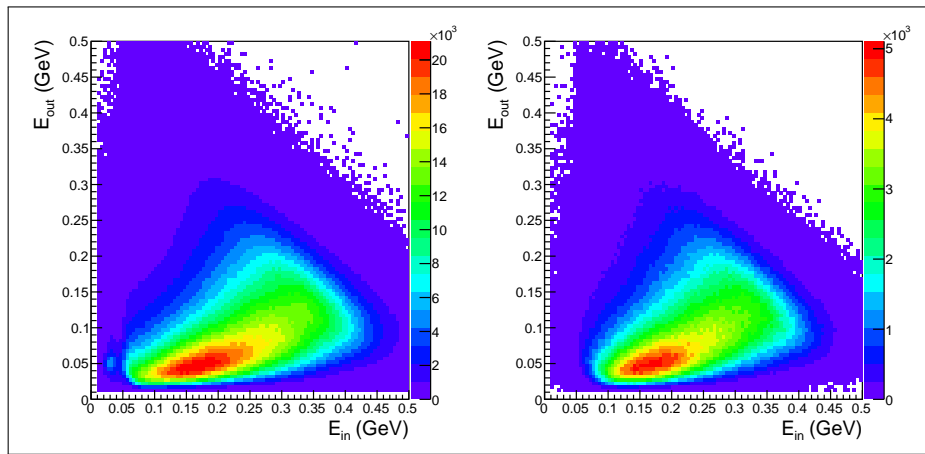


Figure 2.3: Energy deposited in the outer part of EC versus energy deposited in the inner part of EC before (left plot) and after (right plot) final electron selection.

235 CC cuts

236 To improve the quality of electron candidate selection and π^-/e^- separation a Čerenkov
 237 counter is used. In this experiment the Čerenkov counter had inhomogeneously distributed
 238 zones with partially low detection efficiency. For that purpose a geometrical cut for the
 239 removal of CC low efficiency zones is established. This cut is defined in the plane of Čerenkov
 240 counter. Since polar and azimuthal angles ($\theta_{cc}, \varphi_{cc}$) in the CC plane are not directly defined
 241 in the BOS banks [23] some calculations were made to derive these angles from variables
 242 available in DCPB bank. Fig. 2.4 illustrates these calculations.

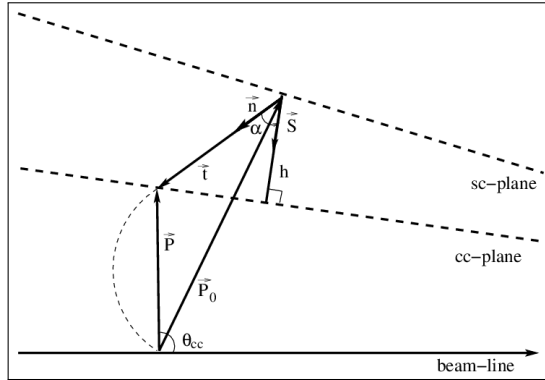


Figure 2.4: Calculation of polar θ_{cc} and azimuthal φ_{cc} angles in the CC plane using variables that are available in DCPB bank.

243 The equation 2.1.2 of the CC plane is known from [25]:

$$\begin{aligned}
 Ax + By + Cz + D &= 0, \\
 D &= 1., \\
 A &= -0.000785, \\
 B &= 0, \\
 C &= -0.00168, \\
 \vec{S} &= (A, B, C)
 \end{aligned} \tag{2.1.2}$$

244 The distance (h) from the SC hit point to the CC plane (see Fig. 2.4) is then given by

$$h = \frac{(\vec{S} \cdot \vec{P}_0) + D}{|\vec{S}|}, \tag{2.1.3}$$

245 where components of \vec{P}_0 are available in DCPB bank (x_{sc}, y_{sc}, z_{sc}). A tangent to the
 246 particle track (the track is shown by a dashed line in Fig. 2.4) at the point of intersection

²⁴⁷ with the CC plane (\vec{t}) can be written as

$$\left| \vec{t} \right| = \frac{h}{\cos(\alpha)}. \quad (2.1.4)$$

²⁴⁸ In turn $\cos(\alpha)$ can be calculated as 2.1.5.

$$\cos(\alpha) = \frac{(\vec{n} \cdot \vec{S})}{\left| \vec{S} \right|}, \quad (2.1.5)$$

²⁴⁹ where \vec{n} is a unit vector in \vec{t} -direction based on the DCPB bank variables (cx_sc, cy_sc, cz_sc).
²⁵⁰ It needs to be mentioned that there is no magnetic field between the CC and SC planes, so
²⁵¹ after hitting the CC plane the particle moves along the \vec{t} -vector.

²⁵² It is easy to see in Fig. 2.4 that the vector \vec{P} , which goes from the interaction vertex to
²⁵³ the track intersection with the CC plane, is $\vec{P} = \vec{P}_0 + \vec{t}$. Therefore, the angles θ_{cc} and φ_{cc}
²⁵⁴ can be calculated by 2.1.6 and 2.1.7, respectively.

$$\theta_{cc} = \arccos \left(\frac{P_z}{\left| \vec{P} \right|} \right) \quad (2.1.6)$$

$$\begin{aligned} \varphi_{cc} &= \arctan \left(\frac{P_y}{P_x} \right) & \text{if } P_x > 0, P_y > 0 \\ \varphi_{cc} &= \arctan \left(\frac{P_y}{P_x} \right) + 2\pi & \text{if } P_x > 0, P_y < 0 \\ \varphi_{cc} &= \arctan \left(\frac{P_y}{P_x} \right) + \pi & \text{if } P_x < 0, P_y < 0 \\ \varphi_{cc} &= \arctan \left(\frac{P_y}{P_x} \right) + \pi & \text{if } P_x < 0, P_y > 0 \\ \varphi_{cc} &= \frac{\pi}{2} & \text{if } P_x = 0, P_y > 0 \\ \varphi_{cc} &= \frac{3\pi}{2} & \text{if } P_x = 0, P_y < 0 \end{aligned} \quad (2.1.7)$$

²⁵⁵ After the angles in the CC plane are defined, distributions φ_{cc} vs. θ_{cc} are plotted for each
²⁵⁶ CLAS sector (see Fig. 2.5). The quantity 2.1.8 is shown by the color code in Fig. 2.5. This
²⁵⁷ quantity varies from zero to one and shows the portion of good electrons with number of
²⁵⁸ photoelectrons greater than five inside a $(\theta_{cc}, \varphi_{cc})$ bin. Or in other words how efficient CC
²⁵⁹ is in a given $(\theta_{cc}, \varphi_{cc})$ bin.

$$\frac{\text{number of events inside } (\theta_{cc}, \varphi_{cc}) \text{ bin with more than 5 photoelectrons in CC}}{\text{total number of events inside } (\theta_{cc}, \varphi_{cc}) \text{ bin}} \quad (2.1.8)$$

260 The edges of the distributions in Fig. 2.5 are sharp due to the fiducial cut that is applied in
 261 the CC plane 2.1.9. The shape of this cut is taken from [26].

$$\begin{aligned} \theta_{cc} &> 7.0 + 0.0032\varphi_{cc} + 0.0499\varphi_{cc}^2 \\ \left(\frac{\theta_{cc} - 45.5^\circ}{34.5^\circ}\right)^2 + \left(\frac{\varphi_{cc}}{21^\circ}\right)^2 &\leq 1 \\ \left(\frac{\theta_{cc} - 45.5^\circ}{1.75^\circ}\right)^2 + \left(\frac{\varphi_{cc}}{21^\circ}\right)^2 &> 1 \\ \theta_{cc} &< 45^\circ \end{aligned} \quad (2.1.9)$$

262 The two stripes in sector five in Fig. 2.5 correspond to the inefficient zones that will be
 263 discussed in Sec. 3.1.

264 For further analysis only zones with a ratio 2.1.8 greater than 0.8 are selected. These
 265 zones are shown in black in Fig. 2.6. As it is seen in Fig. 2.6, there is an inefficient zone in
 266 the middle of each sector, that is expected since two CC mirrors are joined there.

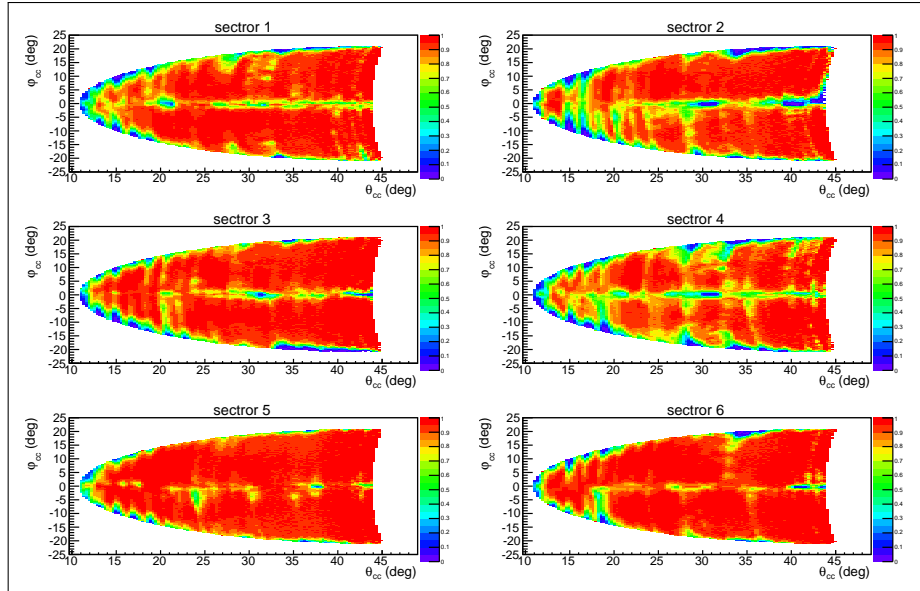


Figure 2.5: Distributions of the quantity 2.1.8 as function of the polar (θ_{cc}) and azimuthal (φ_{cc}) angles in the CC plane for six CLAS sectors.

267 After the geometrical cut shown in Fig. 2.6 is applied photoelectron distributions are
 268 plotted for each PMT on the left and right sides of each CC segment and for each CLAS
 269 sector (see Fig. 2.7). The segment number and *index* that indicates which side PMT was
 270 fired are taken from the CCPB bank *Status* variable according to

$$Status = 10 \times (\text{CC segment number}) + 1000 \times (1 + index), \quad (2.1.10)$$

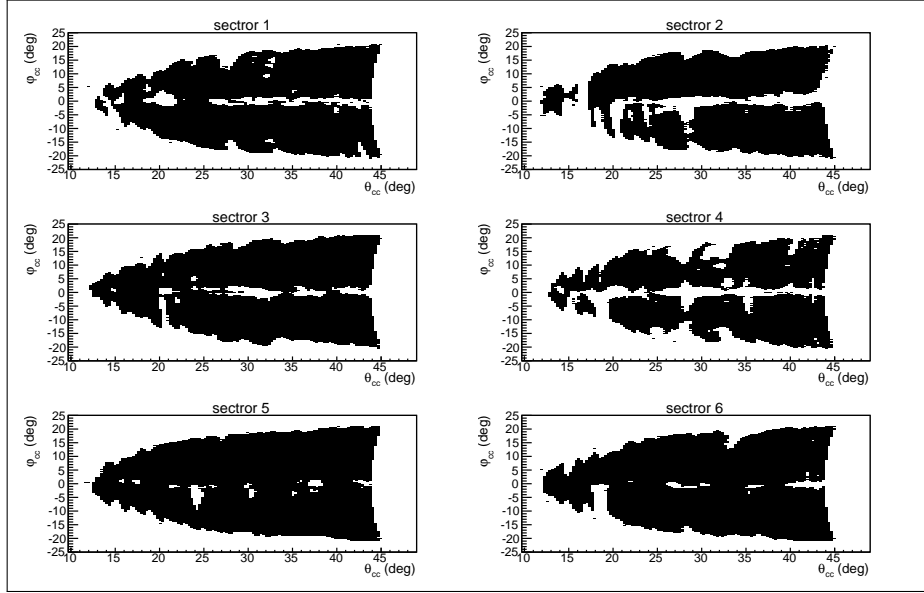


Figure 2.6: Zones where CC is efficient enough to accept good electron candidates are shown in black as function of the polar (θ_{cc}) and azimuthal (φ_{cc}) angles in the CC plane for six CLAS sectors.

271 where *index* is 1 for right PMTs, -1 for left PMTs, and 0 for the case when both PMTs were
272 fired.

273 As it is seen in Fig. 2.7, there are some peaks at low number of photoelectrons. These
274 peaks correspond to π^- contamination and/or noise in PMTs [25]. To eliminate events under
275 this peak all events on the left side of the red vertical line in Fig. 2.7 are excluded from the
276 analysis.

277 Since Monte Carlo does not reproduce photoelectron distributions well enough, the cut
278 shown by the red line in Fig. 2.7 is applied only to the data. To recover good electrons that
279 were cut off in this way a special procedure is developed. The part of the distributions on
280 the right side of the red line is fit by function 2.1.11, which is a slightly modified Poisson
281 distribution.

$$y = P_1 \left(\frac{P_3^{\frac{x}{P_2}}}{\Gamma \left(\frac{x}{P_2} + 1 \right)} \right) e^{-P_3} \quad (2.1.11)$$

282 The fitting function is then continued into the region on the left side of the red line. In
283 this way the two regions, shown by blue and green in Fig. 2.7, are determined. Finally the
284 correction factors are defined by 2.1.12 and applied as a weight for each event which goes to
285 the particular PMT.

$$F_{ph. el.} = \frac{\text{green area} + \text{blue area}}{\text{green area}} \quad (2.1.12)$$

It needs to be mentioned that segments one, two, and 18 are removed from the analysis completely since they are dominated by events with very low number of photoelectrons. The procedure described above is applied for left and right side PMTs. For the events with both PMTs fired the peak at low number of photoelectrons is almost absent and no additional cut like this is needed.

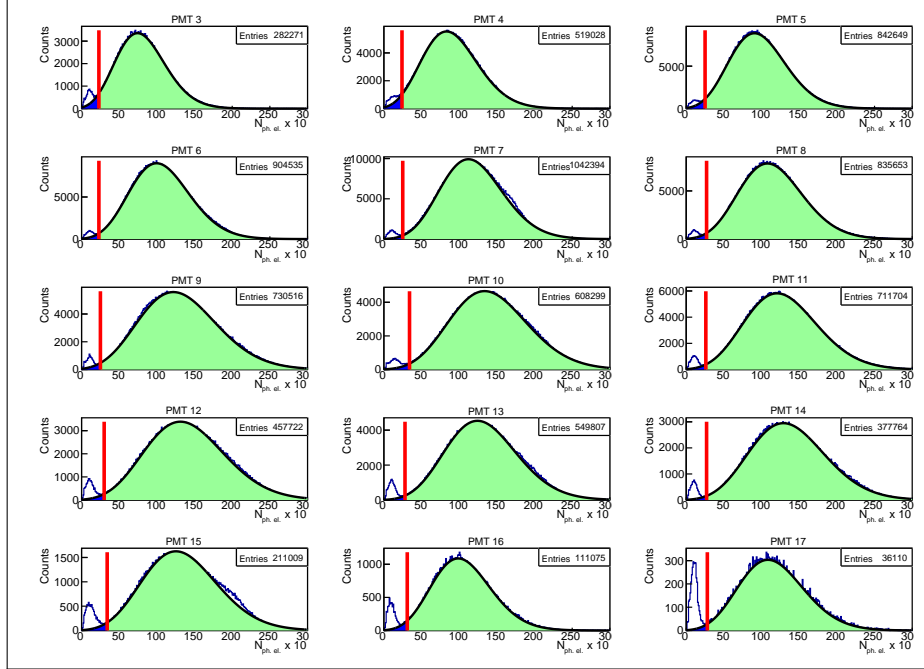


Figure 2.7: Number of photoelectrons multiplied by ten for the left side of sector one of CC. Various plots correspond to various CC segments. Black curves show the fit by function 2.1.11. Red vertical lines show the applied cut. Regions that are needed to calculate the ratio 2.1.12 are shown in blue and green.

2.1.2 Hadron identification

The CLAS time-of-flight (TOF) system provides information on particle velocity ($\beta = v/c$). The information from the Drift Chambers allows to measure the particle momentum (P). Therefore, charged hadron can be identified using the relation between particle mass, momentum, and velocity

$$\beta = \frac{p}{\sqrt{p^2 + m^2}}. \quad (2.1.13)$$

For the hadron identification, only events with electron candidates that have been selected in the previous step are used. β versus momentum distributions are plotted for each TOF

298 scintillator in each CLAS sector (see example plots for CLAS sector one in Fig. 2.8 for
 299 positively charged particles and in Fig. 2.9 for preliminary selected π^- candidates).

300 It needs to be mentioned that in order to simplify the analysis process the preliminary
 301 particle id was made on an initial step of converting data from the BOS files to the files with
 302 ROOT trees. It leads to the fact that in Figure 2.9 only the region that corresponds to the
 303 preliminary selected π^- candidates is filled with events.

304 For visual identification of improperly working scintillation bars, theoretical curves with
 305 hadron 2.1.13 (π^+ , π^- , proton) proper mass assumptions are plotted. As it can be seen in the
 306 plots paddle number 48 has enormous number of events. It happened most likely, because
 307 more paddles of TOF were connected to TDC 48 or due to cooking problems. Therefore,
 308 paddles 48 are excluded from the analysis. Besides scintillators number 17 in sectors two
 309 and five worked improperly and are also excluded from the analysis.

310 Events between purple dashed curves in Fig. 2.8 and Fig. 2.9 are selected as π^+ and π^-
 311 candidates, respectively. Analytical formulae for these curves are given in 2.1.14.

$$\begin{aligned} \beta &< \frac{(205.98 - P_{hadron}) \left(\frac{200 - P_{hadron}}{200 + P_{hadron}} \right)^{0.7} (P_{hadron} + 0.5)}{(200.02 + P_{hadron}) \sqrt{(P_{hadron} + 0.5)^2 + 0.019}} + 0.019 \\ \beta &> \frac{(1 + 5 \times 1.07 \times (P_{hadron} - 0.07))(P_{hadron} - 0.07)}{(1 + 5 \cdot (P_{hadron} - 0.07)) \sqrt{(P_{hadron} - 0.07)^2 + 0.138^2}} - 0.1 \end{aligned} \quad (2.1.14)$$

312 For proton candidates the selection cuts 2.1.15 are used. They are shown by the red
 313 dashed lines in Fig. 2.8.

$$\begin{aligned} \beta &< \left(\frac{P_{hadron}}{\sqrt{P_{hadron}^2 + 0.938^2}} + 0.02 \right) \frac{1.2 + 0.92P_{hadron}}{1 + P_{hadron}} \\ \beta &> \left(\frac{P_{hadron}}{\sqrt{P_{hadron}^2 + 0.938^2}} - 0.05 \right) \frac{1 + P_{hadron}}{0.9 + 1.06P_{hadron}} \end{aligned} \quad (2.1.15)$$

314 As seen in Figs. 2.8 and 2.9 some scintillators with numbers larger equal 40 have two
 315 bands (both of them most likely correspond to the given hadron). The origin of these two
 316 bands can be based on mistakes in data cooking/calibration or the consequence of the fact
 317 that two scintillation bars are connected to one TDC. For this large-number scintillators all
 318 events laying higher than the upper cut for protons are assumed to be pions.

319 2.1.3 Timing correction

320 Another approach can be used to treat the scintillators with numbers larger equal 40, which
 321 have two bands that correspond to the same hadron. The idea of this approach is to plot

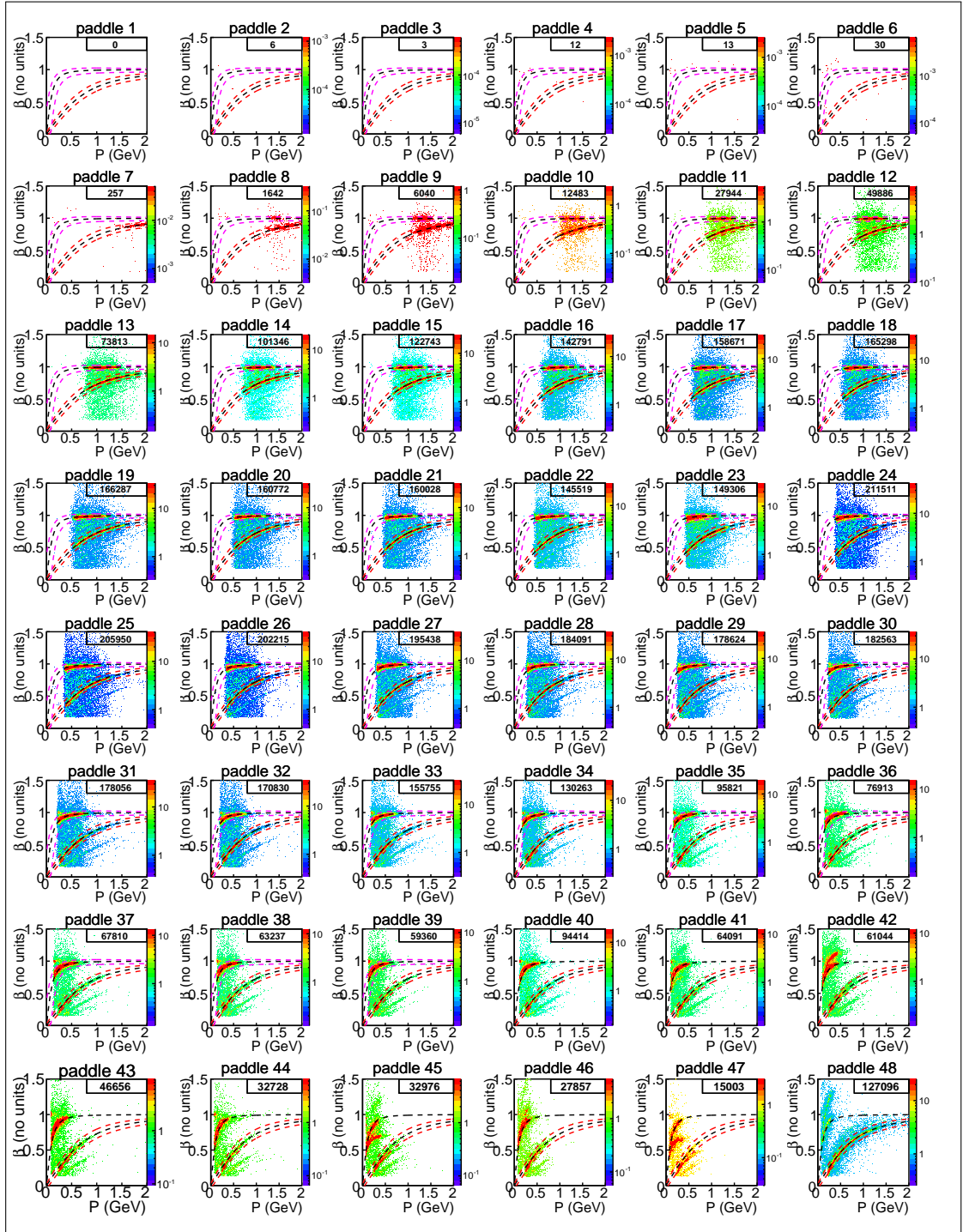


Figure 2.8: β versus momentum distributions for positively charged particles for different TOF scintillators in CLAS sector one. Black dashed curves are theoretical under the exact hadron mass assumption 2.1.13. Events between the two purple dashed 2.1.14 and two red dashed 2.1.15 curves are selected as π^+ and proton candidates, respectively. For scintillators with number greater equal 40 all events laying higher than the upper red dashed curve are assumed as π^+ candidates. Number of events is shown in the right upper corner of each plot.

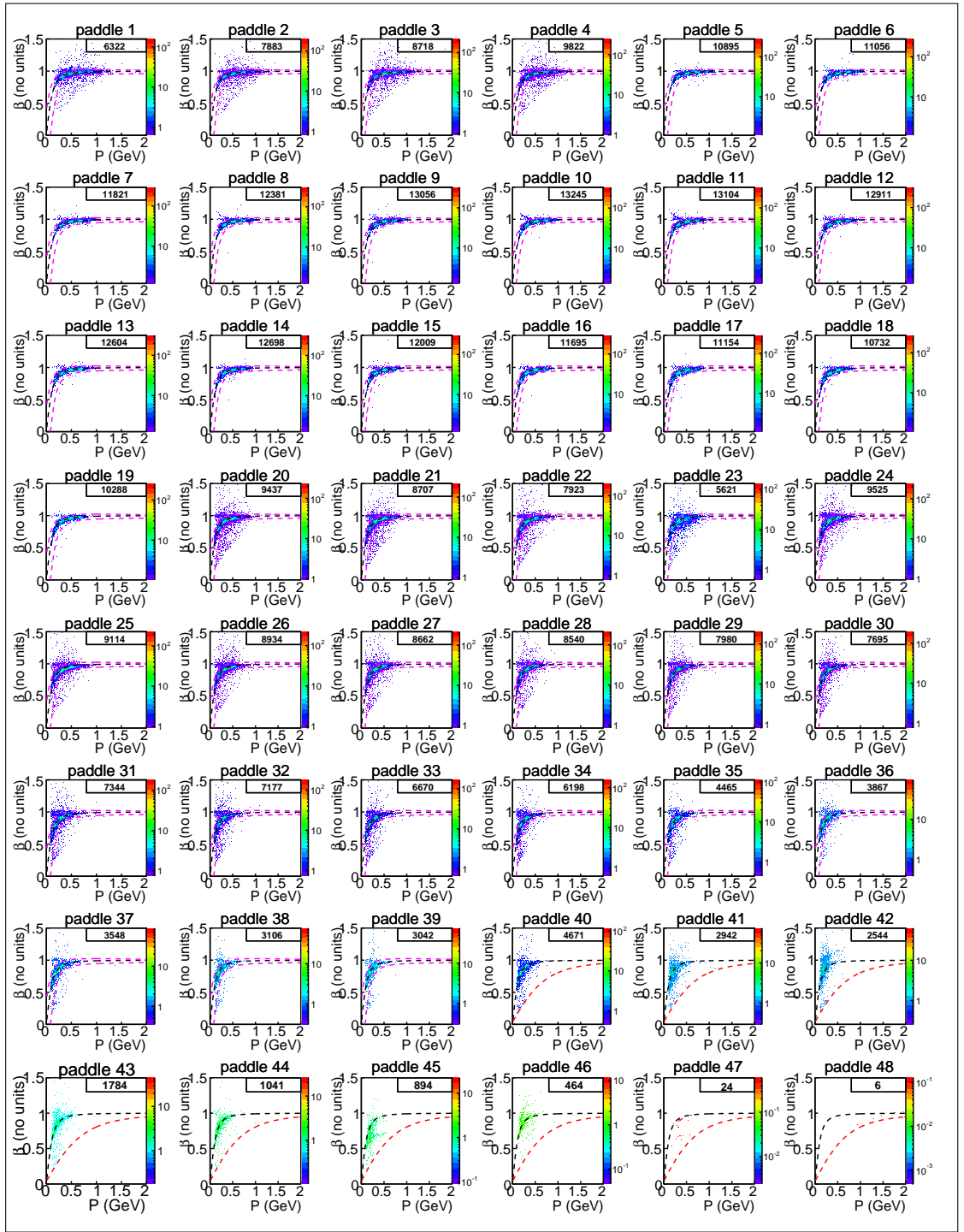


Figure 2.9: β versus momentum distributions for negatively charged particles for different TOF scintillators in CLAS sector one. Black dashed curves are theoretical under the exact π^- mass assumption 2.1.13. Events between the two purple dashed 2.1.14 curves are selected as π^- candidates. For scintillators with number greater equal 40 all events laying higher than the red dashed curve are assumed as π^- candidates. Number of events is shown in the right upper corner of each plot.

322 the difference between the measured time that hadron travels between the target and the
 323 SC plane and the same quantity calculated under the exact hadron mass assumption. This
 324 time difference ΔT is calculated as:

$$\Delta T = \frac{l_h}{c} \left(\frac{1}{\beta_n} - \frac{1}{\beta_{old}} \right), \quad (2.1.16)$$

325 where l_h is the hadron path length from the vertex to the SC plane (the *Path* variable in
 326 DCPB bank), β_n is the nominal β with the exact mass of the hadron assumed (see Eq. 2.1.13),
 327 β_{old} is the value of β that needs to be corrected, c is the speed of light.

328 In the left side in Fig. 2.10 ΔT is plotted for the π^+ candidates for the paddle 42 in
 329 CLAS sector one as a function of their momentum. The two horizontal bands are clearly
 330 seen in this figure. One of them is around $\Delta T = 0$, while another one is shifted by two nano
 331 seconds and corresponds to the wrong band in β versus momentum distribution for paddle
 332 42 (see Fig. 2.8).

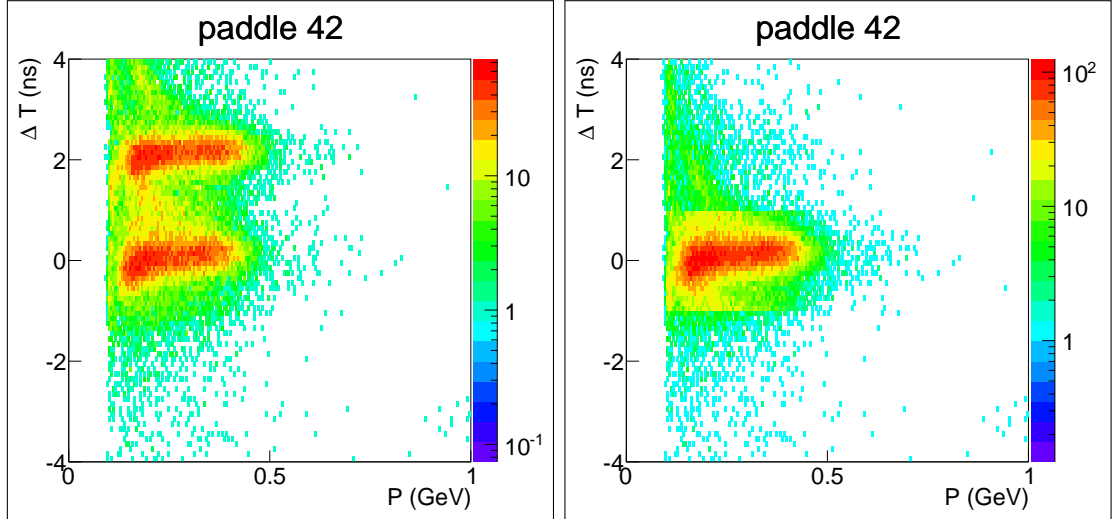


Figure 2.10: Quantity ΔT that is given by Eq. 2.1.16 before (left plot) and after (right plot) the timing corrections.

333 The idea of timing corrections is to shift the wrong bands in ΔT versus momentum
 334 distributions to their correct position around $\Delta T = 0$. The result of this shift is shown in
 335 the right side in Fig. 2.10. After this shift the correct value of β is calculated using Eq. 2.1.17.

$$\beta_{corr} = \frac{1}{\frac{1}{\beta_n} - \frac{(\Delta T - t_{max})c}{l_h}}, \quad (2.1.17)$$

336 where t_{max} is the position of each wrong band, 2 ns in the example shown in Fig. 2.10.

After applying the procedure that is described above for all pion candidates in all problematic paddles with double bands, the β versus momentum distributions are plotted, see Fig. 2.11. As it is seen in Fig. 2.11 there are no paddles with double bands anymore. So, even for scintillators with the numbers greater equal 40 the same β versus momentum cuts (see Eq. 2.1.14) can be applied. This procedure is performed for pion candidates only, since the effect of the band doubling in the β versus momentum distributions for the protons is rather small and all proton candidates are lying inside the cut given by Eq. 2.1.15 even without timing corrections.

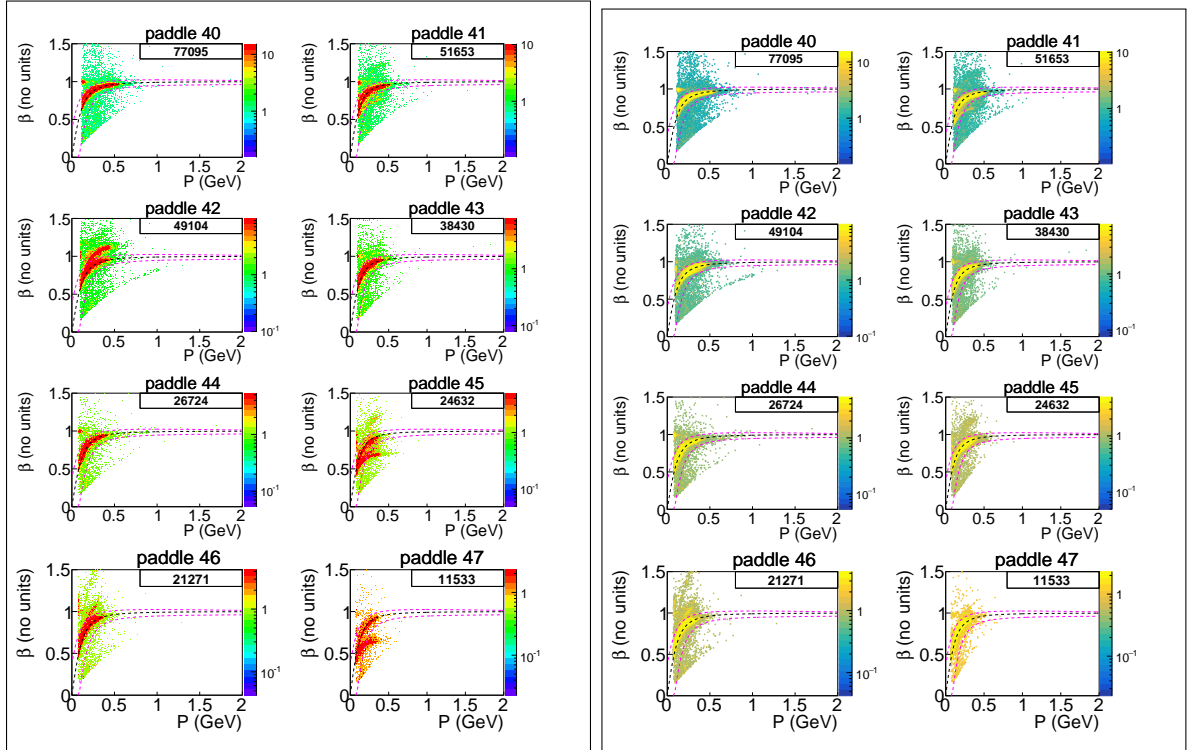


Figure 2.11: β versus momentum distributions before (left plot) and after (right plot) the timing corrections for π^+ . Only scintillators in CLAS sector one with number larger than 40 are shown. Black dashed curves are theoretical under the exact π^+ mass assumption 2.1.13. Events between the two purple dashed 2.1.14 and two red dashed 2.1.15 curves are selected as pions. Number of events is shown in the right upper corner of each plot.

Both methods of hadrons identification that are described in the previous and this sections have been compared and it is found that they give pretty small difference in the cross sections. Nevertheless, the final cross sections presented in this analysis are obtained using the timing corrections described in this section.

349 2.2 Momentum corrections

350 2.2.1 Electron momentum correction

351 Due to the slight misalignments in the DC position, small inaccuracies in the description of
 352 the torus magnetic field, and other possible reasons the momentum and angle of particles
 353 may have some small systematic deviations from the real values. Since the effects are of
 354 unknown origin, they cannot be simulated in GSIM. Hence a special momentum correction
 355 procedure is needed for the data. The approach [27], which is based on elastic kinematic,
 356 was chosen for this purpose.

357 Low beam energy ~ 2 GeV of analyzed dataset leads to the small shift (~ 3 MeV) in
 358 elastic peak position. For comparison for 6 GeV runs this shift is about 20 MeV. From [27]
 359 it is known that momentum corrections are essential only for high-energetic particles. Since
 360 in 2π kinematics hadrons carry only small portion of the system momentum, the expected
 361 momentum corrections for them are significantly less than for electrons and can be neglected.

362 In Fig. 2.12 elastic peak positions are shown for six CLAS sectors before (left panel)
 363 and after (right panel) electron momentum correction. The peaks are fit by Gaussians with
 364 polynomial background, fitting curves are shown in Fig. 2.12, and the fit parameter $p1$
 365 corresponds to the elastic peak position. As seen in Fig. 2.13, elastic peak positions for all
 366 CLAS sectors get closer to the proton mass, shown by red horizontal line. The momentum
 367 resolution for electrons can be roughly estimated from elastic peak width that is about nine
 368 MeV.

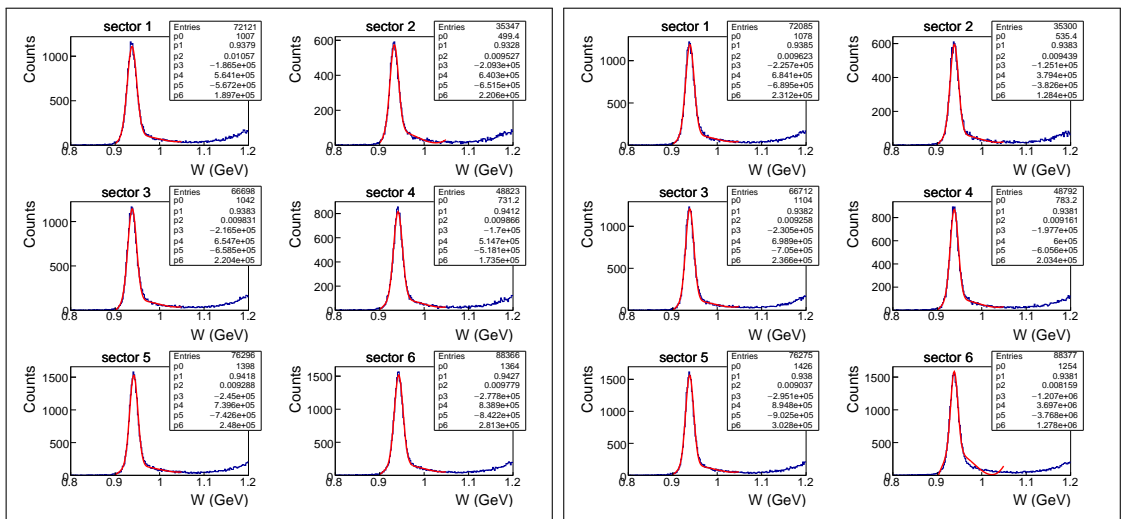


Figure 2.12: Elastic peaks for six CLAS sectors before (left panel) and after (right panel) electron momentum correction. Fit parameter $p1$ corresponds to elastic peak position.

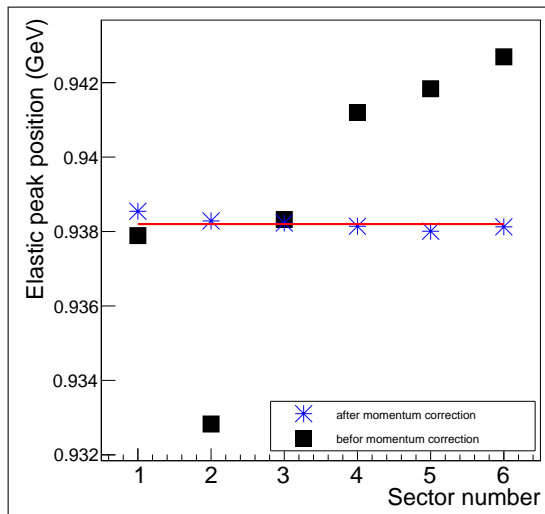


Figure 2.13: Elastic peak position for six CLAS sectors before (black squares) and after (blue stars) electron momentum correction. Horizontal red line shows the proton mass.

369 Due to unknown reasons (most likely because electrons lose energy when they travel
 370 through the detector and target media) the reconstructed electron momentum appears to
 371 be slightly lower than the generated one. Therefore, an adapted electron momentum correc-
 372 tion procedure is also applied to the Monte Carlo events. This correction depends only on
 373 scattered electron angle θ and momentum, but not on the CLAS sector. Figure 2.14 shows
 374 differences between thrown and reconstructed electron momenta before and after the correc-
 375 tion procedure. As shown in Fig. 2.14, these differences become negligible after momentum
 376 corrections have been applied.

377 2.2.2 Proton momentum correction (Energy loss)

378 While traveling through the detector and the target, the proton loses part of its energy due
 379 to interaction with media, hence the measured momentum is lower than the one the proton
 380 actually had right after the interaction. This effect is especially important for the low-
 381 energy protons and can lead to misdetermination of various kinematical quantities. GSIM
 382 simulation of the CLAS detector correctly propagates protons through the media and is used
 383 to account for this effect by using both information about the generated and reconstructed
 384 protons.

385 To obtain the correction function, event distributions for the differences between gener-
 386 ated and reconstructed proton momenta are binned in proton momentum and proton angle θ
 387 and fit by Gaussians. Then in this way obtained peak positions are fit as function of proton
 388 momentum and proton angle θ . The results are shown in Fig. 2.15. The function shown in

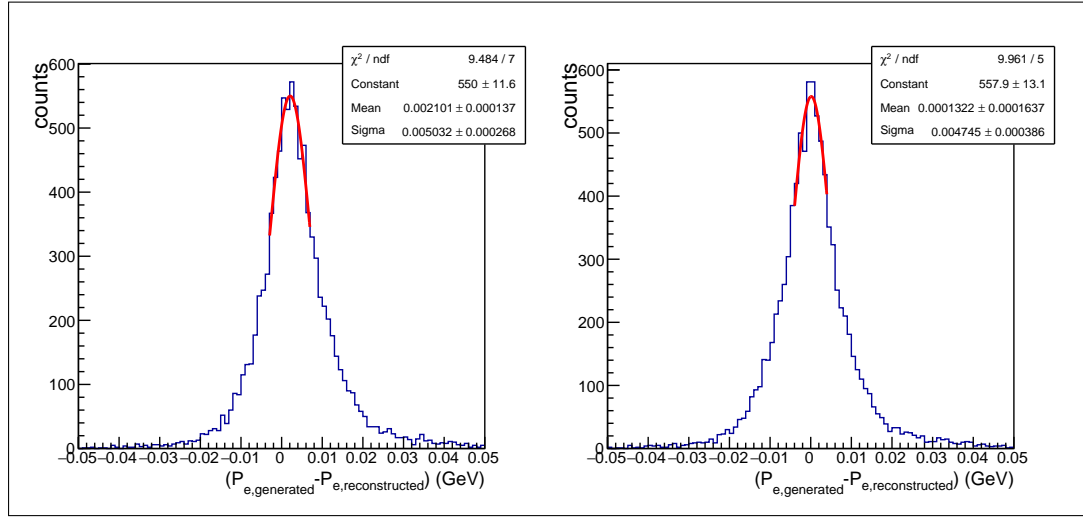


Figure 2.14: The difference between generated and reconstructed electron momenta before (left plot) and after (right plot) the momentum correction has been applied to the reconstructed electrons.

389 Fig. 2.15 gives the percentage of the momentum that protons lose when they move through
 390 the detector and target media. This function is used to correct the momentum both in the
 391 simulation and the data.

392 It needs to be mentioned that to isolate the pure effect of energy loss, reconstructed
 393 events with and without detector and target material need to be compared. Since in the
 394 used procedure differences between generated and reconstructed events are analyzed, the
 395 correction function shown in Fig. 2.15 can also include other effects that lead to improper
 396 proton momentum reconstruction.

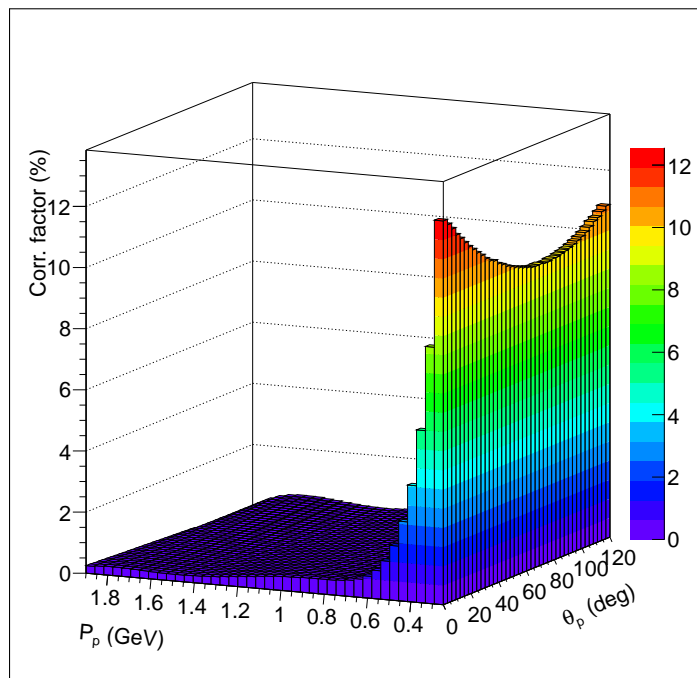


Figure 2.15: The percentage of momentum that protons lose when they move through the detector and target media as a function of the momentum and scattered angle θ of the proton.

³⁹⁷ Chapter 3

³⁹⁸ Other cuts and corrections

³⁹⁹ 3.1 Fiducial cuts

⁴⁰⁰ The CLAS detector has an active detection solid angle that is obviously smaller than 4π .
⁴⁰¹ This is in part due to the space filled with the torus field coils: the angles covered by the coils
⁴⁰² are not equipped with any detection system and therefore form a "dead" area for detection.
⁴⁰³ Moreover, different studies and analyses have shown that also the edges of the active area
⁴⁰⁴ do not provide a safe region for particle reconstruction, being affected by rescattering from
⁴⁰⁵ the coil, field distortions, and similar effects. Therefore it is now common practice to accept
⁴⁰⁶ for the analysis only events inside specific fiducial cuts, i.e. cuts on the kinematic variables
⁴⁰⁷ (momentum and angles) of each particle. This method guarantees that the reconstructed
⁴⁰⁸ events accepted in the analysis include only particles detected in "safe" areas of the detector,
⁴⁰⁹ that is where the acceptance is thought to be well understood. These cuts are applied for
⁴¹⁰ both real events and Monte Carlo reconstructed events and produce a reduction factor in
⁴¹¹ the number of events accepted in each kinematic bin that is called detector acceptance.

⁴¹² 3.1.1 Fiducial cuts for negatively charged particles

⁴¹³ In the CLAS experiments with the normal direction of the torus magnetic field, like in e1e
⁴¹⁴ experiment, negatively charged particles are inbending. For that type of particles sector
⁴¹⁵ independent, symmetrical, and momentum dependent cuts are applied. To establish the
⁴¹⁶ shape of these cuts relatively flat areas in φ distributions are selected. For that purpose all
⁴¹⁷ events are binned in the particle momentum and the particle polar angle θ (see Fig. 3.1).
⁴¹⁸ In Fig. 3.1 φ distributions are shown for one slice over momentum and for various bins in
⁴¹⁹ θ for electrons (left side plots) and π^- (right side plots). Events between the vertical lines
⁴²⁰ in Fig. 3.1 are selected for further analysis. The analytical shape of these cuts is given by

⁴²¹ Eq. 3.1.1 for electrons and Eq. 3.1.2 for π^-

$$\begin{aligned}
 \theta_{min} &= 9.7 + 17/(P_{e'} + 0.2) \\
 \delta\varphi_{e'} &= p_1 \sin(p_2(\theta_{e'} - \theta_{min}))^{p_3 + p_4/\theta_{e'} + p_5/\theta_{e'}^2} + p_6 \\
 p_1 &= 37.3(0.85 + 1.1P_{e'}) \\
 p_2 &= 0.01745 \\
 p_3 &= p_1/37.3 \\
 p_4 &= -62.8 - 30P_{e'} \\
 p_5 &= 1525 \\
 p_6 &= 0
 \end{aligned} \tag{3.1.1}$$

$$\begin{aligned}
 \theta_{min} &= 11 + 8/(0.472P_{\pi^-} + 0.117) \\
 \delta\varphi_{\pi^-} &= p_1 \sin(p_2(\theta_{\pi^-} - \theta_{min}))^{p_3 + p_4/\theta_{\pi^-} + p_5/\theta_{\pi^-}^2} + p_6 \\
 p_1 &= 30.5 \\
 p_2 &= 0.01745 \\
 p_3 &= 0.705 + 1.1P_{\pi^-} \\
 p_4 &= -63.2 - 33.3P_{\pi^-} \\
 p_5 &= 1530 \\
 p_6 &= -1
 \end{aligned} \tag{3.1.2}$$

⁴²² where $P_{e'}$ and P_{π^-} are the momenta of the particles in GeV, $\theta_{e'}$ and θ_{π^-} are the polar angles
⁴²³ of the particles in degrees. $\delta\varphi_{e'}$ and $\delta\varphi_{\pi^-}$ are the portions of the polar angle φ accepted by
⁴²⁴ the fiducial cut, or in other words if $\theta > \theta_{min}$ and $|\varphi| < \delta\varphi$ then the particle is accepted.
⁴²⁵ The functions 3.1.1,3.1.2 are shown in 2D plots φ versus θ in Fig. 3.2 for electrons (left side)
⁴²⁶ and π^- (right side).

⁴²⁷ There are some additional inefficient areas that are not related to the gaps between
⁴²⁸ CLAS sectors. These areas are typically caused by drift chamber and time-of-flight system
⁴²⁹ inefficiencies (dead wires or PMTs). Some of them are reproduced in Monte Carlo simulation,
⁴³⁰ while others are not. To exclude the latter from the analysis additional fiducial cuts on θ
⁴³¹ versus momentum distributions are applied. These cuts are individual for each CLAS sector.
⁴³² They are shown by the black curves for real and Monte Carlo events in Fig. 3.3 for electrons
⁴³³ and in Fig. 3.4 for π^- . For the electron distributions in Fig. 3.3 only CLAS sector five is
⁴³⁴ shown since there are no dead areas in other sectors.

⁴³⁵ 3.1.2 Fiducial cuts for positively charged particles

⁴³⁶ For positively charged particles, which are outbending in the e1e experiment, momentum
⁴³⁷ independent and asymmetrical fiducial cuts are the best choice. These cuts are established

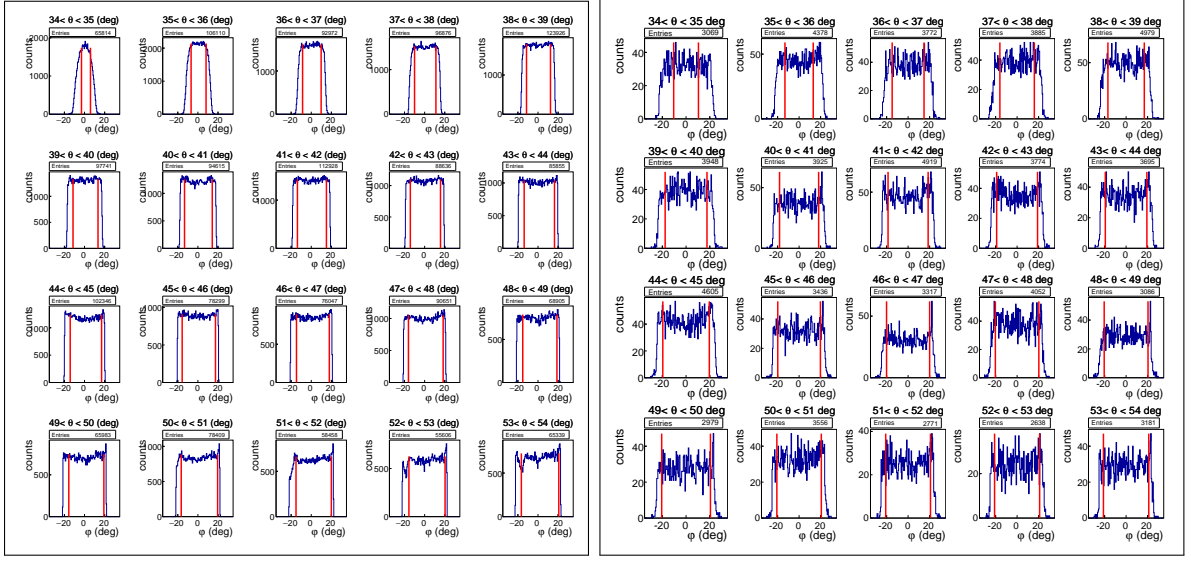


Figure 3.1: φ -event distributions for electrons (left plot) and π^- (right plot). Electrons are shown for CLAS sector 6 and a momentum range from 480 MeV to 560 MeV, while π^- are for sector 3 and a momentum range from 400 MeV to 600 MeV. Various plots represent bins in polar angle θ . Events between the red lines are selected for the analysis.

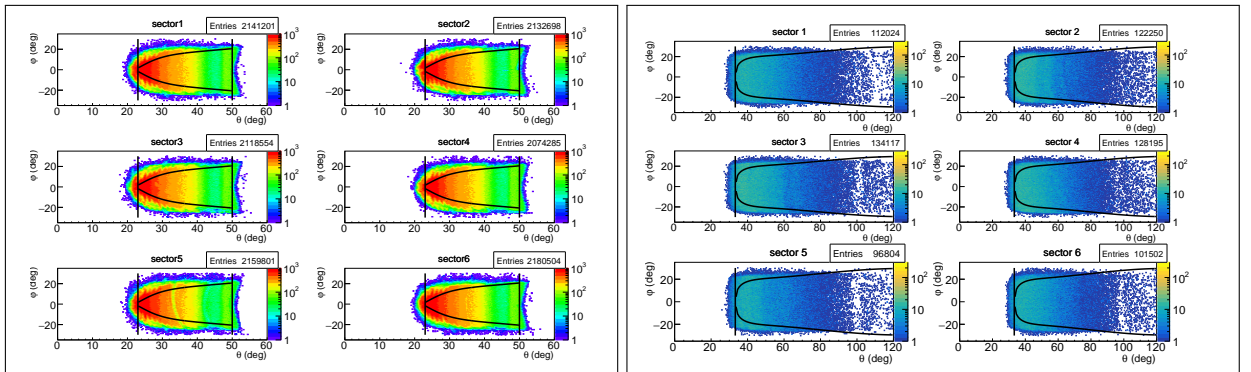


Figure 3.2: φ versus θ distributions for electrons with momenta from 1120 MeV to 1200 MeV (left frame) and π^- with momenta from 400 MeV to 600 MeV (right frame) for all six CLAS sectors. Curves show the applied fiducial cuts, vertical lines stand for minimum and maximum θ cuts.

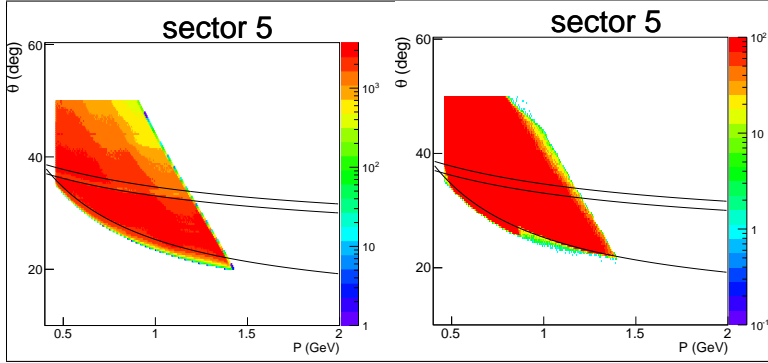


Figure 3.3: θ versus momentum distributions for electrons in CLAS sector five. Left plot shows real and right plot Monte Carlo events. Black curves show cuts applied to remove inefficient areas.

in the same way as for negatively charged particles, i.e. by selection of the flat parts of the event distributions over φ . The shape of these cuts is given by

$$\begin{aligned}\varphi_{upper} &= 24(1 - e^{-0.08(\theta-9)}) \\ \varphi_{lower} &= -25(1 - e^{-0.1(\theta-10)}),\end{aligned}\quad (3.1.3)$$

where θ is the particle angle in degrees. φ_{upper} and φ_{lower} are the upper and lower cut boundaries. Events with $\varphi_{lower} < \varphi < \varphi_{upper}$ are selected for further analysis.

This function is superimposed on the 2D φ versus θ distributions of real events and shown in Fig. 3.5 by the black curves. Additional cuts in θ versus momentum coordinates are shown by the black curves for Monte Carlo and real events in Fig. 3.6 for protons and in Fig. 3.7 for π^+ .

3.2 Data quality check

During the quite long experimental run the variations of the experimental conditions, like the target density deviation or improper operation of some parts of the detector, can lead to different yields of events. Only parts of the run with relatively stable event rates are selected for the analysis. For that purpose cuts on DAQ live time and number of events per Faraday cup (FC) charge are used.

FC charge updates with given frequency, so the whole run time can be divided into so-called *blocks*. Each *block* corresponds to the portion of time between two FC charge readouts. FC charge readout happens approximately once in ten seconds. The *block* number ranges from one to the maximum number over the run time. The first and last *blocks* in each run

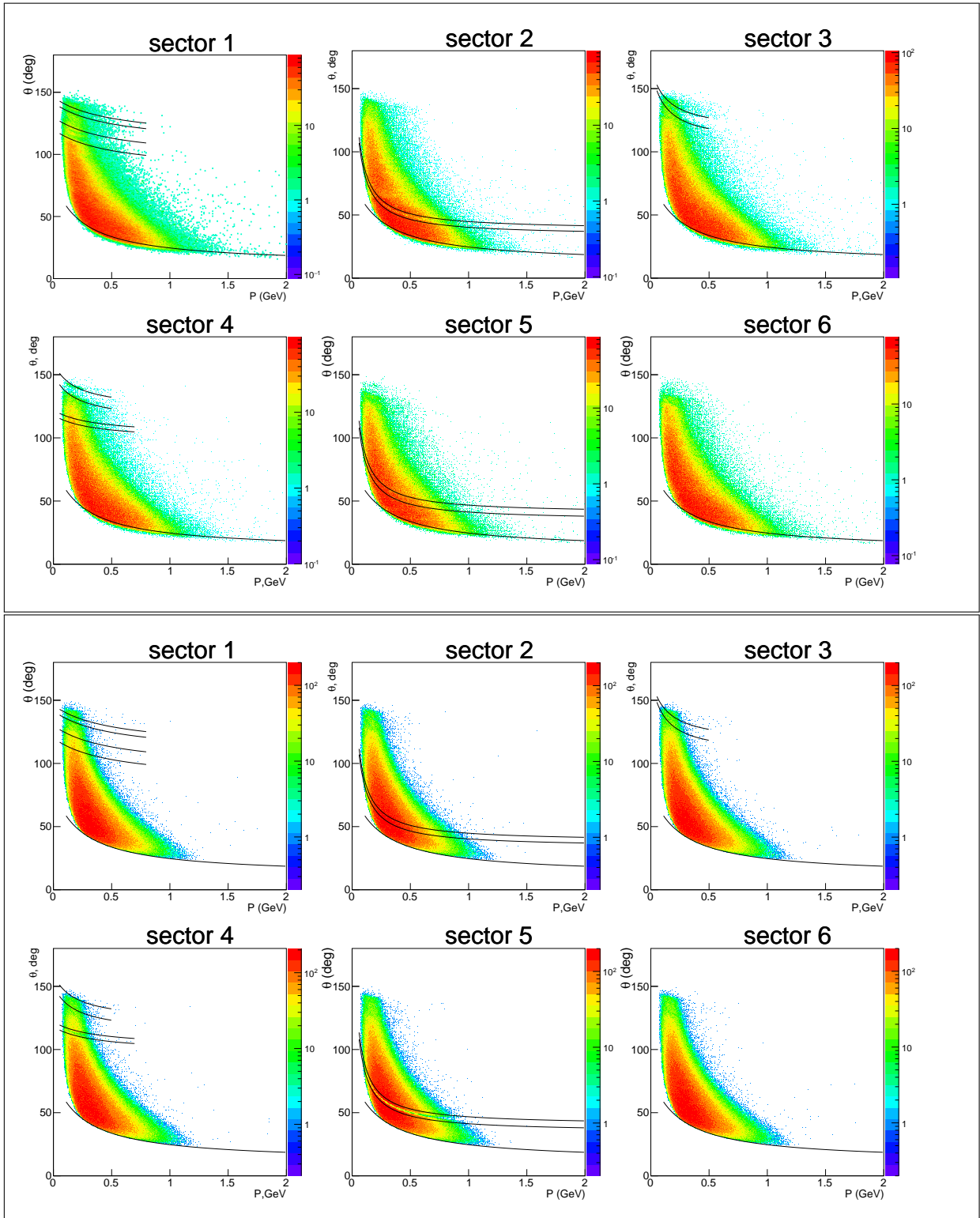


Figure 3.4: θ versus momentum distributions for real π^- events (upper frame) and for Monte Carlo events (lower frame) for all six CLAS sectors. Black curves show cuts applied to remove inefficient areas.

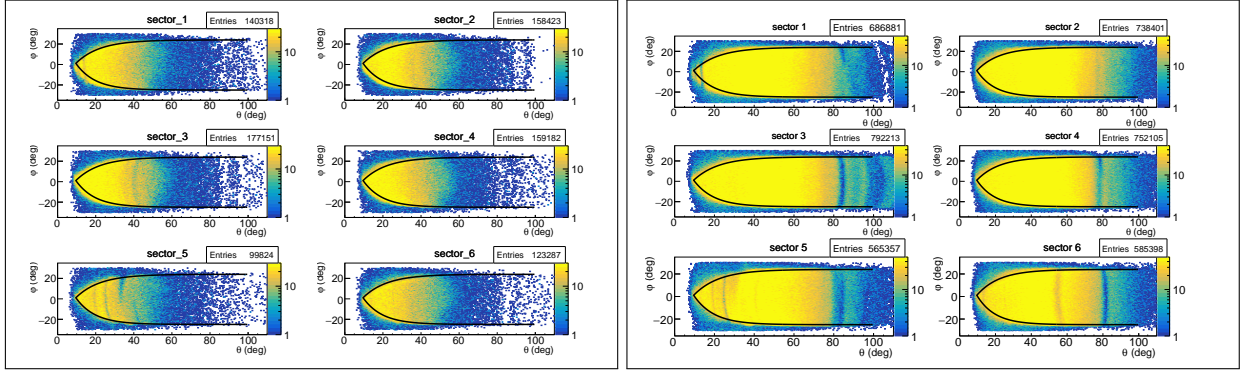


Figure 3.5: φ versus θ distributions for protons with momenta from 600 MeV to 800 MeV (left frame) and π^+ with momenta from 400 MeV to 600 MeV (right frame) for all six CLAS sectors. Curves show the applied fiducial cuts.

456 file are excluded from the analysis since FC readout is not synchronized with begin/end of
457 the file.

458 DAQ live time is the portion of time within the *block* during which the DAQ is able to
459 accumulate events. A significant deviation of the live time from the average value indicates
460 event rate alteration. For instance, if the live time is close to one, then the event rate
461 is too low and vice versa. In Fig. 3.8 DAQ live time and yields of elastic and inclusive
462 events normalized to FC charge are shown as function of *block* number. *Blocks* between the
463 horizontal red lines in Fig. 3.8 are selected for the analysis. Due to the enormous amount of
464 *blocks* all of them can not be made visible in two dimensional histogram, so y-axis projections
465 of histograms in Fig. 3.8 are produced (see Fig. 3.9). The horizontal red cut lines in Fig. 3.8
466 correspond to the vertical red cut lines in Fig. 3.9.

467 3.3 Vertex cut

468 The target is specific to the e1e experiment and its setup is presented in Fig. 3.10. It has a
469 conical shape with diameter varying from 0.4 to 0.6 cm. In some instances cooling system
470 could not extract all the heat generated by the beam and the hydrogen in the target cell
471 could boil. If bubbles stay along the beamline, the real luminosity would be different from
472 the expected value and the absolute measurement will lack accuracy. The conical shape helps
473 to direct bubbles upwards and into a wider area of the target, thus clearing the beamline.
474 The forward aluminum window is made exactly the same as the entry/exit windows of the
475 target cell and can serve for both the estimation of the number of events originated in the
476 target windows and to precisely measure target z position in the beamline.

477 In Fig. 3.11 distributions of electron coordinate z at the interaction vertex are shown for

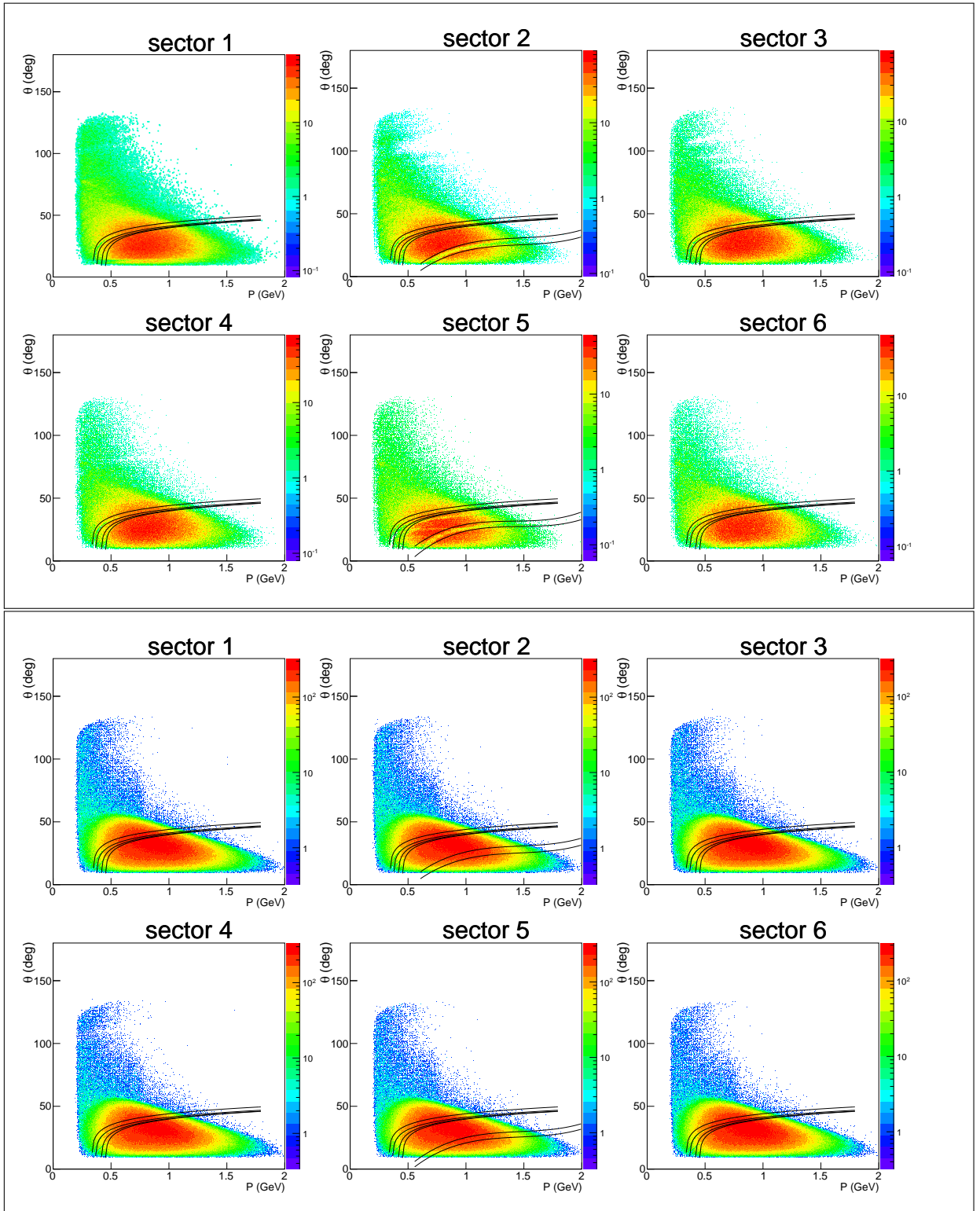


Figure 3.6: θ versus momentum distributions for real proton events (upper frame) and for Monte Carlo events (lower frame) for all six CLAS sectors. Black curves show cuts applied to remove inefficient areas.

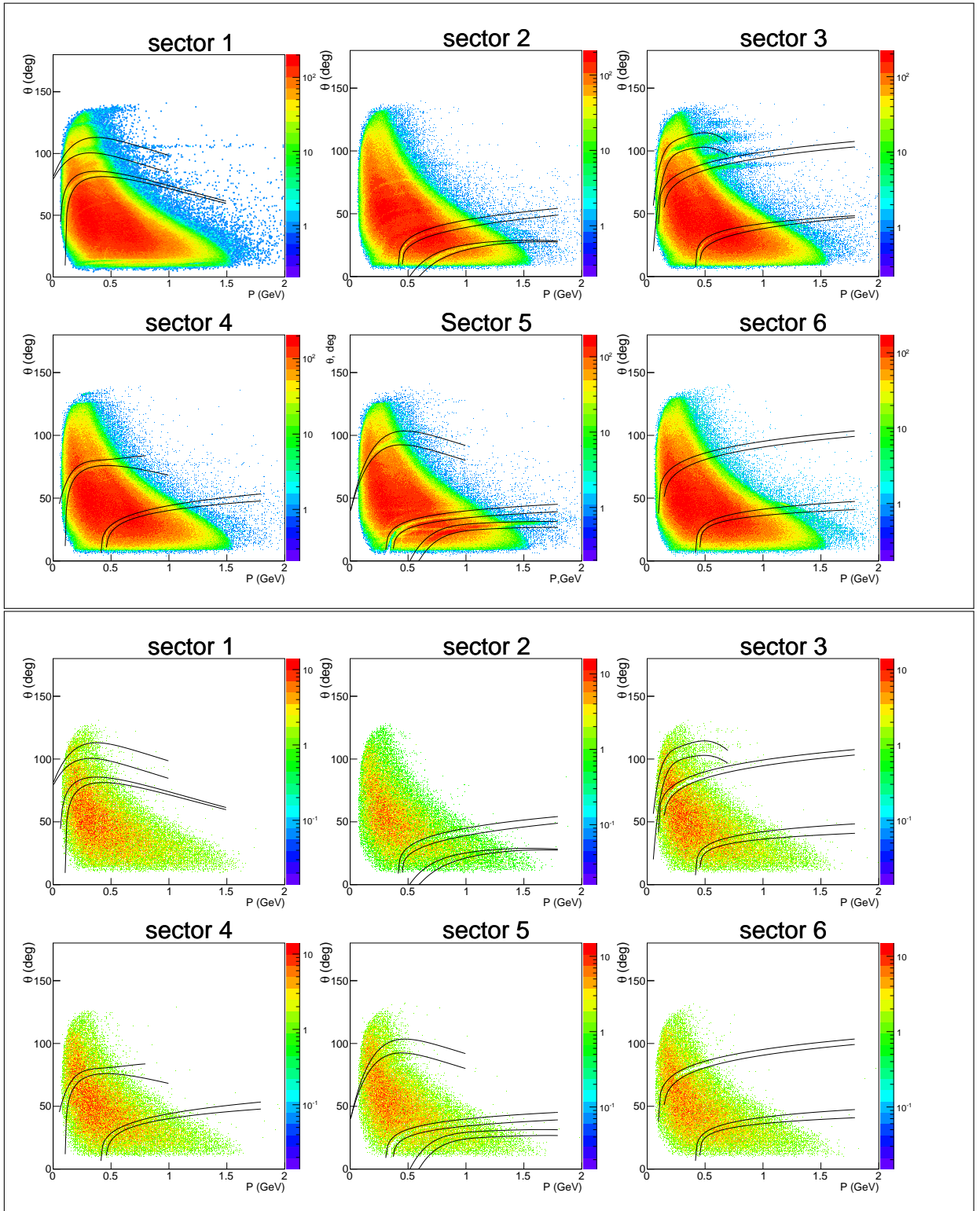


Figure 3.7: θ versus momentum distributions for real π^+ events (upper frame) and for Monte Carlo events (lower frame) for all six CLAS sectors. Black curves show cuts applied to remove inefficient areas.

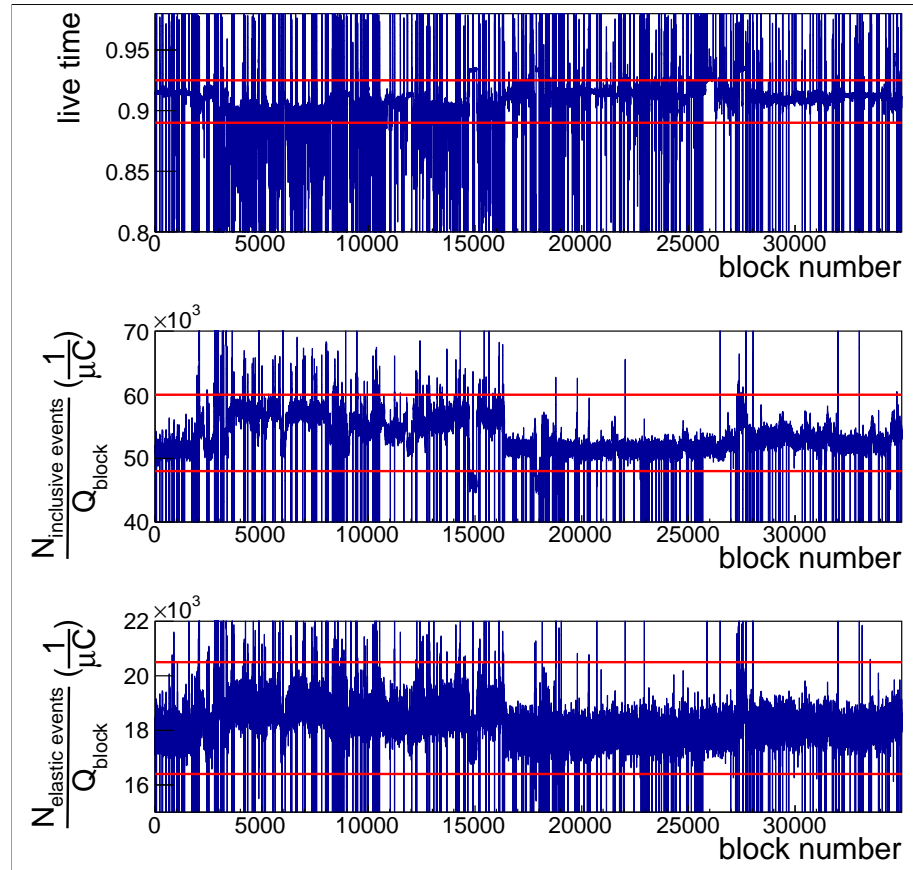


Figure 3.8: In the top plot DAQ live time is shown as function of *block* number. Each *block* corresponds to the portion of events that is accumulated during a single Faraday cup charge reading cycle. *Block* numbers range from one to the maximum number and represents the run duration in Faraday cup reading units. In the middle plot the number of inclusive events accumulated within each *block* divided by FC charge accumulated during the *block* is plotted versus *block* number. Bottom plot shows the number of elastic events accumulated within each *block* divided by FC charge accumulated during the *block* as function of *block* number. Horizontal red lines show the applied cuts.

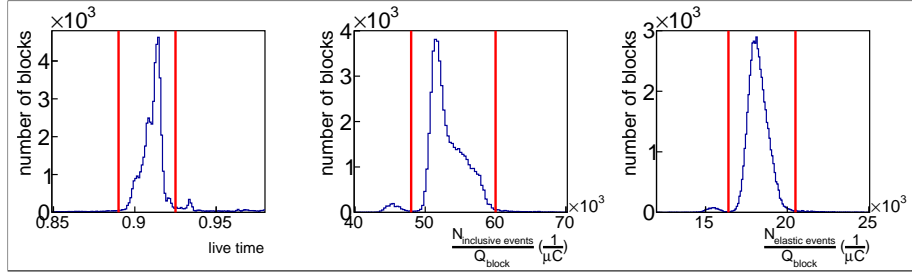


Figure 3.9: Number of *block* occurrences (see explanation in the text) as function of DAQ live time (left plot), inclusive event yield normalized to FC charge (middle plot), and elastic event yield normalized to FC charge (right plot).

events from both empty and full target runs for six CLAS sectors. The vertex coordinate z is taken from DCPB bank, where already beam-offset corrected values are stored. However small vertex corrections are made to shift the peak that corresponds to the forward aluminum window to the same position for full and empty target runs. Vertical green lines in Fig. 3.11 show the cut that is applied in addition to the empty target event subtraction.

In Fig. 3.12 event distributions after subtraction of empty target contribution are shown in comparison with Monte Carlo events both reconstructed and generated. As it can be seen in Fig. 3.12 the simulation reproduces data well enough.

To reduce the number of events in which the electron comes from one and any hadron from another event, additional cuts on the difference of z coordinates of particles at the vertex are applied. These cuts do not allow the registered particles to have z vertices farther apart than 4 cm.

3.4 Exclusivity cut

Due to the experimental conditions the statistics of the double-pion events with all final hadrons registered is rather limited. Moreover, registration of all final hadrons leads to a limited acceptance, so the missing mass technique, when one of the final hadrons is not registered, is the best choice for the double-pion cross section extraction.

For the analyzed reaction one can distinguish four topologies:

- $ep \rightarrow e' p' \pi^+ X$
- $ep \rightarrow e' p' \pi^- X$
- $ep \rightarrow e' \pi^+ \pi^- X$
- $ep \rightarrow e' p \pi^+ \pi^- X$

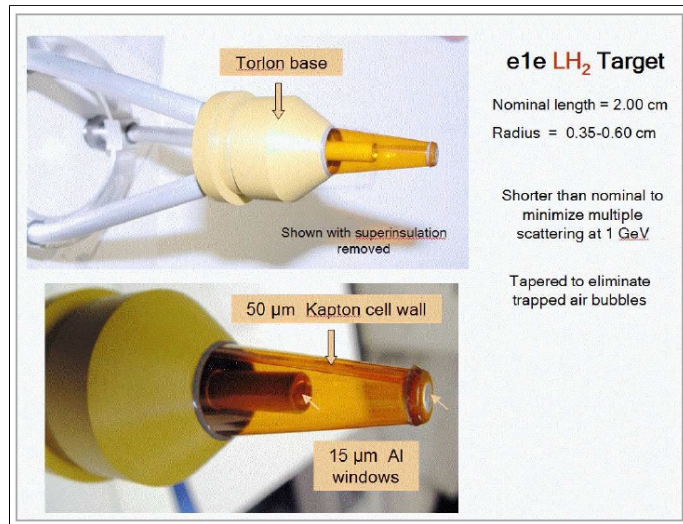


Figure 3.10: The target cell and support structure used during e1e run period.

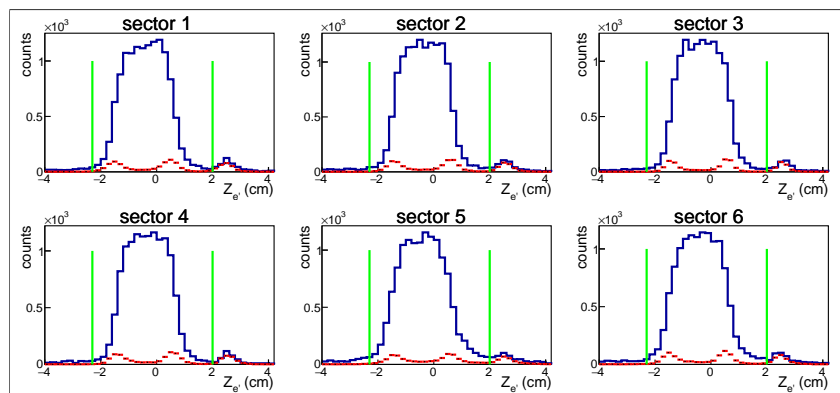


Figure 3.11: Distributions of the electron z coordinate at the vertex for full (blue curves) and empty (red curves) target runs for six CLAS sectors. Vertical green lines show the applied cuts. Both full and empty target distributions are normalized to the corresponding FC charge.

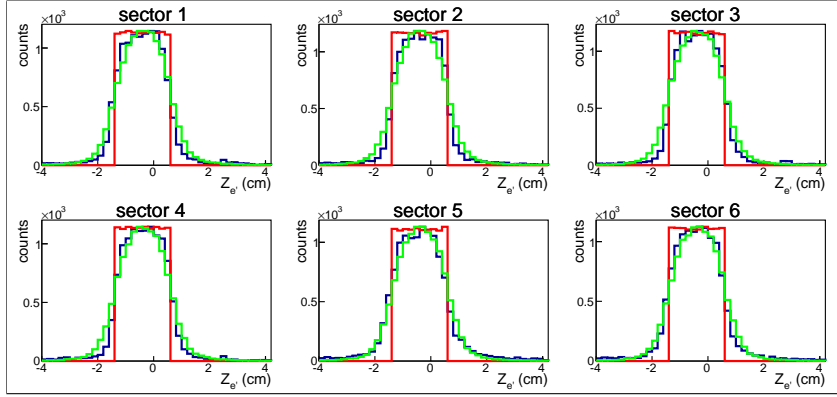


Figure 3.12: Distributions of the electron z coordinate at the vertex for data (blue curves) and Monte Carlo (green curves - reconstructed, red - generated) events for six CLAS sectors. For data empty target contributions are subtracted. All distributions are normalized to the maximum.

These topologies are defined in a way they do not overlap. For example the topology $ep \rightarrow e'p'\pi^+X$ requires the presence of e' , p' and π^+ candidates and absence of π^- candidates, avoiding in this way double counting.

For the case when one of the final hadrons is not registered, the missing mass M_X for the reaction $ep \rightarrow e'h_1h_2X$ is determined by

$$M_X^2 = (P_e + P_p - P_{e'} - P_{h_1} - P_{h_2})^2, \quad (3.4.1)$$

where P_{h_1} and P_{h_2} are the four-momenta of the registered final hadrons, P_e and P_p - four-momenta of initial electron and proton, and $P_{e'}$ - four-momentum of the scattered electron.

While for the events with all final hadrons registered, the missing mass M_X for the reaction $ep \rightarrow e'p'\pi^+\pi^-X$ is given by

$$M_X^2 = (P_e + P_p - P_{e'} - P_{\pi^+} - P_{\pi^-} - P_{p'})^2, \quad (3.4.2)$$

where P_e , P_p , $P_{e'}$, P_{π^+} , P_{π^-} , and $P_{p'}$ are the four-momenta of the initial and final particles.

Distributions of the missing mass squared for various topologies are shown in Fig. 3.13 for different W bins in comparison with Monte Carlo. The top row in Fig. 3.13 stands for the π^- -missing topology, the second row - for π^+ -missing topology, the third row - for proton-missing topology, and the bottom row for the case when all final hadrons are registered. The green arrows show the applied cuts. The π^- -missing topology contributes the biggest part to the statistics (about 70%), while events from other topologies populate kinematical areas with no acceptance for the π^- -missing topology. By combining events from various topologies one can reduce contributions from kinematical cells with zero acceptance (so-called empty cells) (see Sect. 4.5).

519 The simulation is carried out with the JM05 version of double-pion production model
 520 [28–30] and includes inclusive radiative effects according to [31]. More details about Monte
 521 Carlo simulation are in Sect. 4.4.

522 The contribution from the other exclusive channels (exclusive background) to the events
 523 within the exclusivity cuts is also taken into account by the Monte Carlo simulation. Most
 524 of the exclusive background events come from the $ep \rightarrow e'p'\pi^+\pi^-\pi^0$ channel. Both double-
 525 pion and three-pion channels are generated together with the relative weight of their cross
 526 sections taken from [32]. A phase space distribution is assumed for the 3π events. The 3π
 527 background can be barely seen as a separate peak on the right side of the missing mass
 528 squared distributions for the exclusive topology in last two W bins (see Fig. 3.13 bottom row). For the other topologies the 3π background can not be seen as a separate peak and
 529 it manifests itself as a contribution to the tail on the right side of the missing mass squared
 530 distributions.
 531

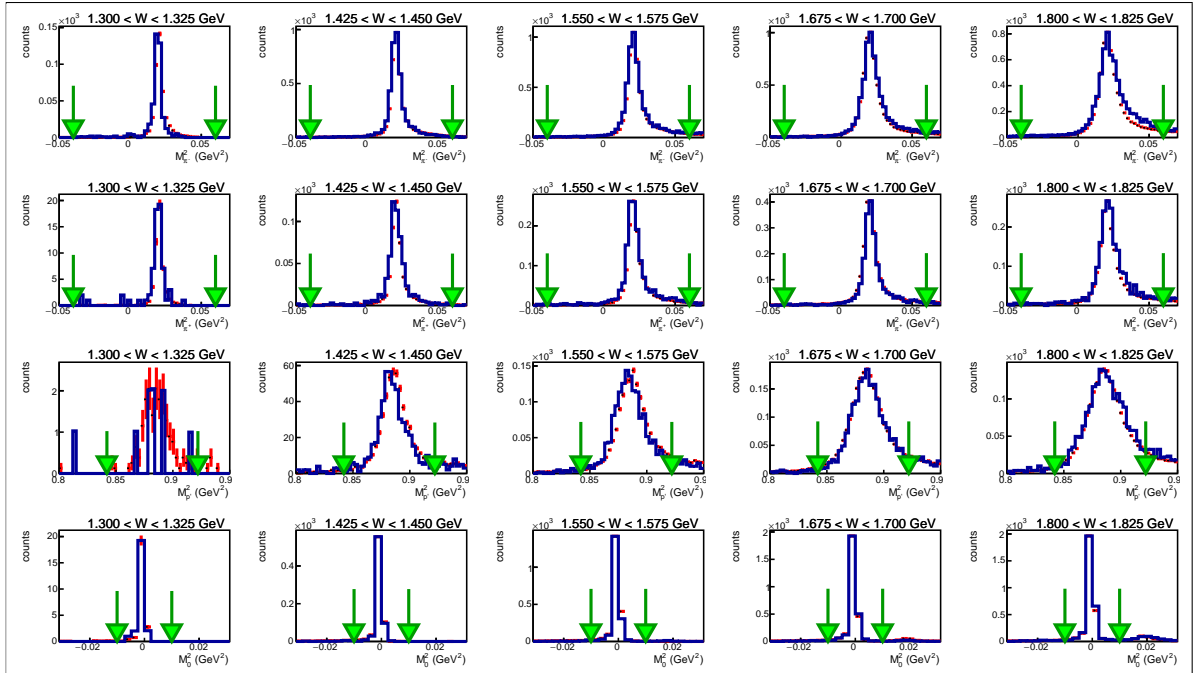


Figure 3.13: Missing mass squared distributions for various bins in W for Q^2 from 0.45 GeV^2 to 0.5 GeV^2 . Blue curves show real and red curves Monte Carlo events. The top row corresponds to π^- -missing topology, the second to π^+ -missing topology, the third to proton-missing topology, and the bottom to the fully exclusive topology. Green arrows show the applied exclusivity cuts.

532 3.5 Missing energy cut

533 To clean up event samples from misidentified and out-of-time particles, a cut on the missing
 534 energy is used in addition to the missing mass cut (Sect. 3.4). It limits the missing energy to
 535 be greater than $m_{miss.hadron} - 50$ MeV, where $m_{miss.hadron}$ is equal to the mass of the missing
 536 hadron (π^- , π^+ , or proton depending on the topology) or zero for the topology where all
 537 final hadrons are registered. The position of this cut is shown by the green vertical lines in
 Fig. 3.14.

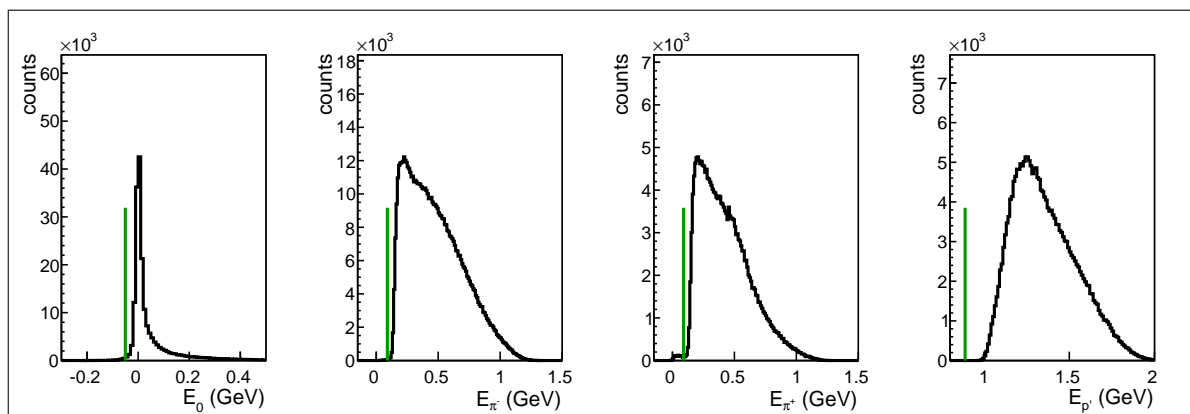


Figure 3.14: Missing energy distributions for various topologies. Left plot corresponds to the topology where all final hadrons are registered and other plots correspond to the topologies with missing π^- , π^+ , or proton, respectively. Green vertical lines show the applied cut. All events on the right side of the lines are selected as good for analysis.

538

539 3.6 Binning and kinematical coverage

540 After all described above cuts and corrections about 2.5 million double-pion events survive
 541 and are used for the cross section calculation. Figure 3.15 shows the available kinematical
 542 coverage in electron variables. double-pion cross sections are calculated in 2D cells within
 543 the white boundaries in Fig. 3.15.

544 The binning in the final hadron variables is chosen according to the statistics left after
 545 the event selection (see Tab. 3.1) and takes into account the fact that the cross section is
 546 small in the W area near the double-pion production threshold. A more detailed description
 547 of the final hadron variable choice is given in Sect. 4.1.

548 It also needs to be mentioned that the right boundary of the invariant mass distributions

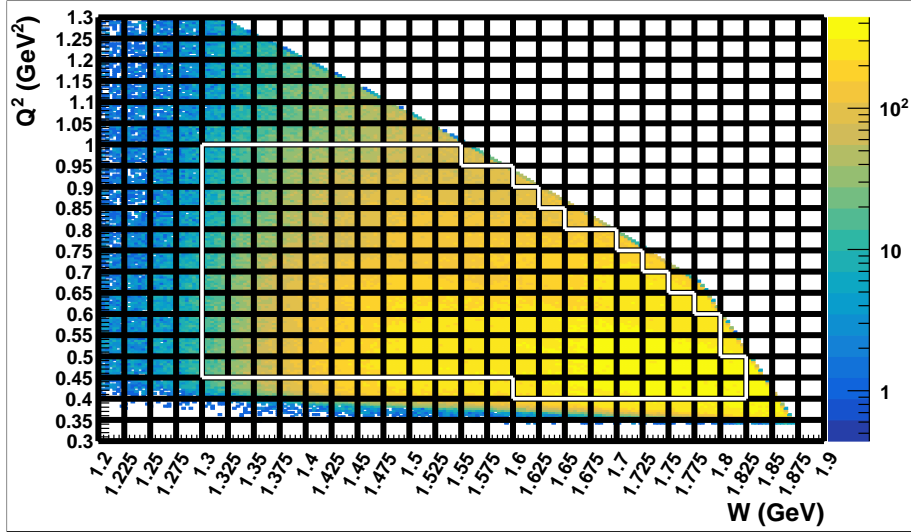


Figure 3.15: Q^2 versus W distribution populated with selected double-pion events. The cross section is calculated in 2D cells within the white boundaries.

549 depends on the value of W , while the left does not (see Eq. 3.6.1).

$$\begin{aligned} M_{left} &= m_{h_1} + m_{h_2} \\ M_{right} &= W - m_{h_3}, \end{aligned} \quad (3.6.1)$$

550 where M_{left} and M_{right} are the left and right boundaries of the invariant mass distribution.
 551 m_{h_1} , m_{h_2} , and m_{h_3} are the masses of final hadrons. The value of W is taken in the center of
 552 the corresponding W bin.

553 It leads to the fact that invariant mass distributions are broader at high W and hence a
 554 more detailed binning in that area is necessary (see Tab. 3.1).

555 Since M_{right} is calculated using the value of W in the center of the corresponding W
 556 bin some events are located beyond the boundaries determined by Eq. 3.6.1. Therefore the
 557 binning in invariant mass needs special attention. Firstly the bin width is determined as:

$$width = \frac{M_{right} - M_{left}}{N_{bins} - 1}, \quad (3.6.2)$$

558 where N_{bins} is the number of bins.

559 Then the invariant mass distributions are obtained with the number of bins N_{bins} and
 560 the left boundary of the first bin is set to M_{left} . That makes the last bin to be situated
 561 completely out of the boundaries given by Eq. 3.6.1. Although the cross section obtained
 562 in this bin is very small, it is kept in analysis since its content contributes to all other cross
 563 sections obtained by integration over the corresponding invariant mass. After the binning

564 corrections this effect is assumed to be taken into account and this last bin in invariant
 565 masses is neglected.

566 It needs to be mentioned that the next to last bin in each invariant mass also needs
 567 special attention. Since the cross sections are obtained in W bin, the right boundaries
 568 of the invariant mass distributions vary for different events within this bin. In Fig. 3.16
 569 the distribution of the invariant mass of the two final hadrons X_1 and X_2 is schematically
 570 illustrated for the bin in W from W_{left} to W_{right} . The green and red vertical dashed lines
 571 show maximal invariant mass values that can be reached with W_{left} and W_{right} , respectively,
 572 while the vertical black dashed lines show the boundaries of the next to last bin in the
 573 invariant mass. As it is seen in Fig. 3.16 events in this bin with W between W_{left} and
 574 $M_{right}^{N_{bins}-1} = W_{center} - m_{X_3}$ are distributed in the range in $M_{X_1 X_2}$, which is less than invariant
 575 mass bin width defined by Eq. 3.6.2.

576 Correction for this effect is made using the new double pion event generator [33]. For
 577 that purpose for each invariant mass two one-dimensional distributions are generated in each
 578 W bin. The first one mimics the data distribution, for which all events in the next to last
 579 bin are divided by the same bin width defined by Eq. 3.6.2. For the second one events with
 580 W between W_{center} and W_{right} are divided by the same bin width defined by Eq. 3.6.2, while
 581 events with W between W_{left} and W_{center} are divided by the bin width that is individual
 582 for each event and equal to $W - m_{X_3} - M_{left}^{N_{bins}-1}$. The correction factor, by which obtained
 583 single-differential cross sections in the next to last bin should be multiplied, is defined as the
 584 ratio of the second distribution over the first one. This factor typically varies from 5% to
 585 10%.

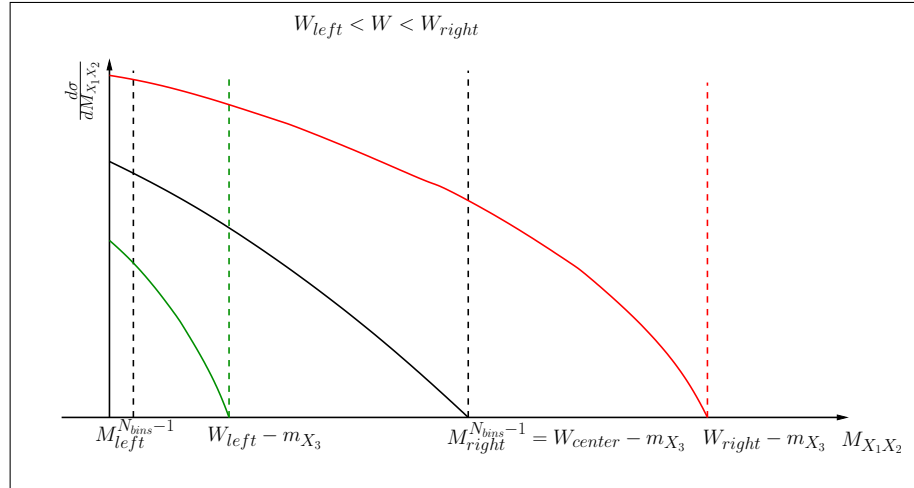


Figure 3.16: Schematic representation of the cross sections in the next to last bin in the invariant mass ($M_{X_1 X_2}$) for various W . Green and red vertical dashed lines show maximal invariant mass values that can be reached with W_{left} and W_{right} , respectively, while vertical black dashed lines show the boundaries of the next to last bin in the invariant mass.

Variable W range	Number of bins in invariant mass M	Number of bins in polar angle θ	Number of bins in azimuthal angle φ	Number of bins in angle between two planes α
1.3 - 1.35 GeV	8	6	5	5
1.35 - 1.4 GeV	10	8	5	6
1.4 - 1.45 GeV	12	10	5	8
> 1.45 GeV	12	10	8	8

Table 3.1: Number of bins for the given final hadron variables.

⁵⁸⁶ **Chapter 4**

⁵⁸⁷ **Cross section calculation**

⁵⁸⁸ **4.1 Kinematical variables**

⁵⁸⁹ After the double-pion event selection that uses the missing mass technique, the four-momenta
⁵⁹⁰ of all particles are known and can be used for the calculation of all kinematic variables. The
⁵⁹¹ cross sections are obtained in the single-photon exchange approximation in the center of
⁵⁹² mass frame of the *virtual photon – initial proton* system.

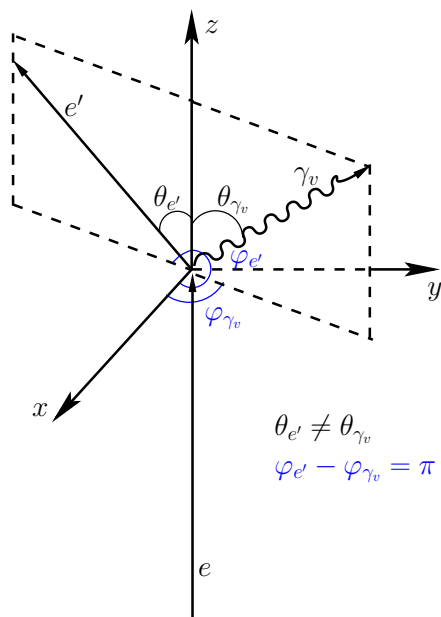


Figure 4.1: Virtual photon and scattered electron angles θ and φ in the lab frame.

593 Therefore, to calculate the kinematic variables the four-momenta of all particles need to
 594 be transformed from the lab frame to the c.m. frame. For that purpose Lorentz transforma-
 595 tions that include the following steps are used ¹.

596 1) Firstly (xy)-plane of the lab system is rotated around z -axis to make x -axis laying in
 597 the electron scattering plane (see Fig. 4.1). This rotation transforms the four-momentum as
 598 $P' = P * R_1$, with

$$R_1 = \begin{pmatrix} \cos(\varphi_{e'}) & -\sin(\varphi_{e'}) & 0 & 0 \\ \sin(\varphi_{e'}) & \cos(\varphi_{e'}) & 0 & 0 \\ 0 & 0 & 1 & 0 \\ 0 & 0 & 0 & 1 \end{pmatrix}, \quad (4.1.1)$$

599 where $\varphi_{e'}$ is the azimuthal angle of the scattered electron.

600 After this rotation $\varphi_{\gamma_v} = \pi$, since the φ angle between scattered electron and virtual
 601 photon is equal to π ; and after the rotation $\varphi_{e'} = 0$ with respect to the intermediate reference
 602 frame.

603 2) After that the lab system is rotated to align the z -axis with the virtual photon direction.
 604 The four-momentum transformation for this rotation is given by $P'' = P' * R_2$, with

$$R_2 = \begin{pmatrix} \cos(\theta_{\gamma_v}) & 0 & -\sin(\theta_{\gamma_v}) & 0 \\ 0 & 1 & 0 & 0 \\ \sin(\theta_{\gamma_v}) & 0 & \cos(\theta_{\gamma_v}) & 0 \\ 0 & 0 & 0 & 1 \end{pmatrix}, \quad (4.1.2)$$

605 where θ_{γ_v} is the polar angle of the virtual photon. ²

606 3) Finally a boost into the c.m. frame of the *virtual photon – initial proton* system is

¹In all derivations the energy is assumed to be the last component of the four-momentum and the four-momentum to be a row vector.

²Using embedded ROOT functions, both rotations can be coded using the unit vectors TVector3 $uz = P4_gamma.Vect().Unit()$ and TVector3 $ux = (P4_EL.Vect().Cross(P4_ELP.Vect())).Unit()$, where P4_gamma, P4_EL, and P4_ELP are the four-momenta of the virtual photon, initial and final electrons, respectively. The axis vector ux needs to be rotated according to $ux.Rotate(3.*M_PI/2,uz)$. Finally the rotation is defined as $rot.SetZAxis(uz,ux).Invert()$ and needs to be applied to the four-momentum (P4) of each particle: $P4.Transform(rot)$.

⁶⁰⁷ performed. It is given by the formula $P''' = P'' * R_3$, with

$$R_3 = \begin{pmatrix} 1 & 0 & 0 & 0 \\ 0 & 1 & 0 & 0 \\ 0 & 0 & \gamma & -\gamma\beta \\ 0 & 0 & -\gamma\beta & \gamma \end{pmatrix}, \quad \beta = \frac{|\vec{q}|}{E_\gamma + m_{proton}} = \frac{\sqrt{E_\gamma^2 + Q^2}}{E_\gamma + m_{proton}}, \quad \gamma = \frac{1}{\sqrt{1 - \beta^2}}, \quad (4.1.3)$$

⁶⁰⁸ where $|\vec{q}|$ is the magnitude of the three-vector of the virtual photon and β the magnitude
⁶⁰⁹ and z -component of the three-vector $\vec{\beta} = (0, 0, \beta)$. ³

⁶¹⁰ When the four-momenta of all particles in the c.m. frame are defined one can calculate
⁶¹¹ the kinematic variables that describe the final hadron state. The three-body final state is
⁶¹² unambiguously determined by five kinematic variables. Indeed, three final particles could be
⁶¹³ described by $4 \times 3 = 12$ components of their four-momenta. All these particles are on mass
⁶¹⁴ shell. So, it gives us three restrictions $E_i^2 - P_i^2 = m_i^2$ ($i = 1, 2, 3$). The energy-momentum
⁶¹⁵ conservation imposes four additional constraints for the final particles four-momenta com-
⁶¹⁶ ponents. So, eventually five kinematic variables remain, which determine unambiguously
⁶¹⁷ the three-body final state kinematics. In the electron scattering process $ep \rightarrow e'p'\pi^+\pi^-$ the
⁶¹⁸ variables W, Q^2 are also present besides the hadronic final state variables. So electron scat-
⁶¹⁹ tering cross section for double-charged pion electroproduction should be seven-differential:
⁶²⁰ five variables for the final hadrons plus W and Q^2 that are determined by the scattered elec-
⁶²¹ tron kinematics. Such seven-differential cross sections may be written as $\frac{d^7\sigma}{dWdQ^2d^5\tau}$, where
⁶²² $d^5\tau$ is five-dimensional phase space differential.

⁶²³ Several sets of five variables for the description of the final hadron kinematics may be
⁶²⁴ used. The following generalized set of variables is used in this analysis:

- ⁶²⁵ • invariant mass of the first pair of the particles M_{12} ;
- ⁶²⁶ • invariant mass of the second pair of the particles M_{23} ;
- ⁶²⁷ • the first particle solid angle Ω ;
- ⁶²⁸ • the angle α between two planes: one of them (plane A) is defined by the three-momenta
⁶²⁹ of the virtual photon (or initial proton) and the first final hadron, the second plane
⁶³⁰ (plane B) is defined by the three-momenta of all final hadrons (these angles are shown
⁶³¹ in Figs. 4.3, 4.4, 4.5 for various choices of the first particle).

⁶³² The cross sections in this analysis are obtained in three sets of variables depending on
⁶³³ various assignments for the first, second, and third final hadrons:

³ Note: if you use ROOT function `.Boost` you should change the sign of the z -component of β -vector:
`.Boost(0,0,-\beta)`.

- invariant mass of the $p'\pi^+$ pair, invariant mass of the $\pi^+\pi^-$ pair, proton spherical angles $\theta_{p'}$ and $\varphi_{p'}$ and angle $\alpha_{(p,p')(\pi^+,\pi^-)}$ (or $\alpha_{p'}$) between planes B (defined by the momenta of all final hadrons) and A (defined by initial and final protons), see Fig. 4.3;
- invariant mass of the $\pi^-\pi^+$ pair, invariant mass of the π^+p pair, π^- spherical angles θ_{π^-} and φ_{π^-} and angle $\alpha_{(\pi^-)(p\pi^+)}$ (or α_{π^-}) between planes B (defined by the momenta of all final hadrons) and A (defined by initial proton and π^-), see Fig. 4.4;
- invariant mass of the $\pi^+\pi^-$ pair, invariant mass of the π^-p pair, π^+ spherical angles θ_{π^+} and φ_{π^+} and angle $\alpha_{(\pi^+)(p\pi^-)}$ (or α_{π^+}) between planes B (defined by the momenta of all final hadrons) and A (defined by initial proton and π^+), see Fig. 4.5.

Lets explain in more detail the calculation of the kinematical variables in case of set number two. The invariant masses $M_{\pi^+\pi^-}$ and $M_{\pi^+p'}$ are calculated from the four-momenta of the final particles P_{π^-} , P_{π^+} , $P_{p'}$ in the c.m. frame in the following way

$$\begin{aligned} M_{\pi^+\pi^-} &= \sqrt{(P_{\pi^+} + P_{\pi^-})^2} \text{ and} \\ M_{\pi^+p'} &= \sqrt{(P_{\pi^+} + P_{p'})^2}. \end{aligned} \quad (4.1.4)$$

The angle θ_{π^-} between the three-momentum of the initial photon (\vec{P}_γ) and three-momentum of the final π^- (\vec{P}_{π^-}) in c.m. frame is calculated as:

$$\theta_{\pi^-} = \arccos \left(\frac{(\vec{P}_{\pi^-} \cdot \vec{P}_\gamma)}{|\vec{P}_{\pi^-}| |\vec{P}_\gamma|} \right) \quad (4.1.5)$$

The angle φ_{π^-} is determined as:

$$\begin{aligned} \varphi_{\pi^-} &= \arctg \left(\frac{P_{y\pi^-}}{P_{x\pi^-}} \right); P_{x\pi^-} > 0; P_{y\pi^-} > 0 \\ \varphi_{\pi^-} &= \arctg \left(\frac{P_{y\pi^-}}{P_{x\pi^-}} \right) + 2\pi; P_{x\pi^-} > 0; P_{y\pi^-} < 0 \\ \varphi_{\pi^-} &= \arctg \left(\frac{P_{y\pi^-}}{P_{x\pi^-}} \right) + \pi; P_{x\pi^-} < 0; P_{y\pi^-} < 0 \\ \varphi_{\pi^-} &= \arctg \left(\frac{P_{y\pi^-}}{P_{x\pi^-}} \right) + \pi; P_{x\pi^-} < 0; P_{y\pi^-} > 0 \\ \varphi_{\pi^-} &= \pi/2; P_{x\pi^-} = 0; P_{y\pi^-} > 0 \\ \varphi_{\pi^-} &= 3\pi/2; P_{x\pi^-} = 0; P_{y\pi^-} < 0, \end{aligned} \quad (4.1.6)$$

where $P_{i\pi^-}$ is i -component of the π^- three-momentum ($i = x, y, z$). The angles θ_{π^-} and φ_{π^-} are shown in Fig. 4.2.

651 The calculation of the angle α_{π^-} between two planes A and B (see Fig. 4.4) is more
 652 complicated. Firstly two auxiliary vectors $\vec{\gamma}$ and $\vec{\beta}$ should be determined. The vector $\vec{\gamma}$ is
 653 the unit vector perpendicular to the three-momentum \vec{P}_{π^-} , directed toward the vector $(-\vec{n}_z)$
 654 and situated in the plane A, which is defined by the three-momentum of initial proton and
 655 three-momentum of π^- . \vec{n}_z is the unit vector directed along z -axis. The vector $\vec{\beta}$ is the unit
 656 vector perpendicular to the three-momentum of π^- , directed toward the three-momentum
 657 of π^+ and situated in the plane B, which is defined by all final hadrons. Note that the three-
 658 momenta of π^+ , π^- , p' are in the same plane, since in c.m. frame their total three-momentum
 659 has to be equal to zero. Then the angle between two planes α_{π^-} is

$$\alpha_{\pi^-} = \arccos(\vec{\gamma} \cdot \vec{\beta}), \quad (4.1.7)$$

660 where \arccos is a function that runs between zero and π , while the angle α_{π^-} may vary between
 661 zero and 2π . To determine the α angle in the range between π and 2π the relative direction
 662 between the π^- three-momentum and the vector product $\vec{\delta} = [\vec{\gamma} \times \vec{\beta}]$ of the auxiliary vectors
 663 $\vec{\gamma}$ and $\vec{\beta}$ should be taken into account. If the vector $\vec{\delta}$ is colinear to the three-momentum of
 664 π^- , the angle α_{π^-} is determined by (4.1.7), and in a case of anti-collinearity by

$$\alpha_{\pi^-} = 2\pi - \arccos(\vec{\gamma} \cdot \vec{\beta}). \quad (4.1.8)$$

665 The defined above vector $\vec{\gamma}$ can be expressed as

$$\begin{aligned} \vec{\gamma} &= a_\alpha(-\vec{n}_z) + b_\alpha \vec{n}_{P_{\pi^-}} \quad \text{with} \\ a_\alpha &= \sqrt{\frac{1}{1 - (\vec{n}_{P_{\pi^-}} \cdot (-\vec{n}_z))^2}} \quad \text{and} \\ b_\alpha &= -(\vec{n}_{P_{\pi^-}} \cdot (-\vec{n}_z))a_\alpha, \end{aligned} \quad (4.1.9)$$

666 where $\vec{n}_{P_{\pi^-}}$ is the unit vector directed along the three-momentum of π^- (see Fig. 4.4).

667 Taking the scalar products $(\vec{\gamma} \cdot \vec{n}_{P_{\pi^-}})$ and $(\vec{\gamma} \cdot \vec{\gamma})$, it is straightforward to verify, that $\vec{\gamma}$ is
 668 the unit vector perpendicular to the three-momentum of π^- .

669 The vector $\vec{\beta}$ can be obtained as

$$\begin{aligned} \vec{\beta} &= a_\beta \vec{n}_{P_{\pi^+}} + b_\beta \vec{n}_{P_{\pi^-}} \quad \text{with} \\ a_\beta &= \sqrt{\frac{1}{1 - (\vec{n}_{P_{\pi^+}} \cdot \vec{n}_{P_{\pi^-}})^2}} \quad \text{and} \\ b_\beta &= -(\vec{n}_{P_{\pi^+}} \cdot \vec{n}_{P_{\pi^-}})a_\beta, \end{aligned} \quad (4.1.10)$$

670 where $\vec{n}_{P_{\pi^+}}$ is the unit vector directed along the three-momentum of π^+ .

671 Again taking the scalar products $(\vec{\beta} \cdot \vec{n}_{P_{\pi^-}})$ and $(\vec{\beta} \cdot \vec{\beta})$, it is straightforward to see, that
 672 $\vec{\beta}$ is the unit vector perpendicular to the three-momentum of π^- .

673 The angle α_{π^-} coincides with the angle between the vectors $\vec{\gamma}$ and $\vec{\beta}$. So, the scalar
 674 product $(\vec{\gamma} \cdot \vec{\beta})$ allows to determine the angle α_{π^-} (4.1.7). The kinematic variables for the
 675 other assignments for the first, second, and third final hadrons described above, are evaluated
 in the similar way.

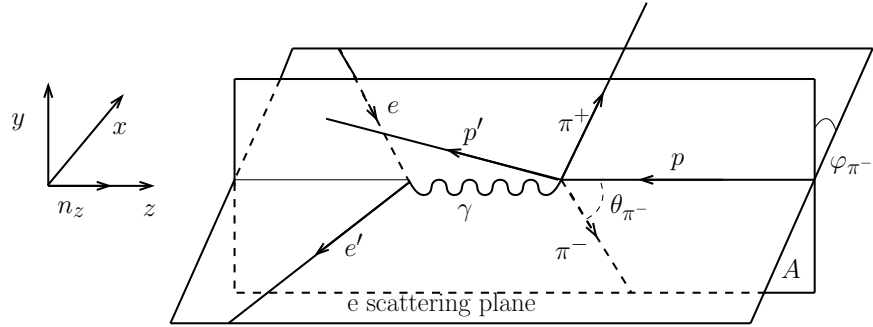


Figure 4.2: Polar (θ_{π^-}) and azimuthal (φ_{π^-}) angles of π^- in the c.m. frame.

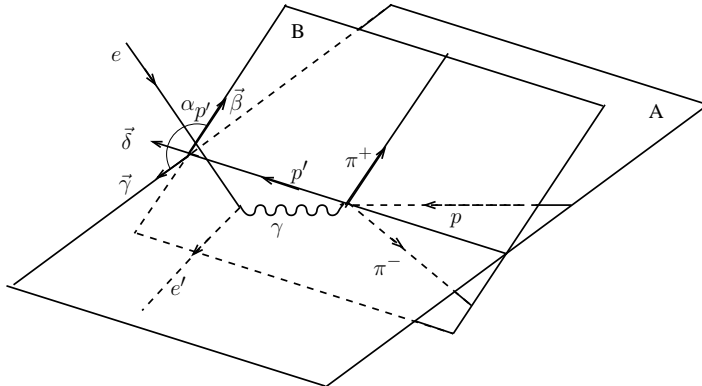


Figure 4.3: Definition of the angle $\alpha_{p'}$ between two planes: the plane B is defined by the three-momenta of all final hadrons, while the plane A defined by the three-momenta of initial and scattered protons. The definitions of auxiliary vectors $\vec{\beta}$, $\vec{\gamma}$, $\vec{\delta}$ are given in the text.

676
 677 Further detailed information about kinematic of the reactions with three-particle final
 678 states can be found here [34].

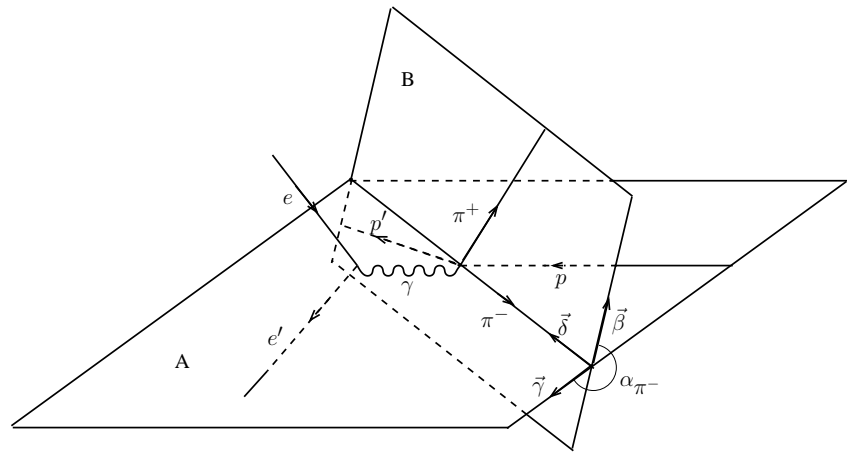


Figure 4.4: Definition of the angle α_{π^-} between two planes: the plane B is defined by the three-momenta of all final hadrons, while the plane A defined by the three-momenta of π^- and initial proton. The definitions of auxiliary vectors $\vec{\beta}$, $\vec{\gamma}$, $\vec{\delta}$ are given in the text.

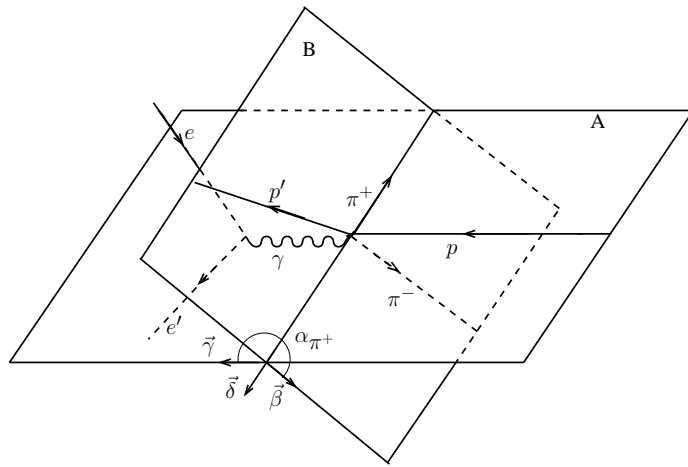


Figure 4.5: Definition of the angle α_{π^+} between two planes: the plane B is defined by the three-momenta of all final hadrons, while the plane A defined by the three-momenta of π^+ and initial proton. The definitions of auxiliary vectors $\vec{\beta}$, $\vec{\gamma}$, $\vec{\delta}$ are given in the text.

⁶⁷⁹ **4.2 Cross section formula**

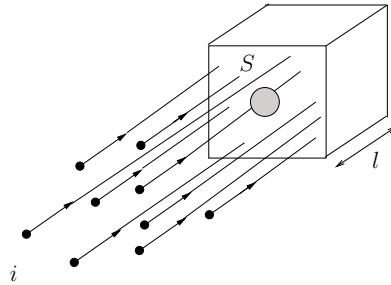


Figure 4.6: The incoming electron beam with the current i is hitting a homogeneous target with the area S and density ρ .

⁶⁸⁰ In the fixed target experiments (see Fig. 4.6) the interaction rate (the number of interactions per second) can be determined according to the following relation:

$$\frac{dN}{dt} = \frac{iN_{targ}\sigma}{S}, \quad (4.2.1)$$

⁶⁸² where i is the beam current (the number of incoming electrons per second), N_{targ} is the total ⁶⁸³ number of nuclei inside the target, S is the taget area, σ is the total cross section.

⁶⁸⁴ For i the following is true:

$$i = \frac{dN_{beam}}{dt} = \frac{1}{q_e} \frac{dQ}{dt}, \quad (4.2.2)$$

⁶⁸⁵ where N_{beam} is the number of incoming electrons, Q is the total charge that is carried by ⁶⁸⁶ incoming electrons, q_e is the elementary charge.

⁶⁸⁷ N_{targ} can be written in this way:

$$N_{targ} = \frac{mN_A}{M_m} = \frac{N_A\rho V}{M_m} = \frac{N_A\rho Sl}{M_m}, \quad (4.2.3)$$

⁶⁸⁸ where m , V , ρ , l are the mass, volume, density and length of the target, respectively, M_m is ⁶⁸⁹ the molar mass of the target material, N_A is the Avogadro constant.

⁶⁹⁰ From (4.2.1), (4.2.2) and (4.2.3) the cross section

$$\sigma = \frac{q_e \Delta NM_m}{Ql N_A \rho} = \frac{\Delta N}{L}, \quad (4.2.4)$$

⁶⁹¹ where $L = \frac{Ql N_A \rho}{q_e M_m}$ is the luminosity and Q is the total charge of incoming electrons accumulated in the Faraday cup.

693 Since this analysis is focused on the reaction $ep \rightarrow e'p'\pi^+\pi^-$, the quantity ΔN in the
 694 formula (4.2.4) is the total number of double-pion events. Liquid hydrogen is located in the
 695 target cell, hence the number of events that correspond to the target cell walls needs to be
 696 subtracted from the number of events that corresponds to the full target.

697 Taking into account that the charge accumulated in the Faraday cup is different for full
 698 (Q_{full}) and empty (Q_{empty}) target runs the formula for the total cross section can be rewritten
 699 as

$$\sigma = \frac{\frac{\Delta N_{full}}{Q_{full}} - \frac{\Delta N_{empty}}{Q_{empty}}}{\frac{l\rho N_A}{q_e M_m}}. \quad (4.2.5)$$

700 As it is mentioned in Sect. 4.1 the double-pion cross section depends on seven kinematical
 701 variables. For the second set of kinematical variables (see Sect. 4.1) considering formula
 702 (4.2.5) the seven-differential cross section can be written as

$$\frac{d\sigma}{dW dQ^2 dM_{p\pi^+} dM_{\pi^+\pi^-} d\Omega d\alpha_{\pi^-}} = \frac{1}{F \cdot R} \frac{\left(\frac{\Delta N_{full}}{Q_{full}} - \frac{\Delta N_{empty}}{Q_{empty}} \right)}{\Delta W \Delta Q^2 \Delta \tau \left(\frac{l\rho N_A}{q_e M_H} \right)}, \quad (4.2.6)$$

703 where ΔN_{full} and ΔN_{empty} are the numbers of events inside the seven-dimensional bin for
 704 runs with hydrogen and empty target, respectively. Each event is weighted with the cor-
 705 responding photoelectron correction factor given by Eq. 2.1.12. $F = F(\Delta W, \Delta Q^2, \Delta \tau)$ is the
 706 total efficiency coming from the Monte Carlo simulation, $R = R(\Delta W, \Delta Q^2)$ is the radiative
 707 correction factor, $Q_{full} = 5999.64 \mu\text{C}$ and $Q_{empty} = 334.603 \mu\text{C}$ are the integrated Faraday
 708 cup charges for runs with hydrogen and empty target, respectively. These charges are calcu-
 709 lated by summing up charges of all corresponding *blocks* that are used in the analysis. See
 710 the definition of *block* in Section 3.2. q_e is the elementary charge ($q_e = 1.610^{-19}\text{C}$), ρ is the
 711 density of liquid hydrogen ($\rho = 0.0708 \text{ g/cm}^3$) at $T = 20 \text{ K}$, l is the length of the target
 712 ($l = 2 \text{ cm}$), M_H is the molar density of the natural mixture of hydrogen ($M_H = 1.00794$
 713 g/mol), N_A is Avogadro's number ($N_A = 6.0210^{23} \text{ mol}^{-1}$), ΔW and ΔQ^2 are kinematical
 714 bins that are determined by the electron scattering kinematics, and $\Delta \tau$ is an element of the
 715 hadronic five-dimensional phase space

$$\Delta \tau = \Delta M_{p\pi^+} \Delta M_{\pi^+\pi^-} \Delta(-\cos(\theta_{\pi^-})) \Delta \varphi_{\pi^-} \Delta \alpha_{\pi^-}. \quad (4.2.7)$$

716 In the single photon exchange approximation, the electron scattering cross section is
 717 related to the hadronic cross section $\frac{d\sigma}{dM_{p\pi^+} dM_{\pi^+\pi^-} d\Omega_{\pi^-} d\alpha_{\pi^-}}$ by

$$\frac{d\sigma}{dM_{p\pi^+} dM_{\pi^+\pi^-} d\Omega_{\pi^-} d\alpha_{\pi^-}} = \frac{1}{\Gamma_v} \frac{d\sigma}{dW dQ^2 dM_{p\pi^+} dM_{\pi^+\pi^-} d\Omega_{\pi^-} d\alpha_{\pi^-}}, \quad (4.2.8)$$

718 where Γ_v is virtual photon flux, given by

$$\Gamma_v = \frac{\alpha}{4\pi} \frac{1}{E_{beam}^2 M_p^2} \frac{W(W^2 - M_p^2)}{(1 - \varepsilon)Q^2}, \quad (4.2.9)$$

where α is the fine structure constant ($1/137$), M_p is the proton mass, and ε is the virtual photon transverse polarization, given by

$$\varepsilon = \left(1 + 2 \left(1 + \frac{\omega^2}{Q^2} \right) \tan^2 \left(\frac{\theta_{e'}}{2} \right) \right)^{-1}, \quad (4.2.10)$$

where $\omega = E_{beam} - E_{scattered\ electron}$ and $\theta_{e'}$ is the angle of the scattered electron in the lab frame. W , Q^2 and $\theta_{e'}$ are taken in the center of the bin.

Limited statistics does not allow to estimate the five-differential cross section with reasonable accuracy. Therefore, the five-differential hadronic cross sections obtained in each bin in W and Q^2 are integrated in order to obtain the single-differential cross sections.

The following set of the single-differential cross sections are obtained for the second set of variables mentioned in Sect. 4.1:

$$\begin{aligned} \frac{d\sigma}{dM_{\pi^+\pi^-}} &= \int \frac{d^5\sigma}{d^5\tau} d\tau_{M_{\pi^+\pi^-}}^4; & d\tau_{M_{\pi^+\pi^-}}^4 &= dM_{\pi^+p} d\Omega_{\pi^-} d\alpha_{\pi^-} \\ \frac{d\sigma}{dM_{\pi^+p}} &= \int \frac{d^5\sigma}{d^5\tau} d\tau_{M_{\pi^+p}}^4; & d\tau_{M_{\pi^+p}}^4 &= dM_{\pi^+\pi^-} d\Omega_{\pi^-} d\alpha_{\pi^-} \\ \frac{d\sigma}{d(-\cos\theta_{\pi^-})} &= \int \frac{d^5\sigma}{d^5\tau} d\tau_{\theta_{\pi^-}}^4; & d\tau_{\theta_{\pi^-}}^4 &= dM_{\pi^+\pi^-} dM_{\pi^+p} d\varphi_{\pi^-} d\alpha_{\pi^-} \\ \frac{d\sigma}{d\alpha_{\pi^-}} &= \int \frac{d^5\sigma}{d^5\tau} d\tau_{\alpha_{\pi^-}}^4; & d\tau_{\alpha_{\pi^-}}^4 &= dM_{\pi^+\pi^-} dM_{\pi^+p} d\Omega_{\pi^-} \end{aligned} \quad (4.2.11)$$

with $d^5\tau = dM_{\pi^+\pi^-} dM_{\pi^+p} d\Omega_{\pi^-} d\alpha_{\pi^-}$.

For the two other sets of variables from Sect. 4.1 the single-differential cross sections can be obtained in a similar way.

In the actual cross section calculations the integrals in (4.2.11) are substituted by respective sums over the five-dimensional kinematical grid of hadronic cross sections.

To evaluate the absolute statistical error of the five-differential hadronic cross sections the following error propagation approach is used:

$$\delta_{stat}(M_{p\pi^+}, M_{\pi^+\pi^-}, \theta_{\pi^-}, \varphi_{\pi^-}, \alpha_{\pi^-}) = \frac{1}{F \cdot R} \frac{1}{\Gamma_v} \sqrt{\left(\frac{\Delta N_{full}}{Q_{full}^2} + \frac{\Delta N_{empty}}{Q_{empty}^2} \right)} \frac{\sqrt{\left(\frac{\Delta N_{full}}{Q_{full}^2} + \frac{\Delta N_{empty}}{Q_{empty}^2} \right)}}{\Delta W \Delta Q^2 \Delta \tau \left(\frac{l\rho N_A}{q_e M_H} \right)}. \quad (4.2.12)$$

Another source of statistical fluctuations is connected to the limited statistics in the Monte Carlo simulation. From (4.2.6) it is clear that the uncertainty in the efficiency F is affecting

736 the cross section value. The definition of efficiency factor F is simple:

$$F = \frac{N_{rec}}{N_{gen}}, \quad (4.2.13)$$

737 where N_{gen} and N_{rec} are the numbers of Monte Carlo generated and reconstructed events,
738 respectively.

739 Due to the fact that N_{gen} and N_{rec} are not independent the special approach needs to
740 be applied in order to calculate the statistical error of efficiency. This approach is described
741 in [35] and neglecting the events migration between the bins it gives the following expression
742 for the absolute statistical error in F

$$\delta(F) = \sqrt{\frac{(N_{gen} - N_{rec})N_{rec}}{N_{gen}^3}}. \quad (4.2.14)$$

743 It needs to be mentioned that kinematical cells where $N_{rec} >= N_{gen}$ are treated as empty
744 cells with no efficiency. Such cells are very rare and usually located near the edges of the
745 invariant mass distributions where the cross section is close to zero.

746 The absolute error on the cross section due to the limited Monte Carlo statistic is given
747 by

$$\delta_{stat,MC} = \frac{d\sigma}{dM_{\pi^+\pi^-} dM_{\pi^+p} d\Omega_{\pi^-} d\alpha_{\pi^-}} \left(\frac{\delta(F)}{F} \right) \quad (4.2.15)$$

748 Finally two statistical errors that come from fluctuation in the data and from the Monte
749 Carlo are combined quadratically, so the total absolute statistical error is given by

$$\delta_{stat,tot} = \sqrt{\delta_{stat,MC}^2 + \delta_{stat}^2}. \quad (4.2.16)$$

750 4.3 Radiative corrections

751 The radiative corrections are done using the new double-pion event generator (see Iu. Sko-
752 rodumina wiki page [33] and Sect 4.4). For that purpose double-pion events are generated
753 with and without radiative effects. After that radiative correction factor R in formula (4.2.6)
754 is determined by

$$R = \frac{N_{rad}^{2D}}{N_{norad}^{2D}}, \quad (4.3.1)$$

755 where N_{rad}^{2D} and N_{norad}^{2D} are the numbers of generated events in each (W, Q^2) bin with and
756 without radiative effects, respectively. The quantity one over R is plotted on the left side of
757 Fig. 4.7 as a function of W for various Q^2 bins. As it can be seen in Fig. 4.7 the dependence
758 of the radiative correction factor on Q^2 is rather small. So, for the actual cross section
759 calculations the factor R is averaged over all Q^2 bins (see right side of Fig. 4.7). The

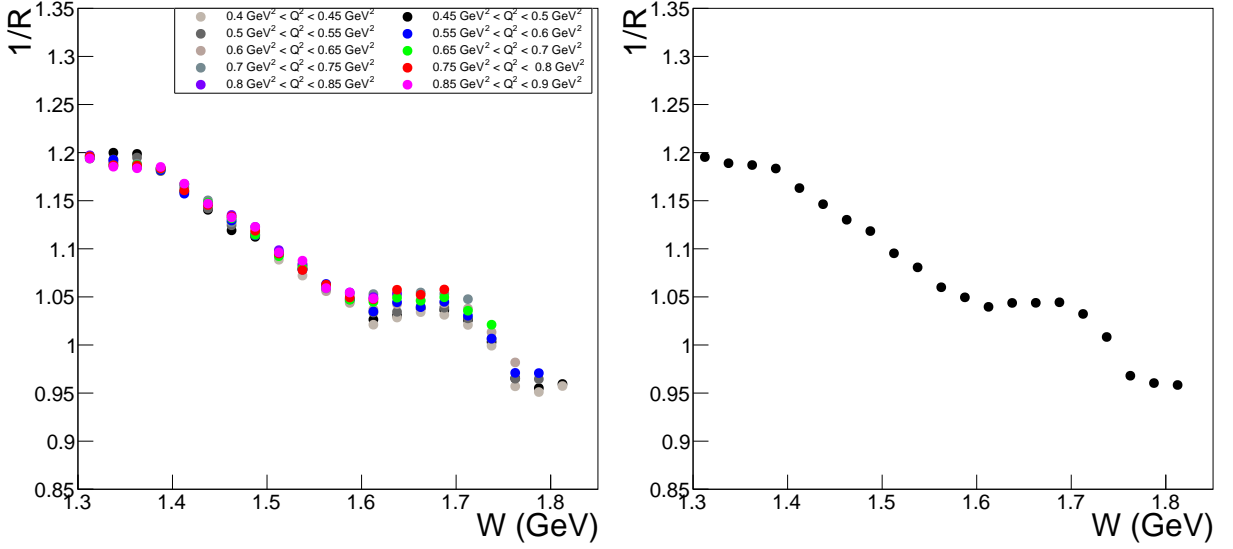


Figure 4.7: One over radiative correction factor (see formula 4.2.6) as function of W , for various bins over Q^2 (left plot) and averaged over all Q^2 bins (right plot).

760 statistical uncertainties associated with the number of generated events are also small and
761 not seen in Fig. 4.7.

762 It should be noted that to account for radiative effects, the new double-pion event gen-
763 erator uses the well known approach taken from Mo and Tsai [31]. In this approach the soft
764 part is evaluated explicitly, while for the calculation of the hard part the "inclusive" hadronic
765 tensor is used. The applicability of this approximation for the hard part of radiative effects
766 is subject of special attention. The single-differential double-pion cross sections (4.2.11)
767 obtained in this analysis represent the over four variables integrated five-differential cross
768 sections. This integration considerably reduces the influence of the final hadron kinematics
769 on the radiative correction factor. Therefore, the "inclusive" Mo and Tsai procedure is in
770 the case of double-pion cross sections more applicable than in a case of non-integrated cross
771 sections that are typically obtained for instance in the single-pion data analysis.

772 It also should be mentioned that this correction should be applied before the empty cells
773 (see Sect. 4.5) are filled, since the cross sections that are used for the purpose of filling empty
774 cells are already corrected for radiative effects.

775 4.4 Efficiency evaluation

776 For the efficiency calculation the Monte Carlo event generator of the Genova group is used.
777 This event generator uses the JM05 model [36] for double-pion channel. Although the cross

sections on which the event generator is based do not include the latest modifications of the JM model [7–9], it describes the data well enough to use it for the purpose of the efficiency evaluation.

To take into account the multi-pion background, three-pion events are generated simultaneously with the double-pion ones, the relative weight of these two channels is determined according to their integral cross sections at the photon point, see Fig. 4.8. The event generator does not assume any model for the channel $ep \rightarrow e'p'\pi^+\pi^-\pi^0$, so for this channel phase space distributions are generated. It needs to be mentioned that even at high W (around 1.8 GeV) three-pion background contributes only few percent to the double-pion events that survive after the exclusivity cut (see Sect. 3.4).

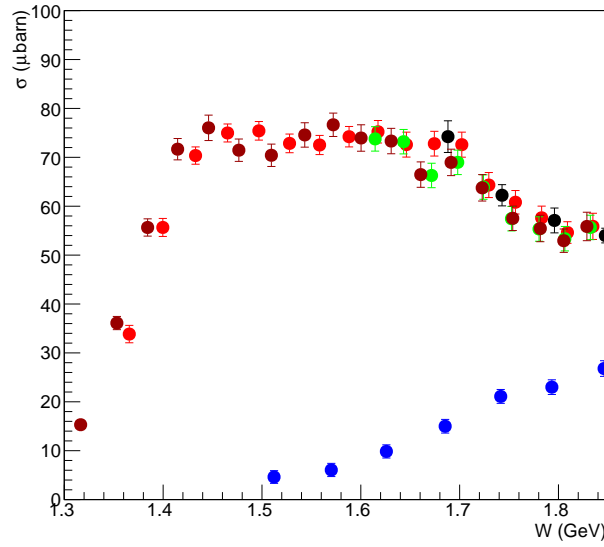


Figure 4.8: Integral cross sections of the reactions $ep \rightarrow e'p'\pi^+\pi^-$ and $ep \rightarrow e'p'\pi^+\pi^-\pi^0$ at the photon point. Black and red circles are double-pion data from [32]. Green and brown circles are double-pion data from [37]. Blue circles are three-pion data from [38].

All generated events are passed through GSIM, GPP and RECSIS. The parameters for the simulation are taken to be the same as in [39]. After applying all cuts and corrections described above, the reconstructed events are compared with the data. As it is seen on the left side of Fig. 4.9 MC reconstructed events reproduce the data rather well.

On the right side of Fig. 4.9 the average efficiency in five-dimensional kinematical cell is shown as functions of the hadron variables that describe the double-pion final state. No distributions show any significant efficiency variation.

The efficiency in some five-dimensional cells is not determined precisely enough, this leads to the fact that the cross sections obtained in them are not reliable. These cells should be excluded from the analysis and treated as empty cells (see Sect. 4.5). In order to determine

the criterion for cell exclusion the distribution shown in Fig. 4.10 is produced. This figure shows the relative efficiency error (absolute efficiency error is given by 4.2.14) that is plotted versus efficiency, color code in this figure represents the number of five-dimensional cells. As it is seen in Fig. 4.10 cells with relative efficiency errors greater than 30% are clustered along horizontal stripes. This effect can be explained taking into account that efficiency is obtained by division of two integer numbers, and it indicates too small statistics of generated events that in turn leads to higher efficiency errors. Moreover these horizontal stripes contain many cells with extremely small efficiency values that one can not count on anyway. Therefore, the five-dimensional cells that are located above the horizontal red line in Fig. 4.10 are excluded from the analysis and treated as empty cells (see Sect. 4.5).

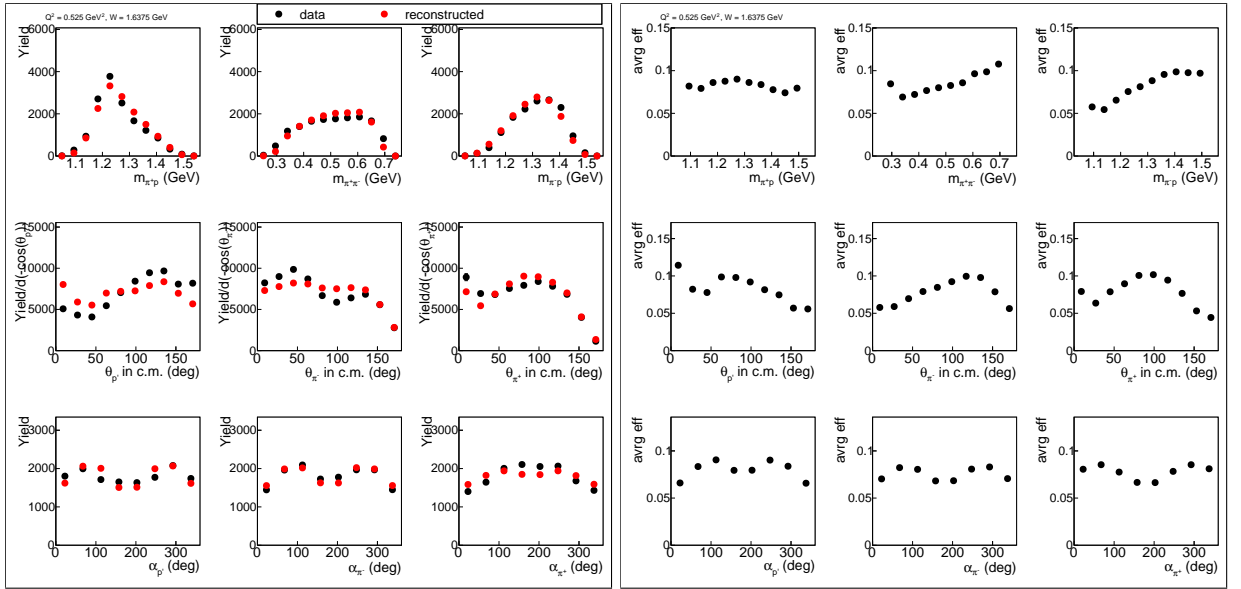


Figure 4.9: Plots in the left frame show the comparison of data and reconstructed MC yields as functions of various hadronic variables that describe the double-pion final state. Plots in the right frame show the average efficiency in the five-dimensional kinematical cell as functions of the final state hadronic variables. All distributions are given for one particular bin in W and Q^2 ($W = 1.6375 \text{ GeV}$, $Q^2 = 0.525 \text{ GeV}^2$).

4.5 Filling kinematical cells with zero acceptance

Since the CLAS detector does not cover full 4π solid angle, there are some blind areas or so-called "empty cells" in the kinematic phase space of the double-pion production. In the case when fully differential cross sections are obtained (for example in single pion production analyses) the presence of these cells is not a problem of big importance. Due to the statistical limitations in the double-pion analyses only the single-differential cross sections

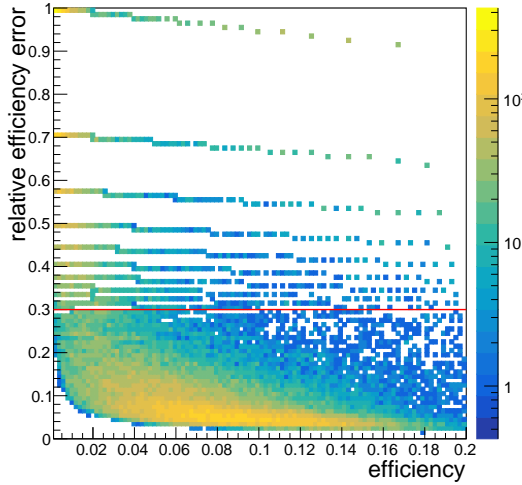


Figure 4.10: Relative efficiency error versus efficiency for one particular bin in W and Q^2 ($W = 1.6375$ GeV, $Q^2 = 0.525$ GeV 2). Color code shows the number of five-dimensional cells.

can be obtained. It means that the five-differential cross sections need to be integrated over four variables (see formulae 4.2.11). To obtain correct integrals, some assumptions on the cross sections in the empty cells are needed. It makes the problem of filling empty cells a point of special attention.

The map of the empty cells is determined by the Monte Carlo simulation. A cell is treated as empty, if it contains generated events, but does not contain any reconstructed events. One should not confuse these cells with those that contain both generated and reconstructed events, but do not contain data. The latter do not contain real events due to the limited experiment duration, and should not be filled since normalization on the charge in Faraday cup is applied.

To consider contributions from empty cells to the integrals (4.2.11) in detail model assumptions on the cross sections in these cells are needed. Recently for the purpose of the development of new double-pion event generator [33] a special procedure that allows to obtain the five-differential double-pion cross sections in the given kinematical cell was worked out. This procedure employs the five-differential cross sections from the recent version of the JM15 model fit to all results on charged double pion photo- and electroproduction cross sections from CLAS (both published and preliminary [1, 6, 7, 40]). In the area not yet covered by CLAS data an additional extrapolation technique was applied, that included additional world data on W dependencies of double-pion photoproduction integrated cross sections [32, 37]. The set of the cross sections obtained using this procedure was used for the purpose of filling empty cells in this analysis.

In Fig. 4.11 the single-differential cross sections are plotted for the two cases: when empty cells are not filled (red circles) and when empty cells are filled by the way described above

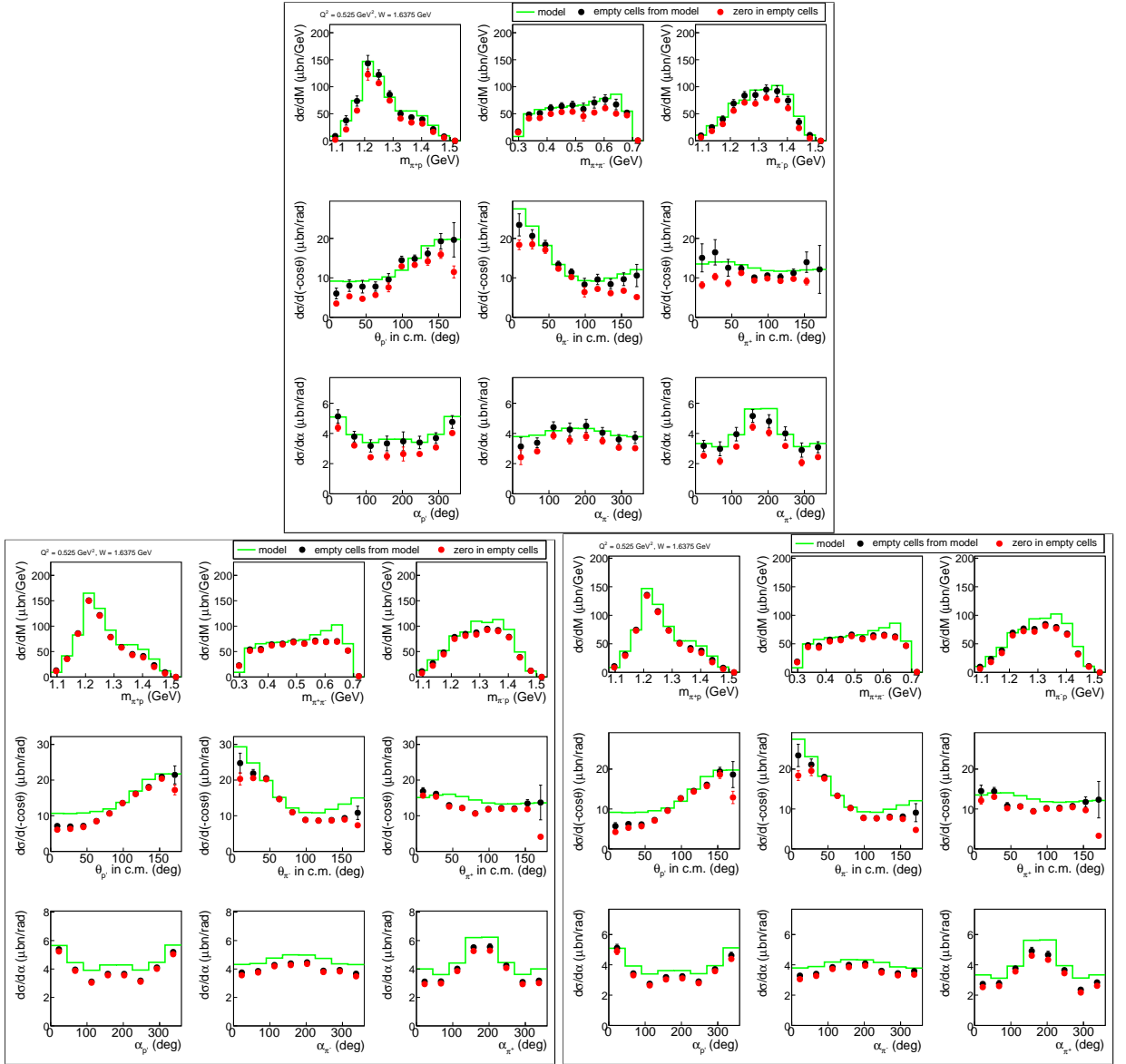


Figure 4.11: Comparison of various ways of combining topologies. Plots in the top frame are for the case when the cross sections are obtained using the topology where π^- is missing combined with the exclusive topology. Plots in the bottom left frame are for the case when the cross sections are obtained using the sum of data and reconstructed events for all four topologies. Plots in the bottom right frame are for the case when the cross sections are obtained using the selection of five-dimensional cells based on the maximum efficiency. See text for more details. In all plots the red circles are for the cross sections with unfilled empty cells and the black circles are for the cross sections with filled empty cells. Green curves show the cross sections that are used for the purpose of filling empty cells. All distributions are given for one particular bin in W and Q^2 ($W = 1.6375 \text{ GeV}$, $Q^2 = 0.525 \text{ GeV}^2$).

(black circles). The cross sections that are used to fill empty cells are shown by the green curves. The plot in the top frame of Fig. 4.11 corresponds to the topology where π^- is missing combined with the exclusive topology, while the two plots in the bottom frames correspond to different ways of combining of all available topologies (ways in which the topologies may be combined are described in more detail in Sect. 4.6).

The plot in the left bottom frame in Fig. 4.11 corresponds to the method of the topologies combination that is selected to be the best. As it can be seen in the left bottom frame in Fig. 4.11 the contribution from empty cells to the total cross sections is reasonably small. Although the cross sections that are used to fill empty cells describe the data well an additional 50% relative error is assigned to the part of the cross section that comes from the empty cell contributions. For finally obtained cross sections (shown by black circles) this additional error is combined with the total statistical one.

4.6 Combination of various topologies

It is mentioned in Sect. 3.4 that the topology where π^- is missing combined with the exclusive one accounts about 80% of all double-pion events. In previously published analyses [6, 41] only these two topologies were used to obtain final cross sections.

In this analysis it is found that the use of only the combination of the exclusive and π^- missing topologies leads to significant contributions from empty cells to the total cross sections in some phasespace regions (see plot in the top frame of Fig. 4.11). Moreover, the last point in θ_{π^+} angular distribution does not contain data at all and the cross section in this point is totally determined by the procedure of filling empty cells as described in Sect. 4.5.

Hence to minimize the part of the cross section that comes from filling of the empty cells and therefore the model dependence of the obtained cross sections, it was decided to use all available topologies.

There are two methods in which topologies can be combined. One of them is chosen as preferable and used to obtain the final cross sections. In this method data events for all topologies are summed up in each five-dimensional kinematical cell. The same is done for the reconstructed events, while the number of generated events remains the same. Then the cross sections are calculated in a usual way. The cross sections for the case when all topologies are combined by this method are shown in the bottom left frame of Fig. 4.11. One can see that the usage of this method allows to minimize the part of the cross section that comes from the empty cells contributions in comparison with the case when only the exclusive and π^- missing topologies are used. Moreover even the last point in θ_{π^+} angular distribution now is partially determined by data and therefore less model dependent.

Another way to combine topologies is used to check the consistency of the results. In this way in each five-dimensional kinematical cell reconstructed and data events are taken from

873 the topology that has maximum efficiency, while the number of generated events remains the
874 same. The cross sections that are obtained using this method are shown in the bottom right
875 frame of Fig. 4.11. Although this method gives almost the same result as the previous one,
876 it has several shortcomings. One of them is slightly bigger contribution from empty cells.
877 Another one is the fact that this method does not allow to use the whole available statistics
878 of the data. As a result the error of the obtained cross sections becomes a little bit higher
879 than in the previous method. That is why this method is not chosen as a primary one. The
880 difference between the cross sections obtained by the two methods described above is used
881 as part of the systematical error of the integrated cross sections (see Sect. 6.2).

882 Finally it needs to be mentioned that independently of the way the cross sections are
883 calculated (see all plots in Fig. 4.11), the final cross sections obtained after filling the empty
884 cells are very close to each other. That indicates the stability and reliability of the cross
885 section extraction procedure.

⁸⁸⁶ **Chapter 5**

⁸⁸⁷ **Correction for binning effects**

⁸⁸⁸ Since the bins in which the cross sections are obtained have finite sizes, the cross section
⁸⁸⁹ values can be distorted due to the averaging within the bins. For instance, if there is a
⁸⁹⁰ sharp peak in the middle of a bin, then the average value of the cross section in that bin
⁸⁹¹ will always be smaller than the peak value. Any non-linear behavior of the cross section will
⁸⁹² likely result in an offset of the obtained value. There are two ways to deal with this issue.
⁸⁹³ Either one uses the corrected values of the kinematical quantities associated with the bin,
⁸⁹⁴ instead of the central values or one calculates the correction to the cross section in the center
⁸⁹⁵ of the bin. In this analysis the second method is chosen, in order to keep the initial binning
⁸⁹⁶ over kinematical variables. For that purpose some model assumption about the cross section
⁸⁹⁷ behavior is needed. The ratio of the model value at the center of the bin to the model value
⁸⁹⁸ averaged within the bin is considered as a multiplicative correction factor, and the corrected
⁸⁹⁹ cross section is found as

$$\sigma_{corr} = \sigma_{uncorr} \times C_{bin} \quad \text{with} \\ C_{bin} = \frac{\sigma_{model,cntr}}{\sigma_{model,avg}}, \quad (5.0.1)$$

⁹⁰⁰ where σ_{uncorr} is the experimental cross section value before binning corrections, $\sigma_{model,cntr}$
⁹⁰¹ is the cross section from the model in the center of the data bin, and $\sigma_{model,avg}$ is the cross
⁹⁰² section from the model averaged in data bin.

⁹⁰³ In the first step the corrections are applied to all single-differential cross sections. For
⁹⁰⁴ the model cross sections the cubical spline approximation is chosen. The results are shown
⁹⁰⁵ in Fig. 5.1. The black and red points in this figure stand for the cross sections before
⁹⁰⁶ and after binning corrections, respectively, while the curves correspond to the model. For
⁹⁰⁷ the invariant masses and θ angular distributions splines are forced to pass through the
⁹⁰⁸ intermediate points that are obtained by averaging of two neighboring cross section points.
⁹⁰⁹ This method reduces the splines sensitivity to accidental cross section fluctuations. For the
⁹¹⁰ α distributions another method is chosen. As it seen in Fig. 4.11 the obtained α distributions
⁹¹¹ are slightly asymmetrical. However after the integration over φ , the cross section must be

symmetrical with respect to the α angle. So, it was decided to force the splines to pass through the points that are obtained by averaging the cross section values in the points that are symmetrical with respect to $\alpha = 180^\circ$.

After that the corrected single-differential cross sections are integrated and corrected to the Q^2 dependence inside the Q^2 bins and the W dependence inside the W bins. In Fig. 5.2 integrated cross sections are shown as functions of Q^2 (left plot) and W (right plot) before (black points) and after (red points) binning corrections. To fit the Q^2 dependencies a second order polynom is chosen, while for W distributions cubical splines are the best choice (splines are forced to pass through the intermediate points that are obtained by averaging two neighboring cross section points). These assumptions for Q^2 and W cross sections behaviors are shown by the curves in Fig. 5.2.

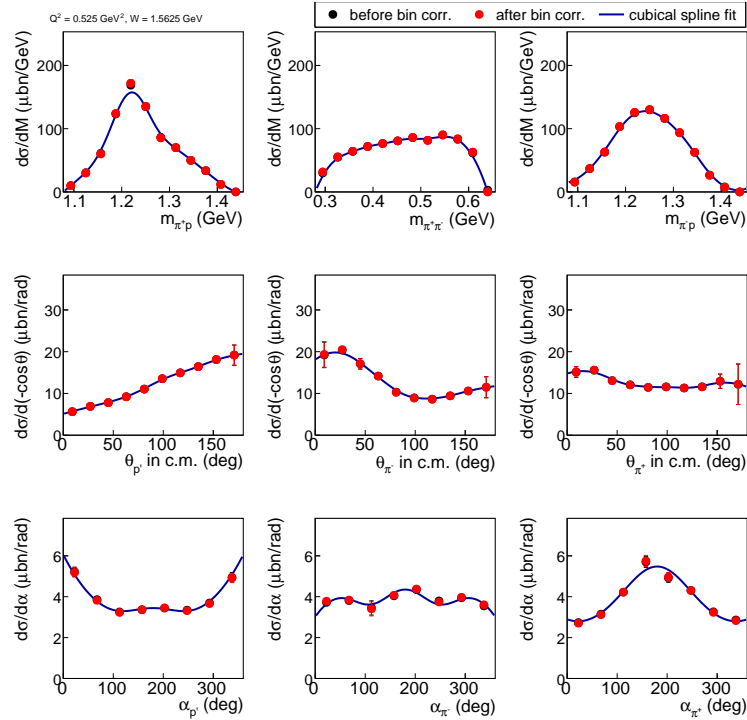


Figure 5.1: The single-differential cross sections as functions of the final hadron variables for one particular bin in W and Q^2 ($W = 1.5625 \text{ GeV}$, $Q^2 = 0.525 \text{ GeV}^2$) before (black points) and after (red points) the binning corrections. Curves stand for the cubical spline approximation.

Since in this analysis the detailed binning over all kinematical variables is chosen, the effect of the binning correction is rather small ($\sim 1\%$) and only in some points at low W it can rise up to 4%. That is why in the Figs. 5.1 and 5.2 the black points (before the correction) are almost completely covered up by the red ones (after the correction).

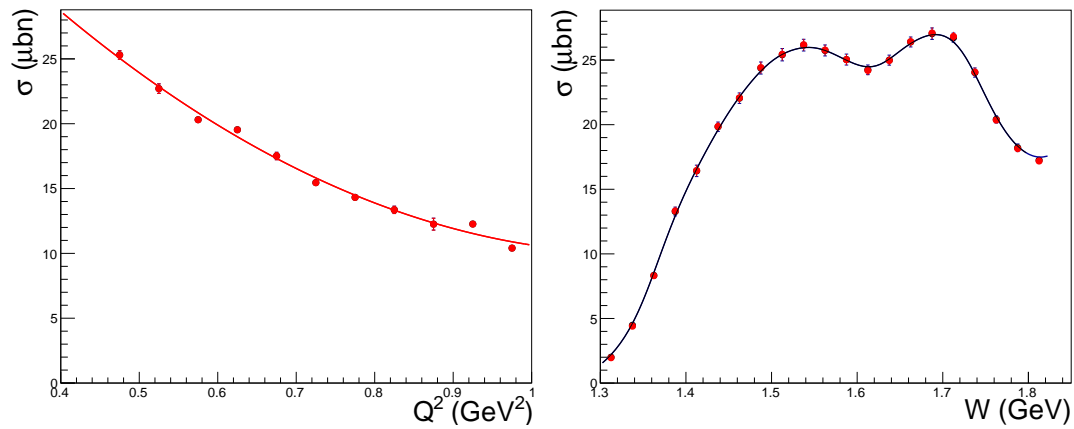


Figure 5.2: Q^2 dependence of integral cross section at $W = 1.4625 \text{ GeV}$ (left plot) and W dependence of integral cross section at $Q^2 = 0.475 \text{ GeV}^2$ (right plot). On both plots black and red points correspond to the cross sections before and after the binning corrections, respectively. The curve on the left plot represents the second order polinomial fit, while the curve on the right plot correspond to the cubical spline approximation.

₉₂₇ **Chapter 6**

₉₂₈ **Systematical errors**

₉₂₉ **6.1 Errors due to normalization, electron identifica-**
₉₃₀ **tion, and electron detection efficiency**

₉₃₁ One of the main sources of systematical errors in this experiment is the uncertainty in
₉₃₂ the normalization. This can arise from miscalibrations of the Faraday cup, target density
₉₃₃ instabilities, and errors in determining the target length and its temperature, DAQ live-time,
₉₃₄ and other factors. However, the presence of the elastic events in the data set allows to check
₉₃₅ the normalization of the cross sections by comparing the elastic cross sections to the world
₉₃₆ data. In this way one can combine normalization, electron detection, electron tracking,
₉₃₇ and electron identification errors into one global uncertainty factor. In Fig. 6.1 the ratio of
₉₃₈ the measured elastic cross section to a parametrization of the elastic cross sections [42] is
₉₃₉ shown. The parametrized cross sections are "radiated" and the elastic cross sections from
₉₄₀ the CLAS data are not corrected for radiative effects. As it is seen in Fig. 6.1, all the points
₉₄₁ are within the green lines that indicate $\pm 5\%$ offsets. This procedure allows to assign a 3%
₉₄₂ global uncertainty due to normalization, electron identification, and electron efficiency.

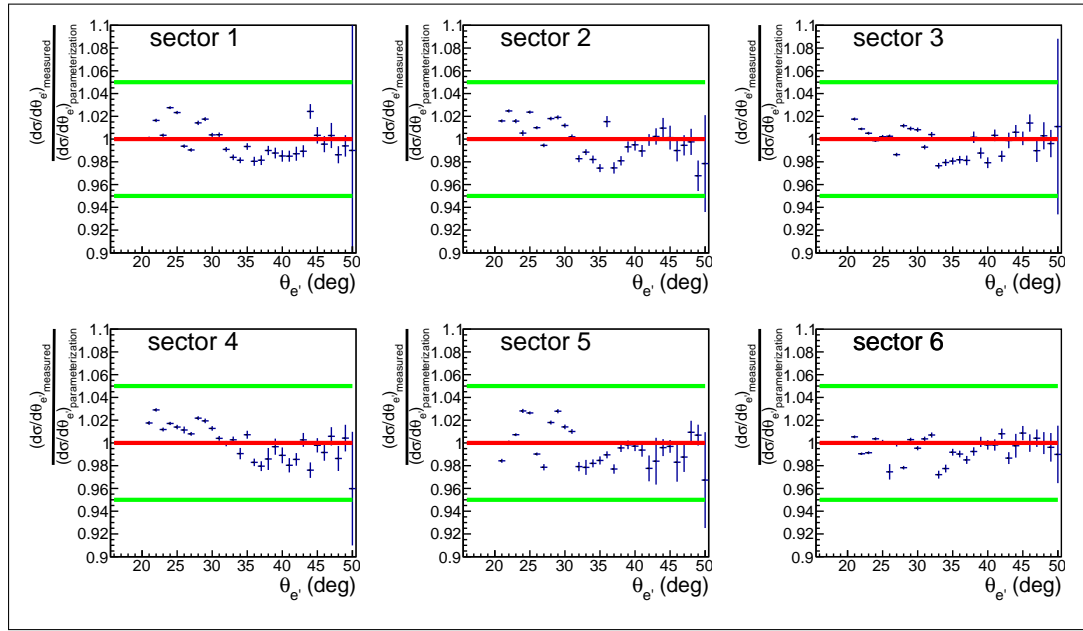


Figure 6.1: Ratio of the elastic cross section to the parametrization [42], plotted versus θ_e' angle of the electron in the lab frame for the six CLAS sectors. Red lines correspond to unity and green lines indicate a $\pm 5\%$ deviation from the parametrization.

943 6.2 Errors due to the different ways of combining 944 topologies

945 In this analysis two ways of combining topologies are used (see Sect. 4.6). The integrated
946 cross sections obtained in these two ways are slightly different. As in the case of the integra-
947 tion over different kinematical grids, this difference is interpreted as systematical error.
948 Since different topologies correspond to the different registered final hadrons (and therefore
949 to the different hadron cut combinations) this systematical error includes partially the error
950 due to the shapes of the cuts that are used in the analysis. The error is calculated for each
951 bin in W and Q^2 and typically is of the order of 2%.

952 6.3 Errors due to the integration over different final 953 hadron variables

954 As it is mentioned in Sect. 4.1 three sets of kinematical variables are used in this analysis. The
955 cross sections obtained by integration over these three kinematical grids should be the same.
956 However, it is found that they are slightly different due to the fact that data and efficiency
957 propagate differently to the different kinematical grids. This difference is interpreted as

958 systematical error and computed for each bin in W and Q^2 . This systematic effect varies
 959 depending on the bin in W and Q^2 and is typically of the order of 5%.

960 6.4 Systematical error summary

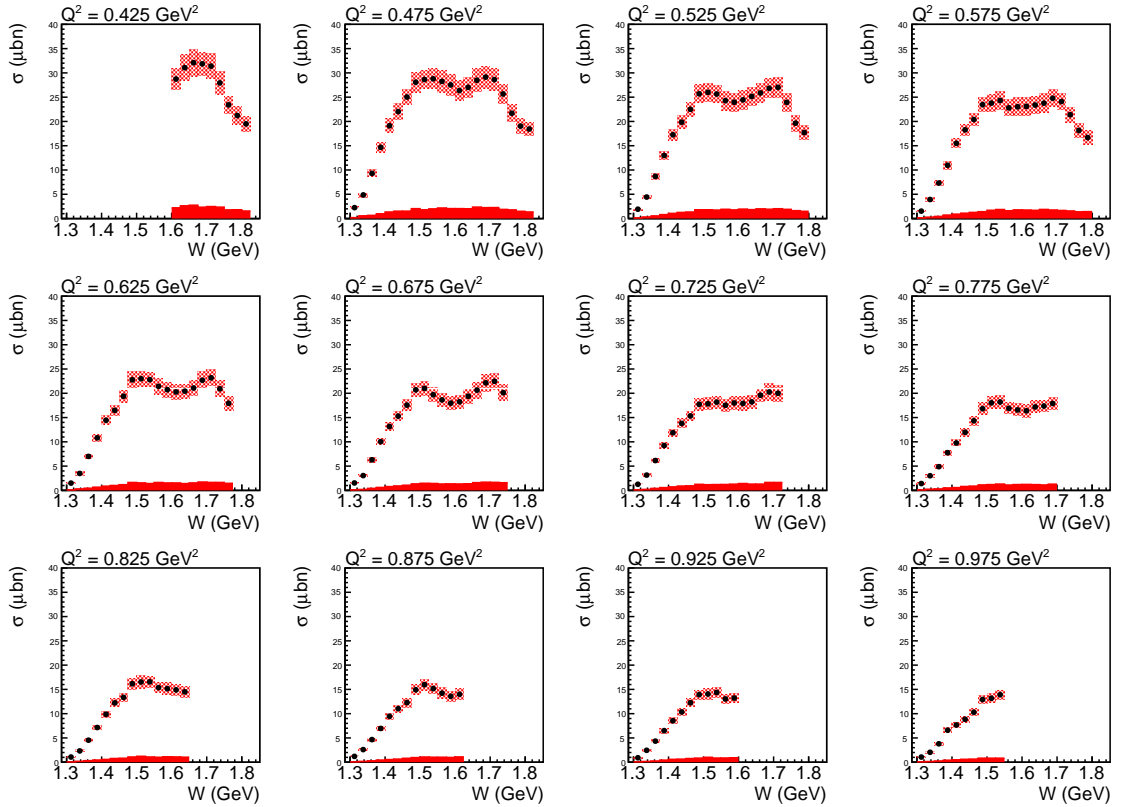


Figure 6.2: Systematical errors of the integrated cross sections. The plots show W dependencies of the integrated cross section in various bins in Q^2 . The systematical uncertainties are shown as the red bands at the bottom of each plot. The total cross section uncertainty (both statistical and systematical ones summed up in quadrature) is shown by the hatched red areas.

961 As final integrated cross sections, the cross sections that are averaged over three grids of
 962 the kinematical variables are reported (see Fig. 6.2). In Fig. 6.2 the systematical uncertainties
 963 are shown as the red bands at the bottom of each plot. This uncertainties include the errors
 964 due to the effects mentioned above and extra 5% global error due to the inclusive radiative
 965 corrections procedure (see Sect. 4.3). To obtain the red bands all the errors are summed up
 966 in quadrature.

967 The statistical cross section uncertainties are typically smaller than the systematical ones.

⁹⁶⁸ The total uncertainty is obtained as the sum of the systematical and statistical ones and is
⁹⁶⁹ shown by the hatched red areas in Fig. 6.2.

⁹⁷⁰ The typical values of the integral systematical errors with their sources are presented in
⁹⁷¹ Tab. 6.1.

Error source	Error value
Normalization, electron id, and electron detection efficiency	3%
Different ways of combining topologies	$\sim 2\%$
Integration over different final hadron variables	$\sim 5\%$
Radiative corrections	5%

Table 6.1: The typical values of the integral systematical errors.

₉₇₂ **Chapter 7**

₉₇₃ **Conclusions**

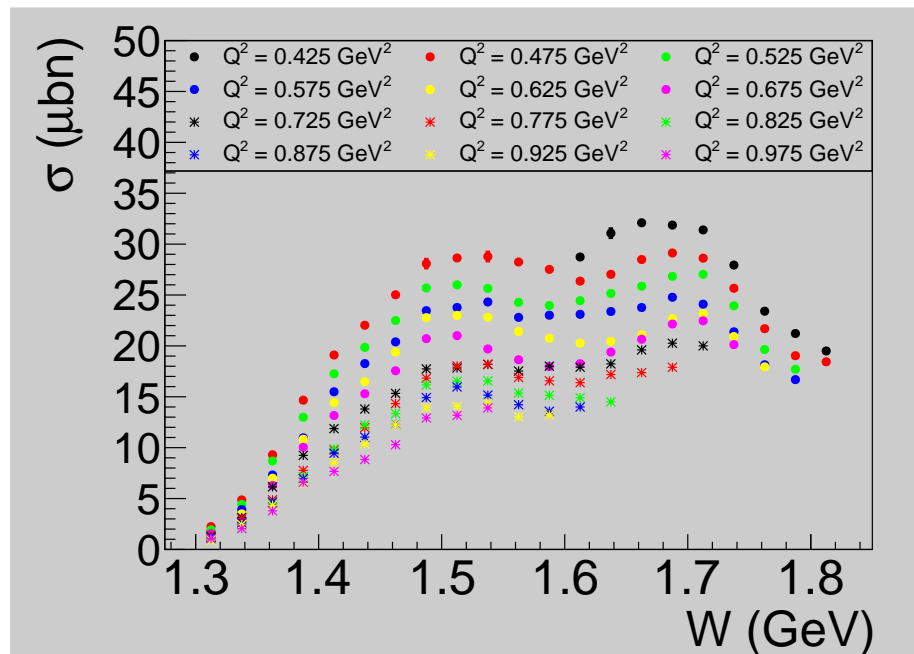


Figure 7.1: W dependencies of the integrated cross sections for various bins in Q^2 . The statistical errors are small and invisible under the symbols.

- ₉₇₄ • The complete set of the single-differential (see appendix A) and integrated cross sections (see Fig. 7.1) for the reaction $\gamma_v p \rightarrow p\pi^+\pi^-$ is obtained in the range of W from 1.3 GeV to 1.825 GeV and Q^2 from 0.45 GeV^2 to 1 GeV^2 . The Q^2 binning of the cross sections in the kinematical area of high-lying nucleon resonances is six times finer than in previously available data.
- ₉₇₅
- ₉₇₆
- ₉₇₇
- ₉₇₈

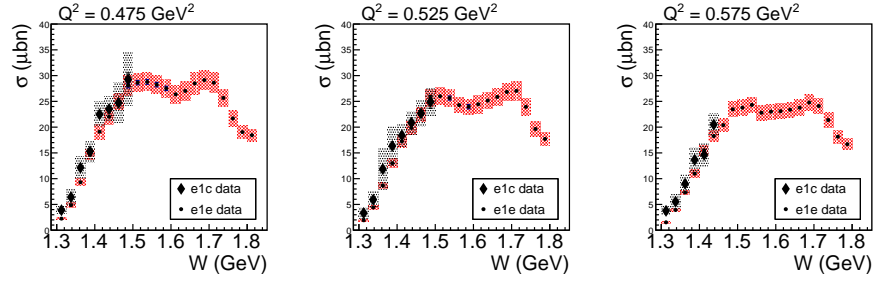


Figure 7.2: W dependencies of the obtained in this analysis cross sections (e1e dataset) in comparison with the cross sections from [6] (e1c dataset) for three bins in Q^2 . Hatched areas correspond to the total uncertainties (sistemtical and statistical).

- 979 • The comparison of the obtained cross sections with the available ones [6] shows the
980 reasonable agreement within the statistical uncertainties (see Fig. 7.2). It needs to be
981 mentioned that this comparison is not fully justified since the cross sections from [6]
982 and this analysis are obtained with different beam energies.
- 983 • The fit of these data by the meson-baryon reaction model JM [7–9] will provide for the
984 first time information on the Q^2 evolution of high-lying resonances with very detailed
985 binning.

⁹⁸⁶ **Appendix A: Measured cross sections**

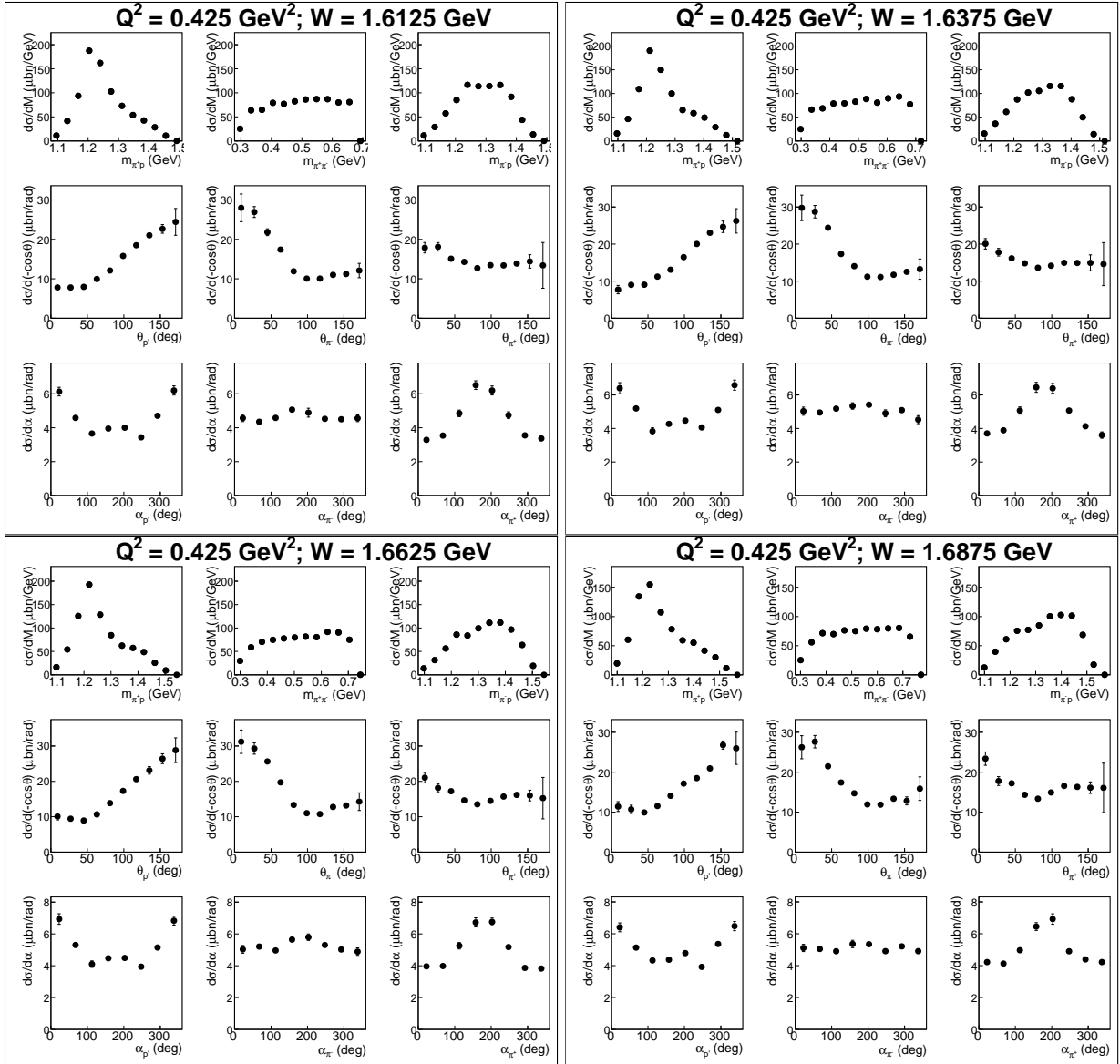


Figure A.1:

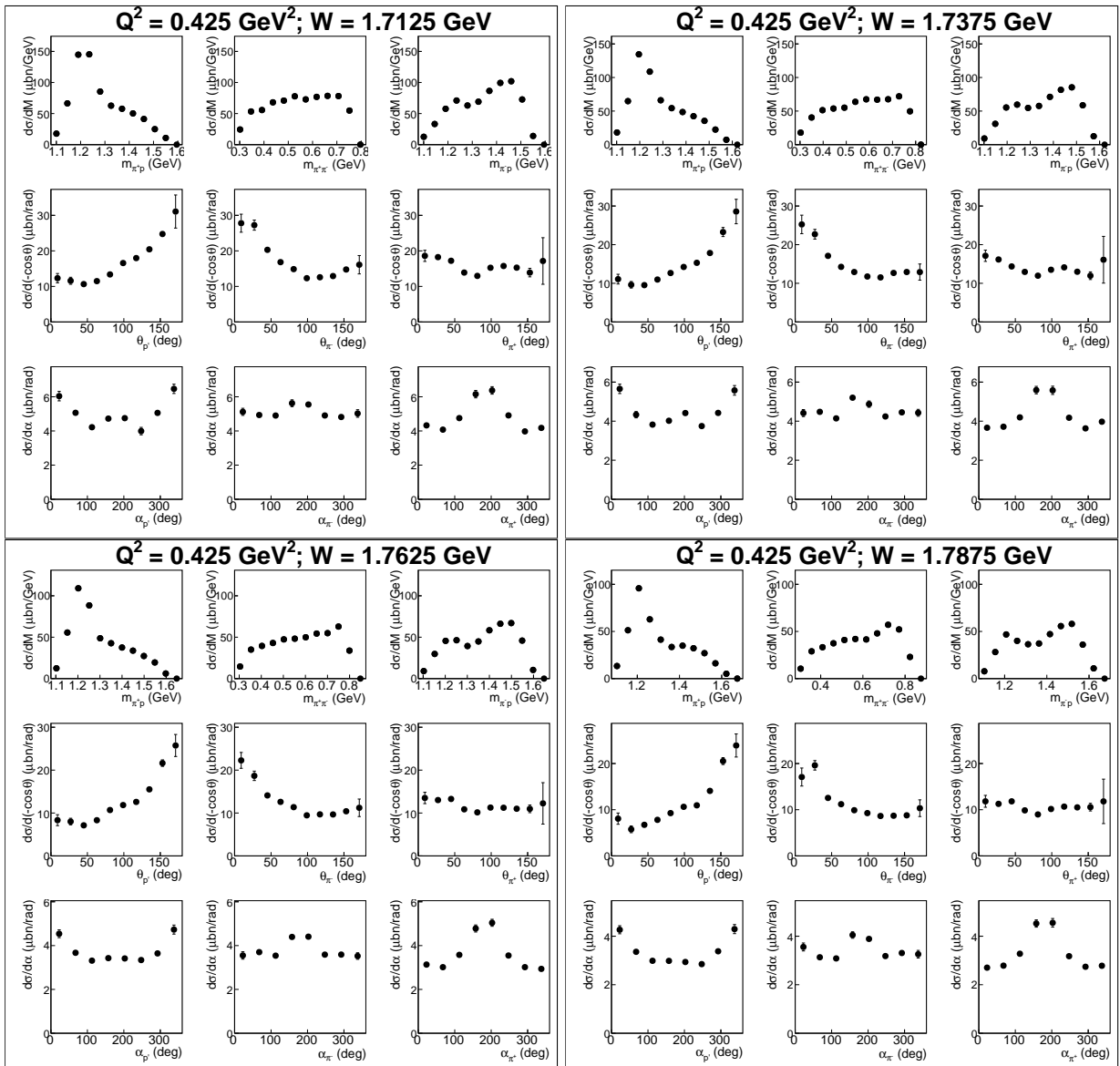


Figure A.2:

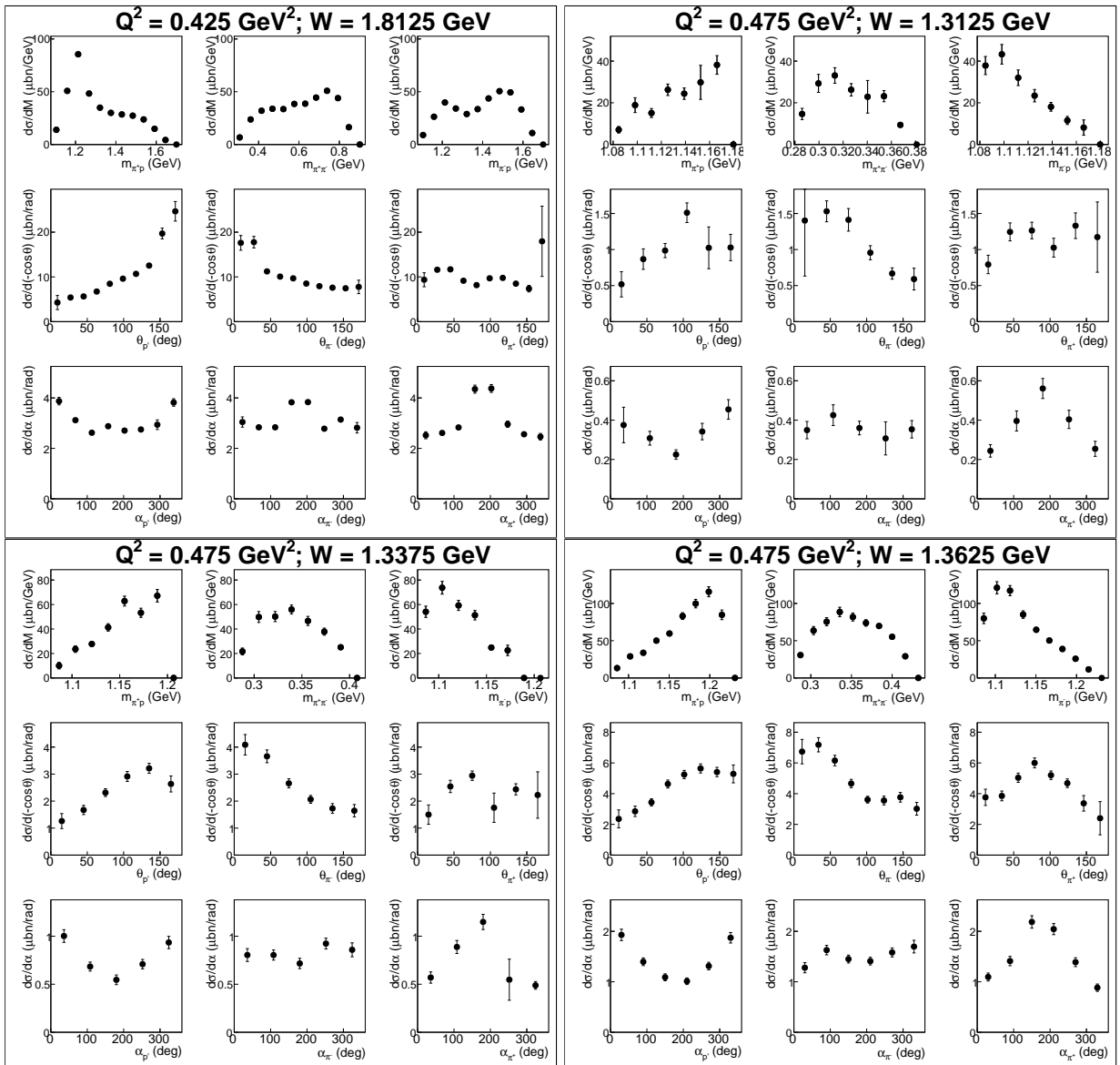


Figure A.3:

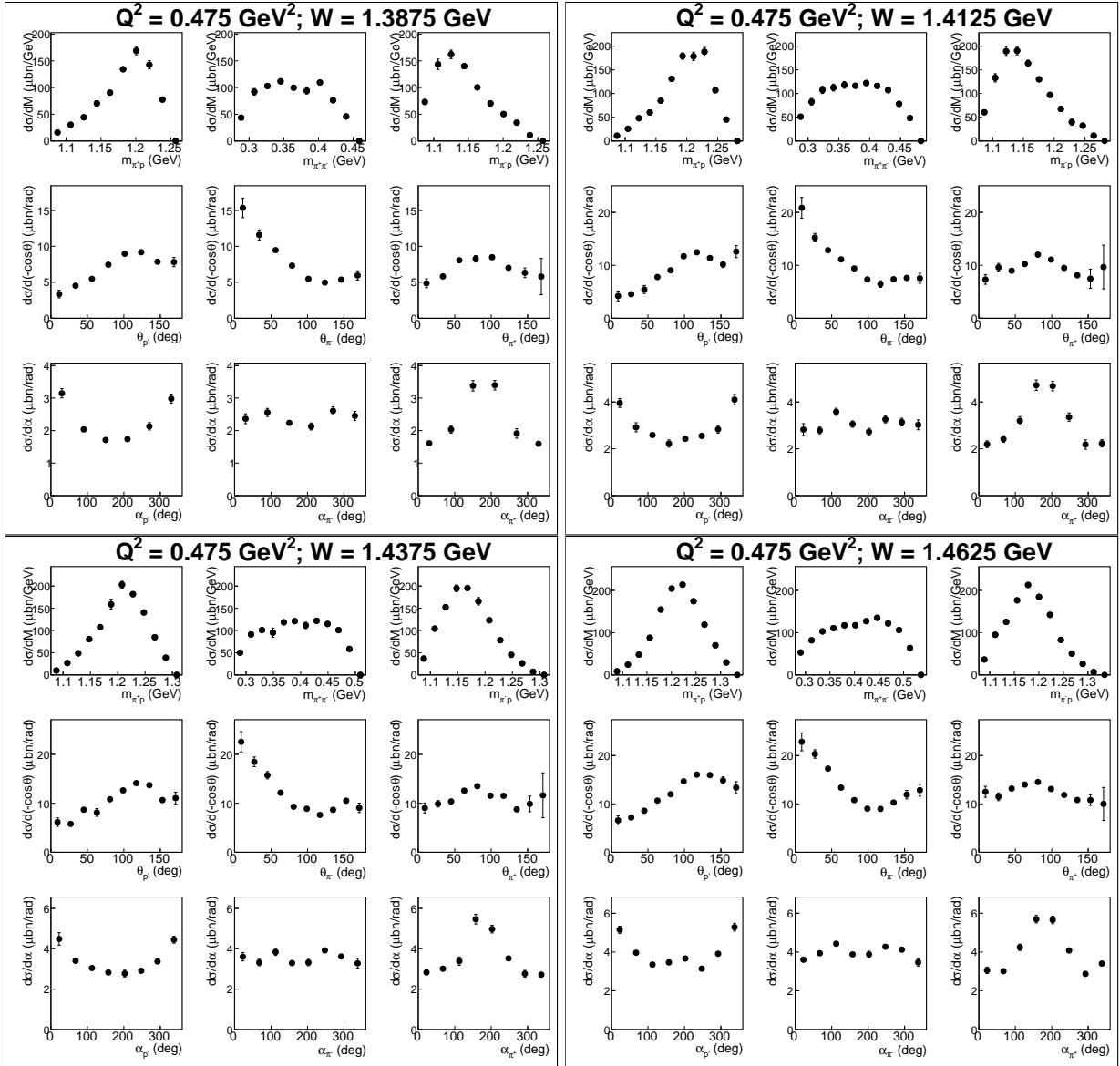


Figure A.4:

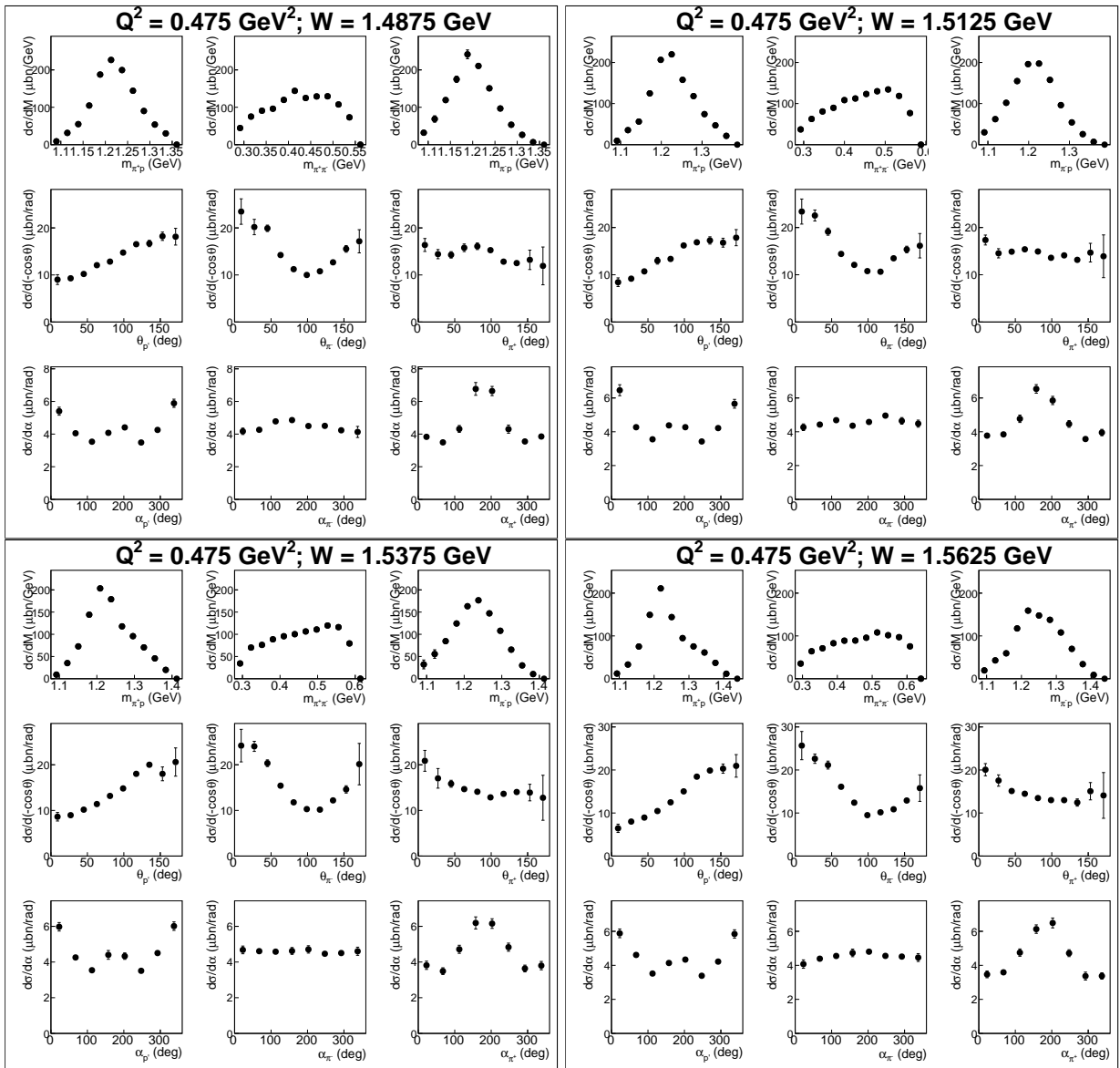


Figure A.5:

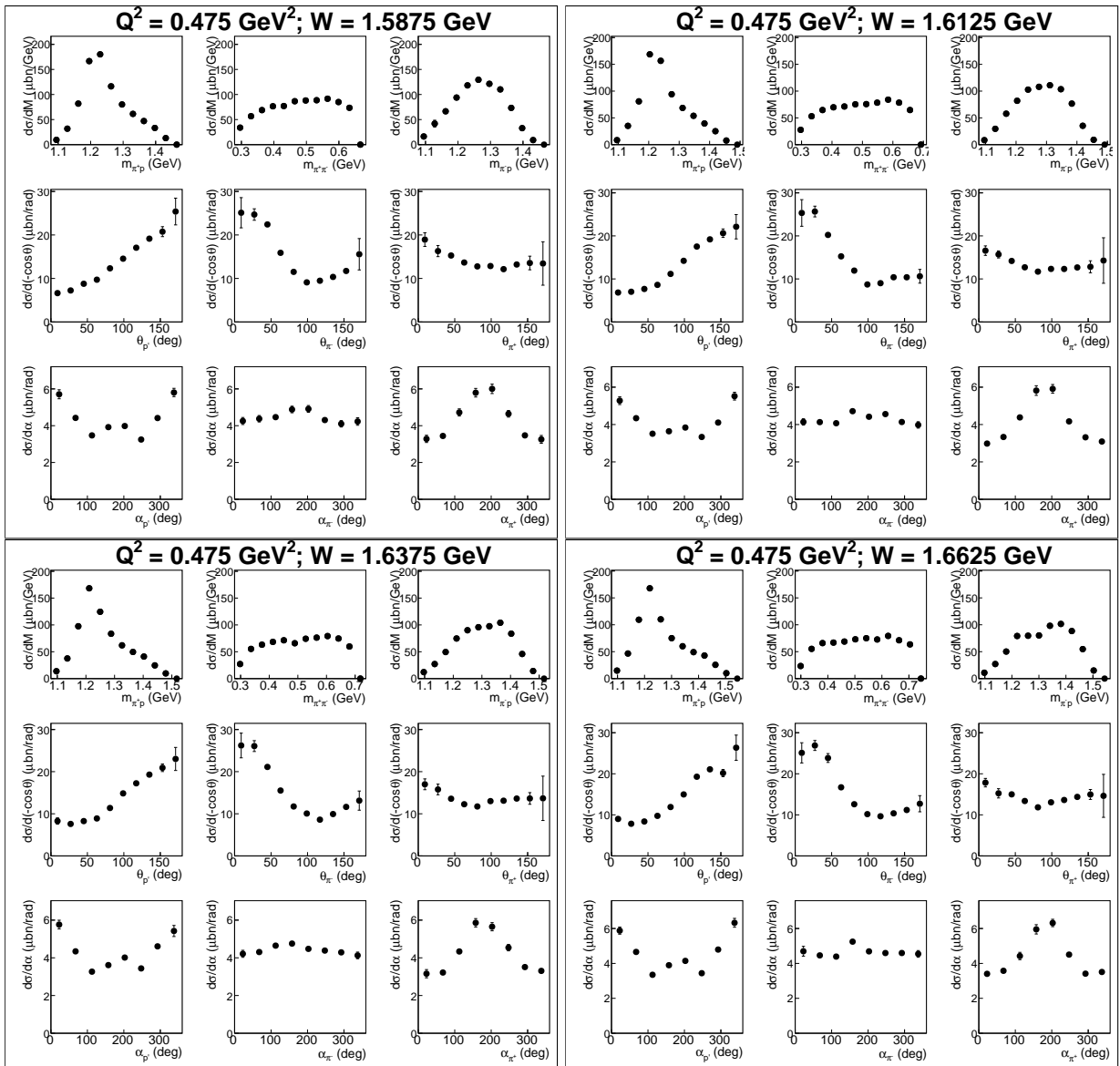


Figure A.6:

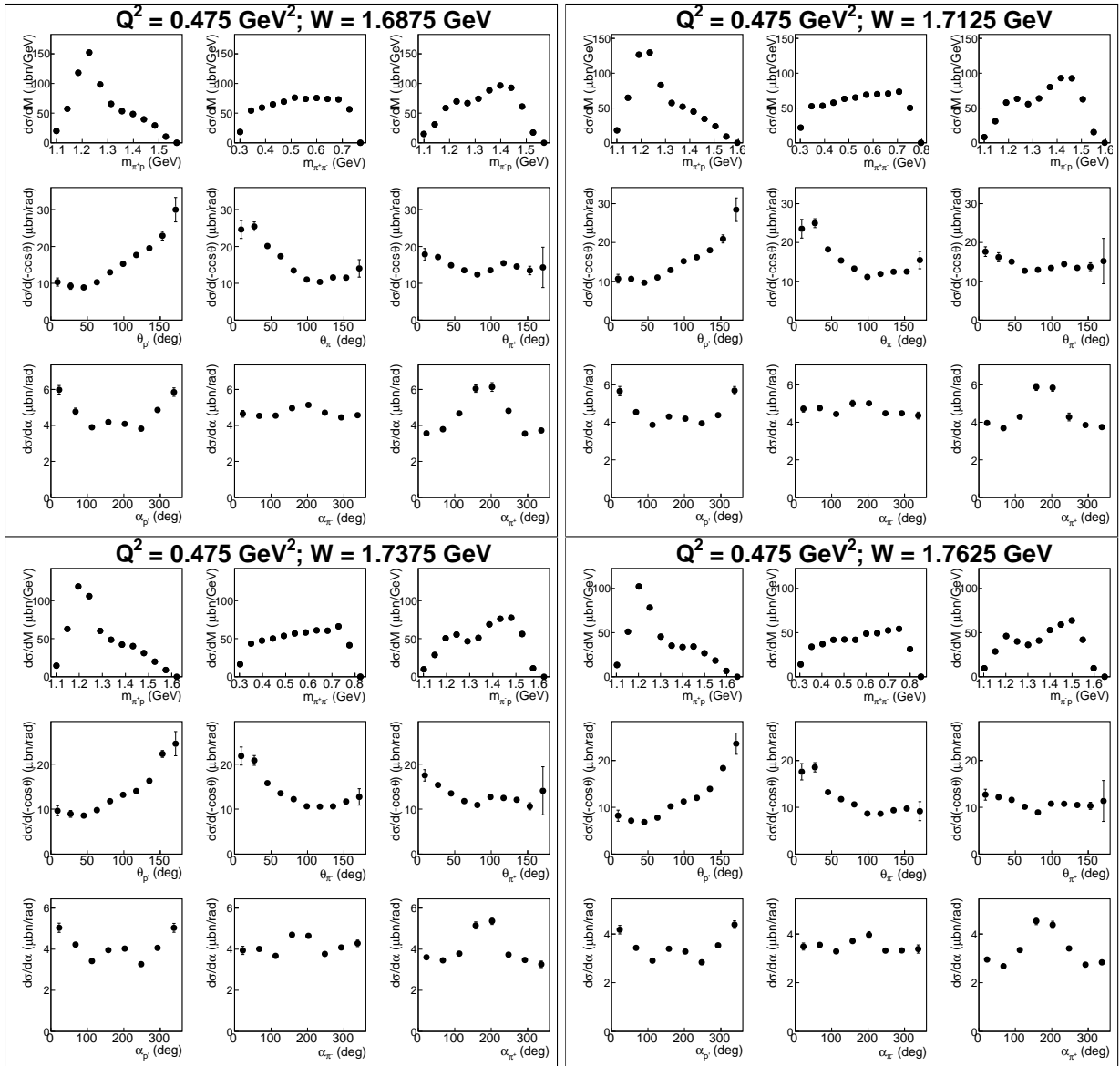


Figure A.7:

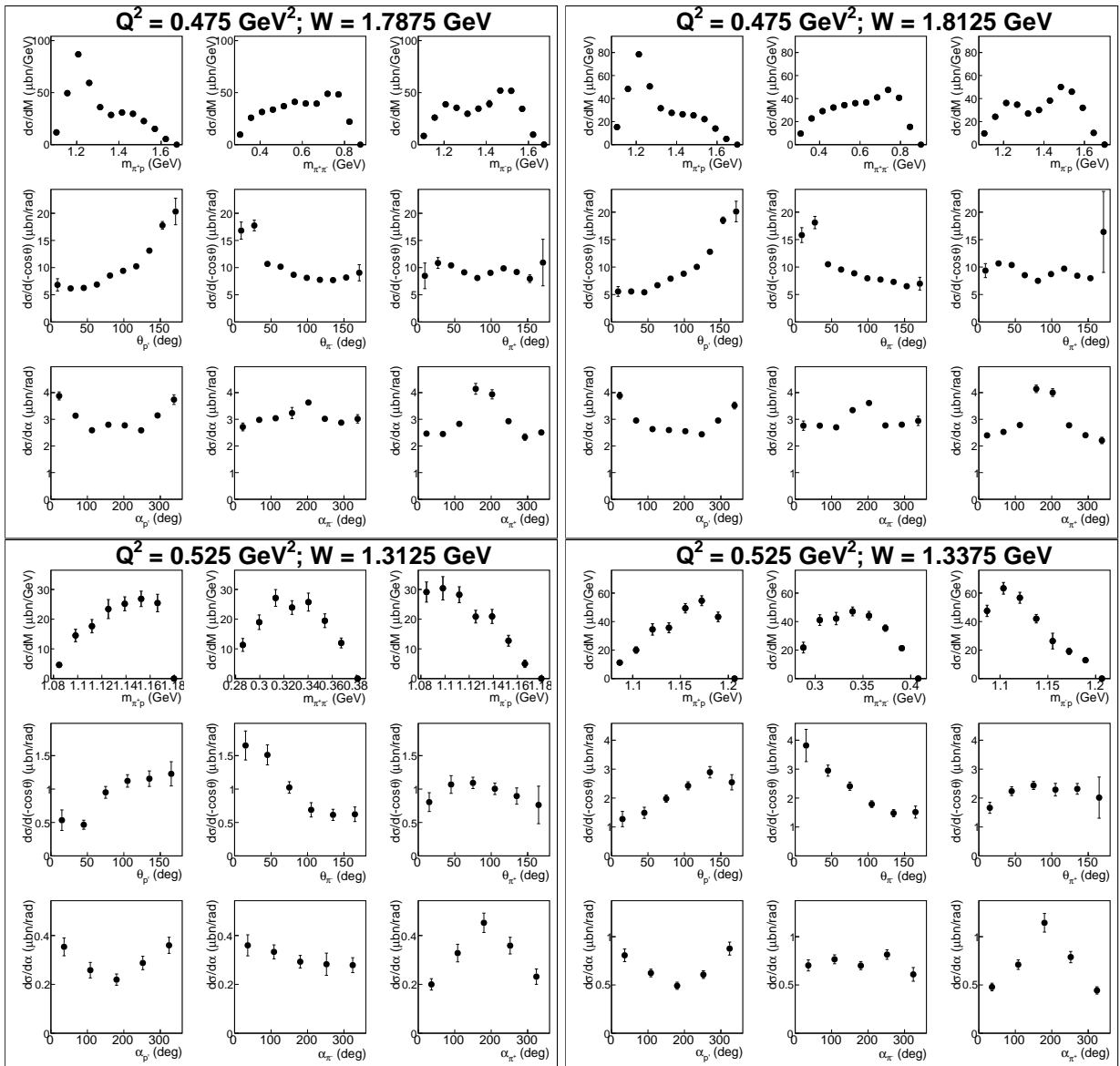


Figure A.8:

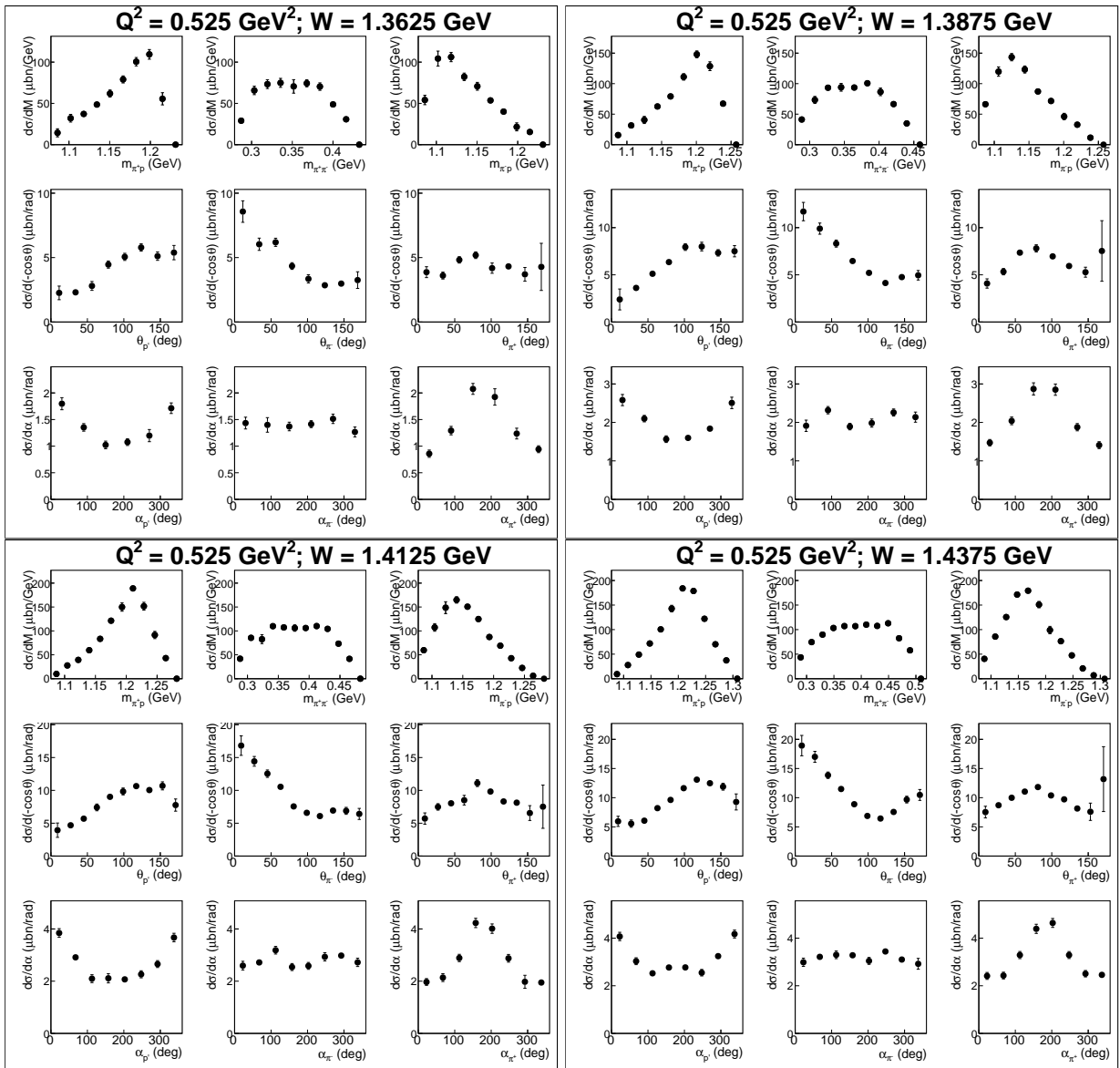


Figure A.9:

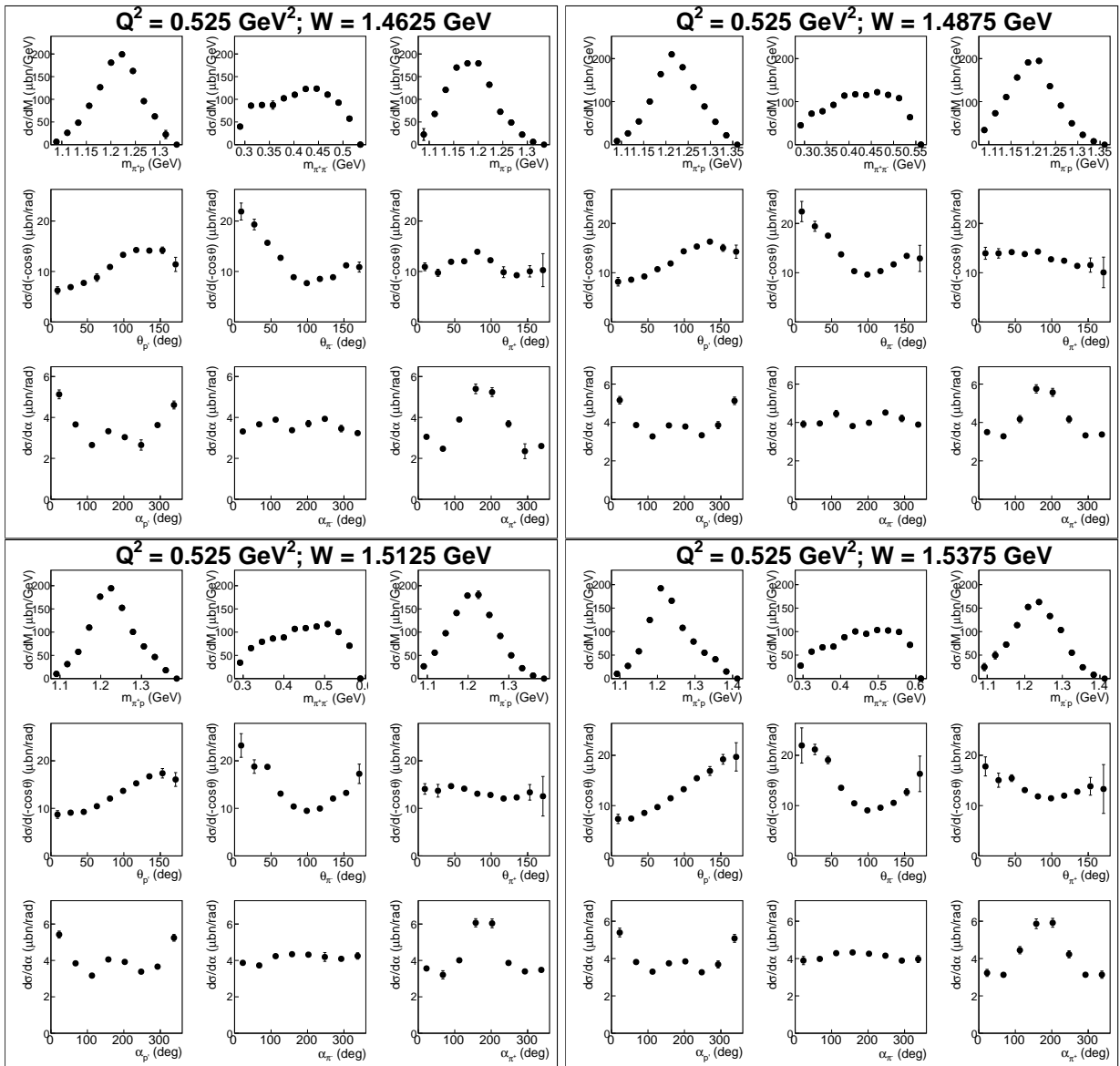


Figure A.10:

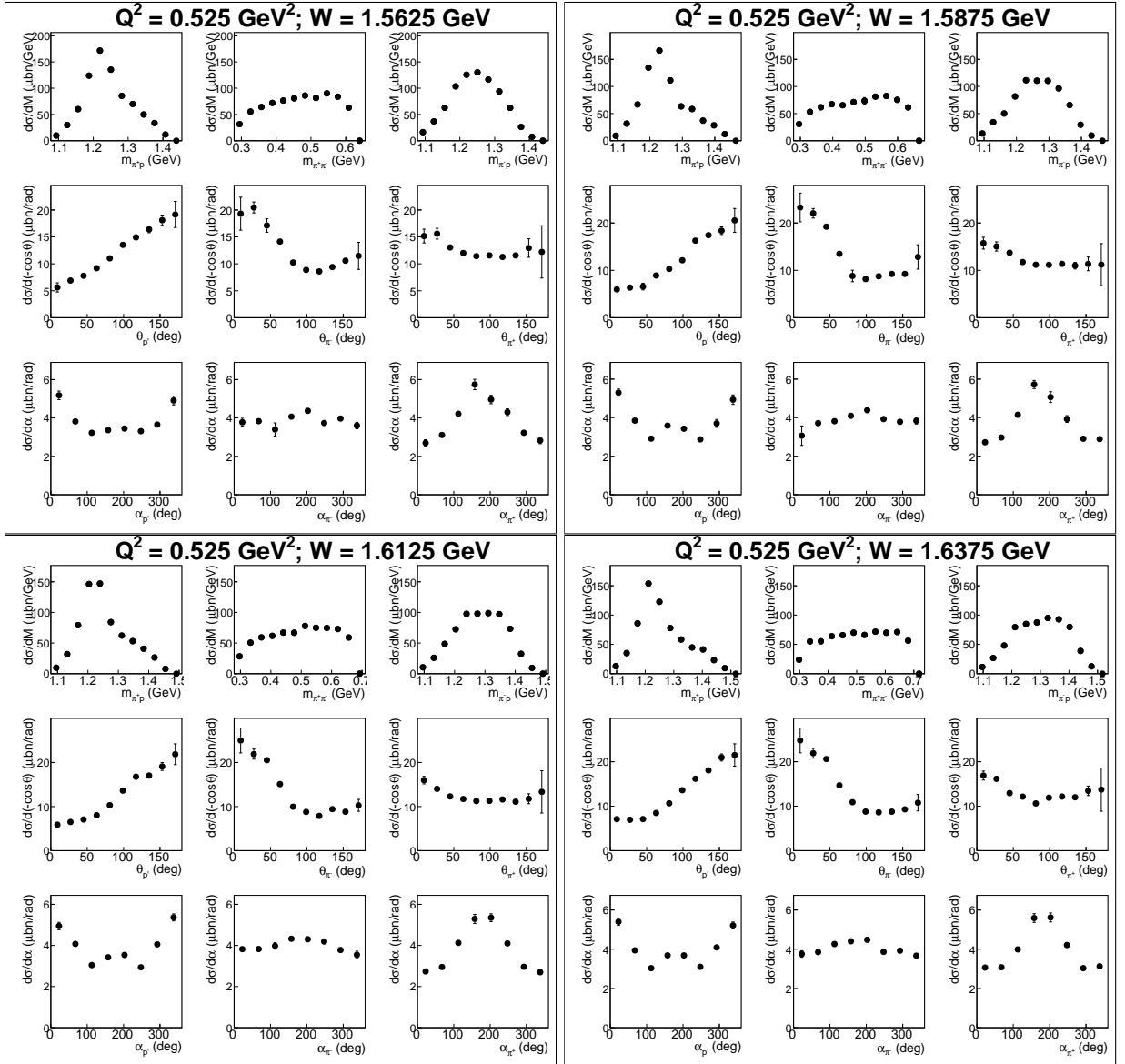


Figure A.11:

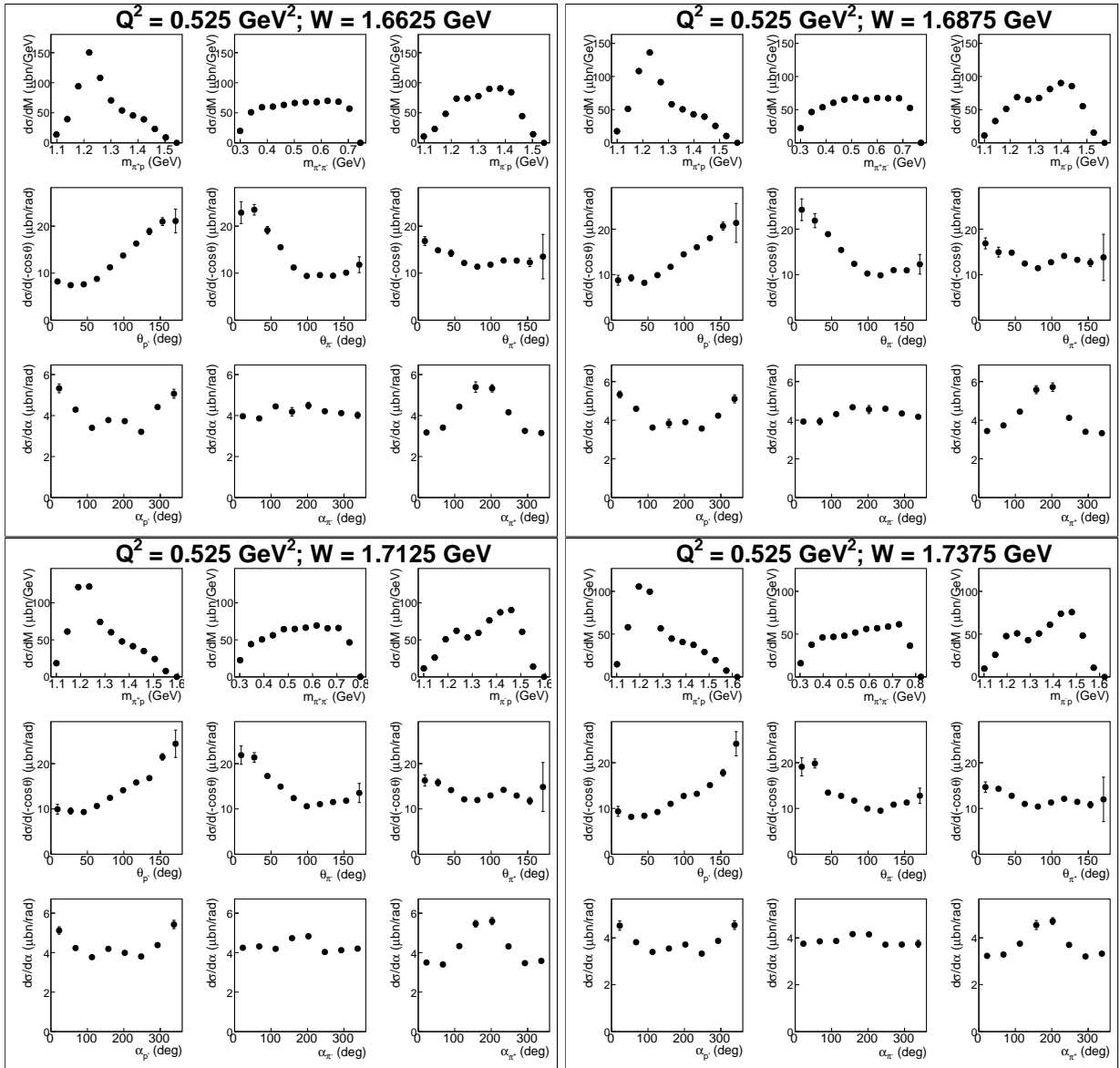


Figure A.12:

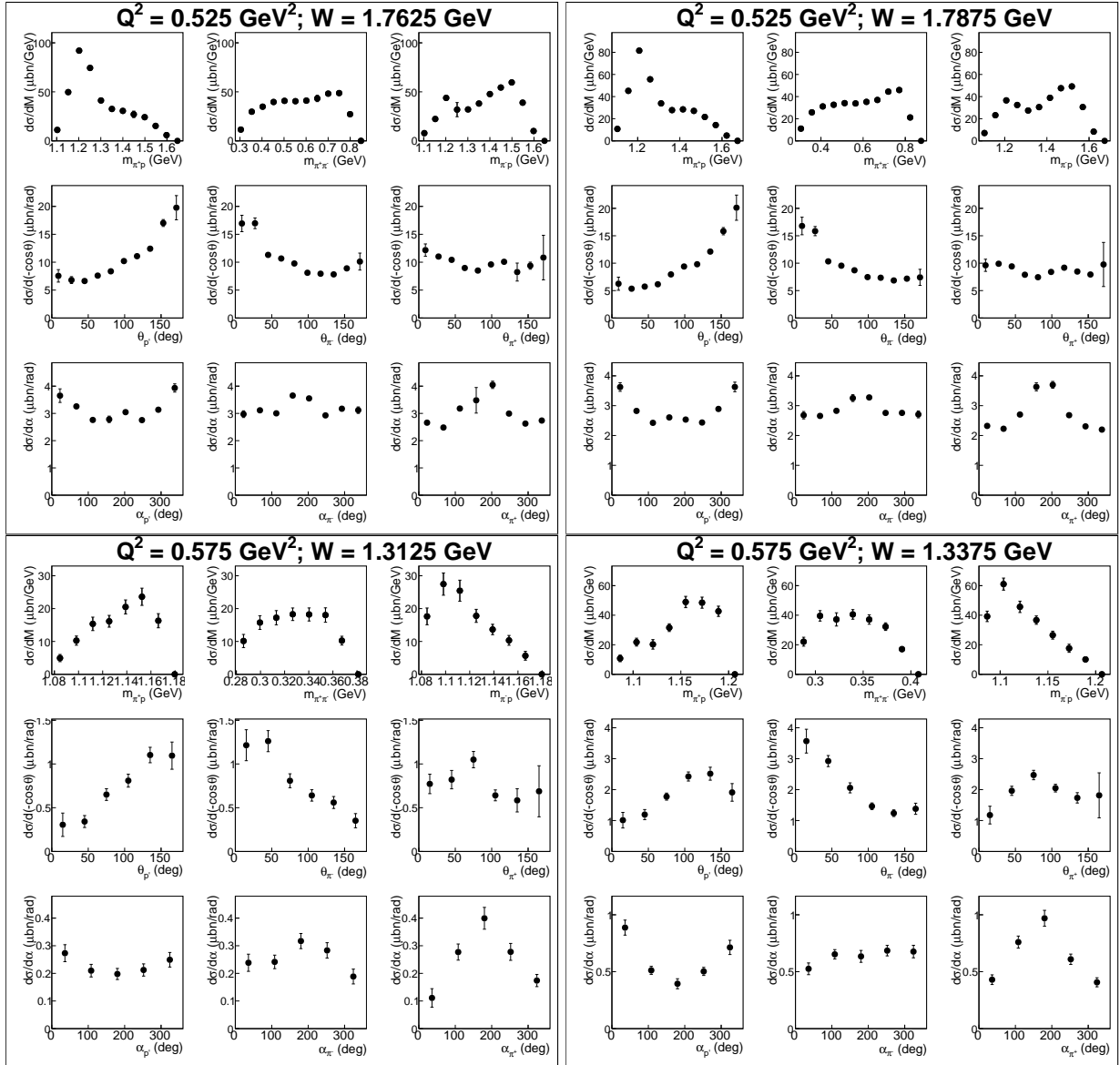


Figure A.13:

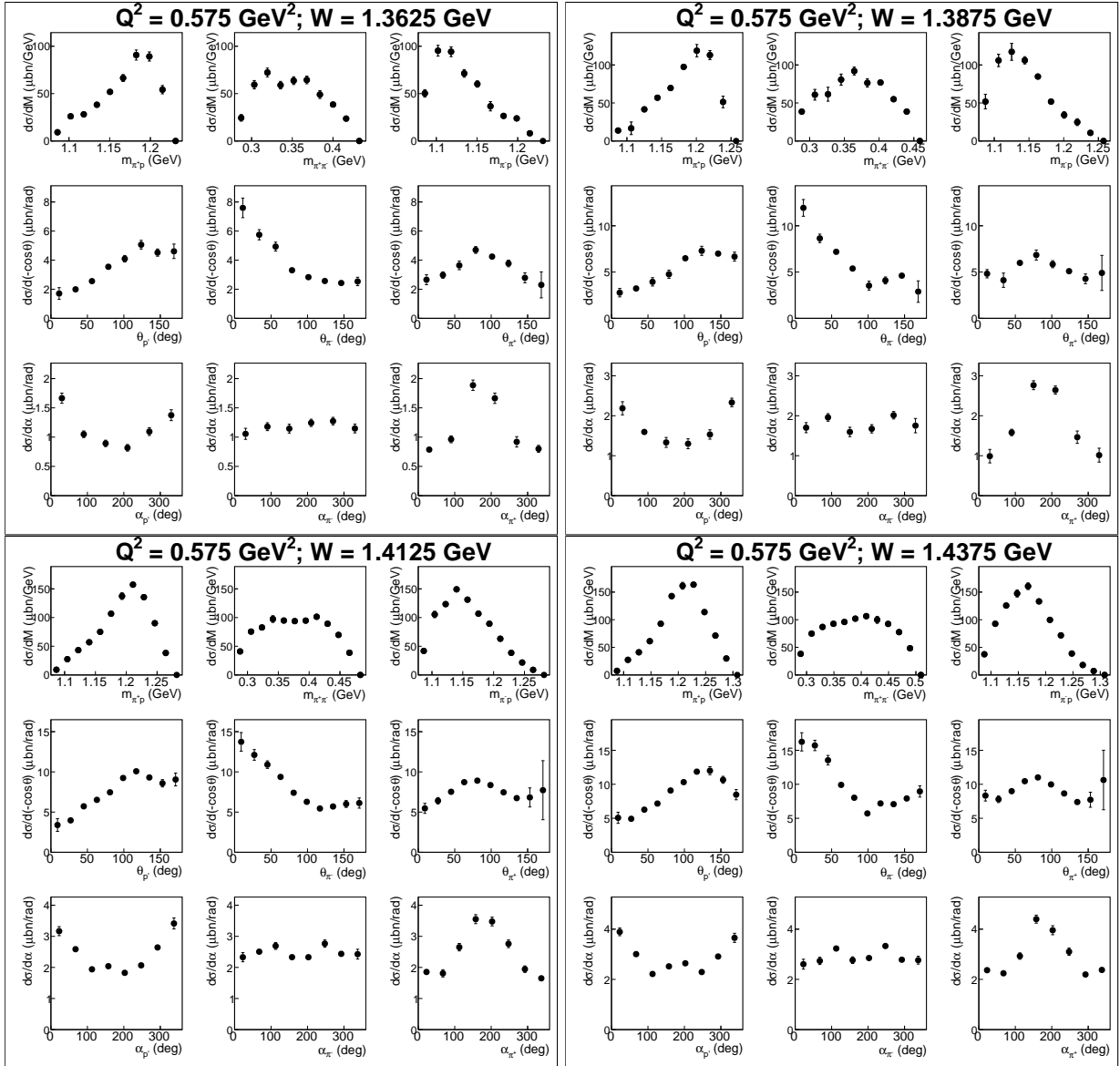


Figure A.14:

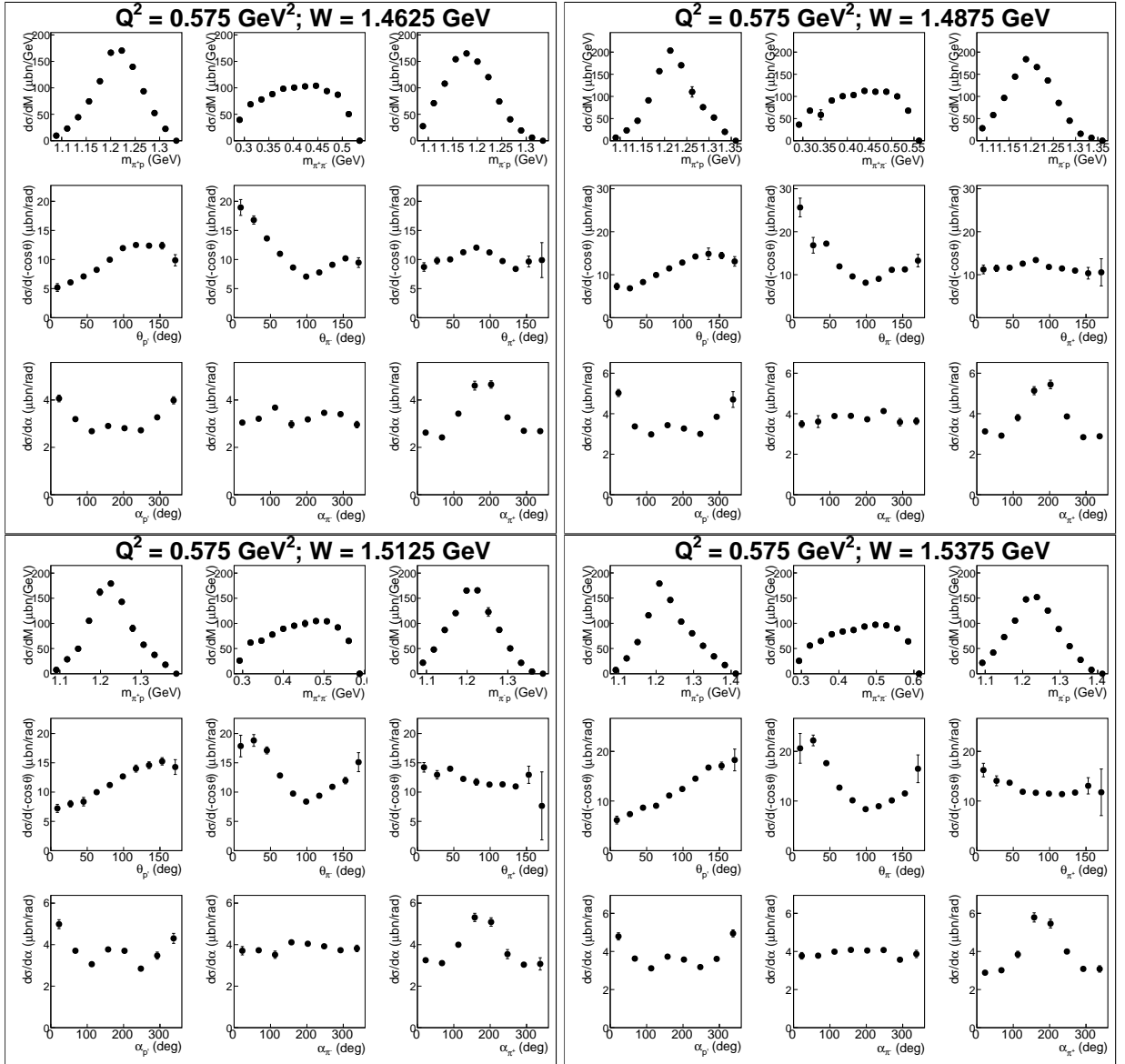


Figure A.15:

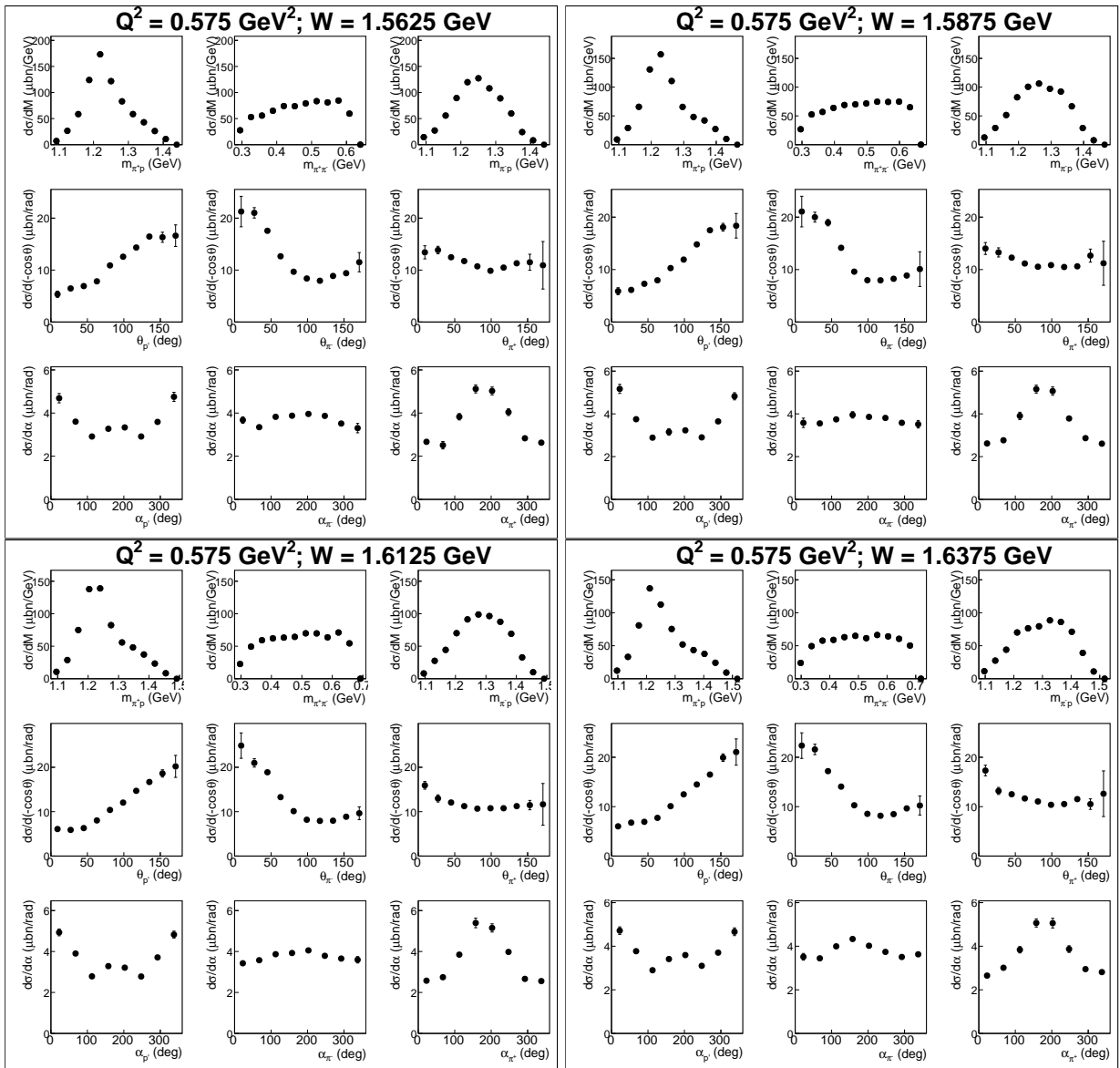


Figure A.16:

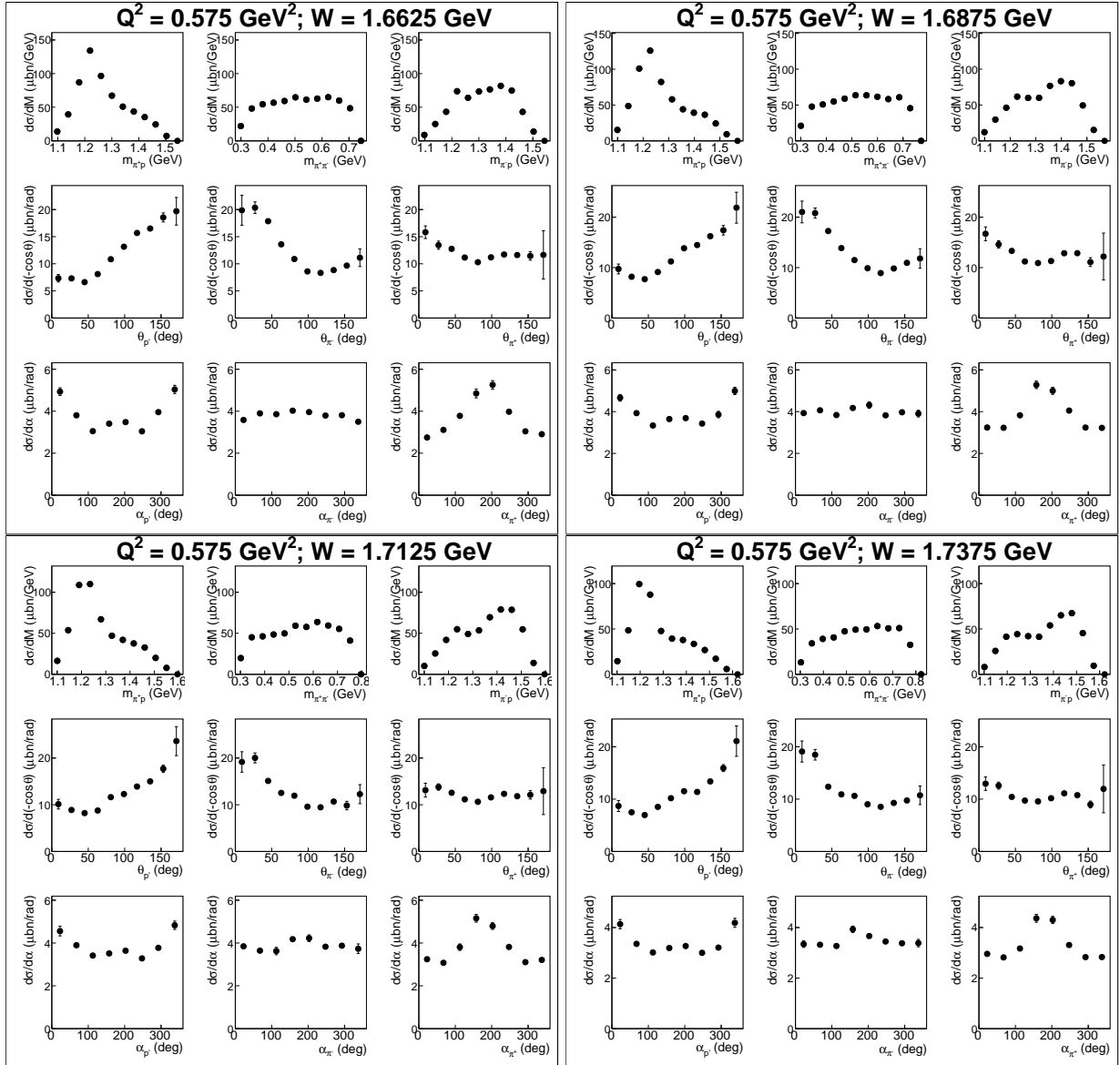


Figure A.17:

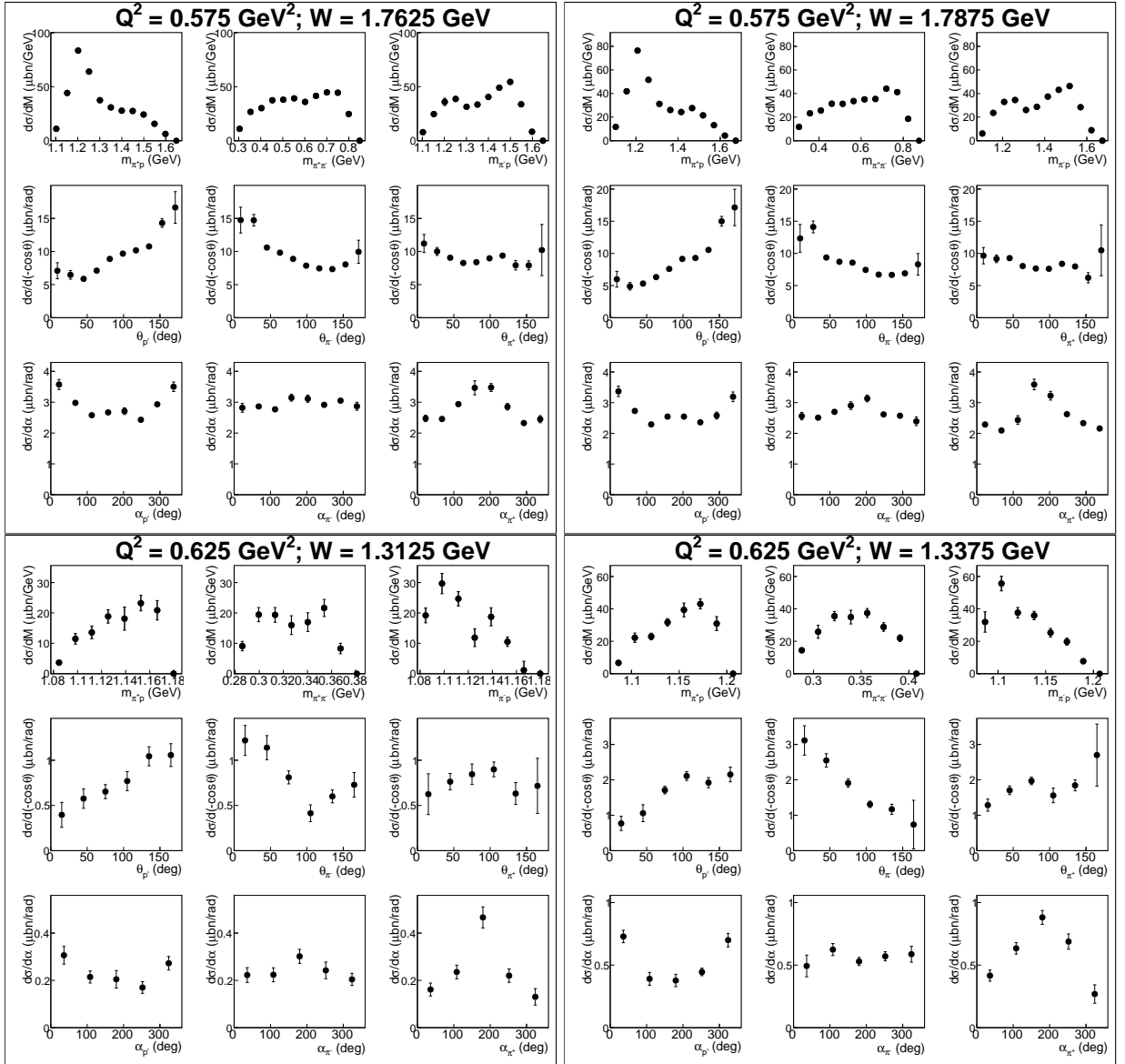


Figure A.18:

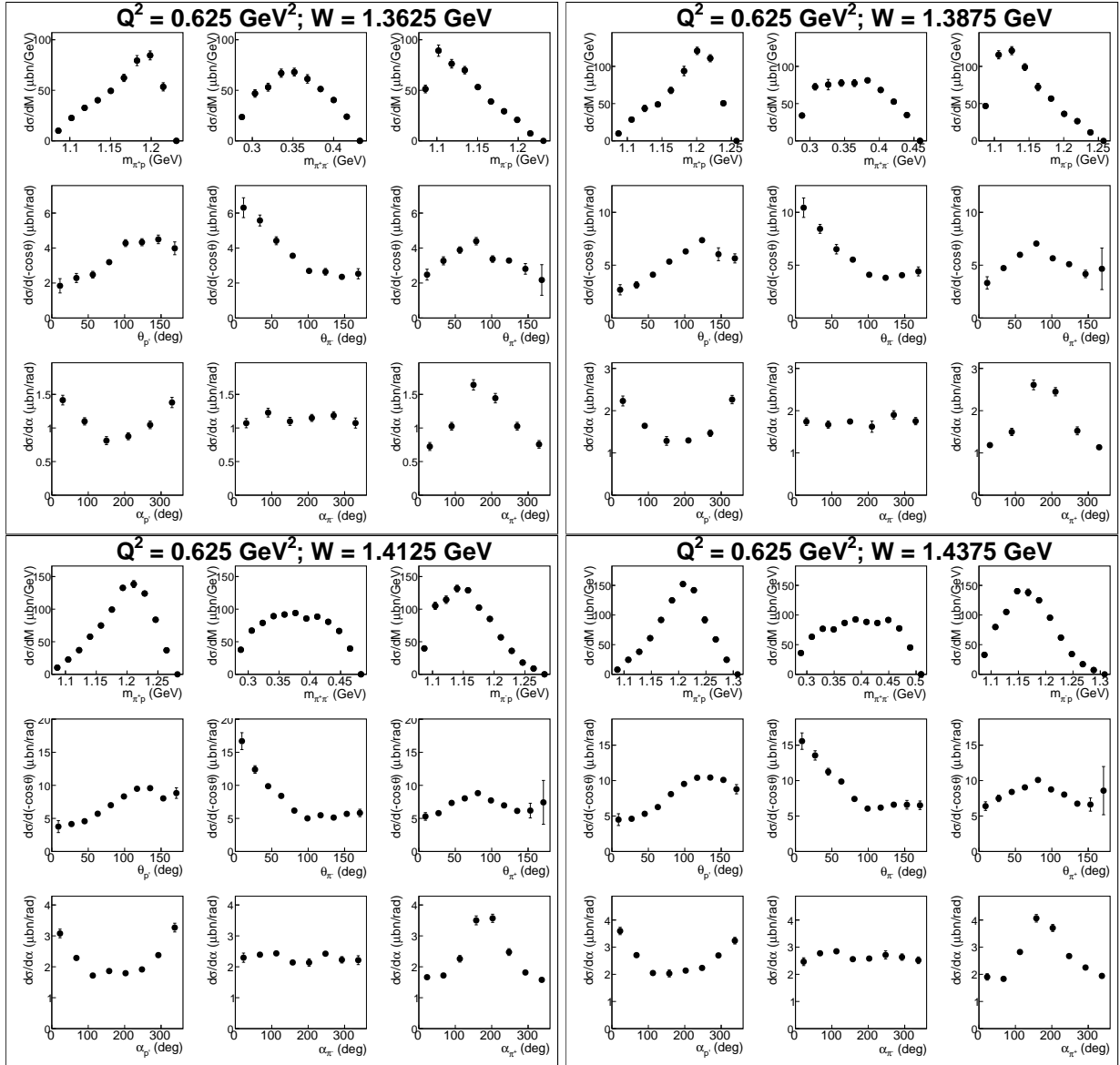


Figure A.19:

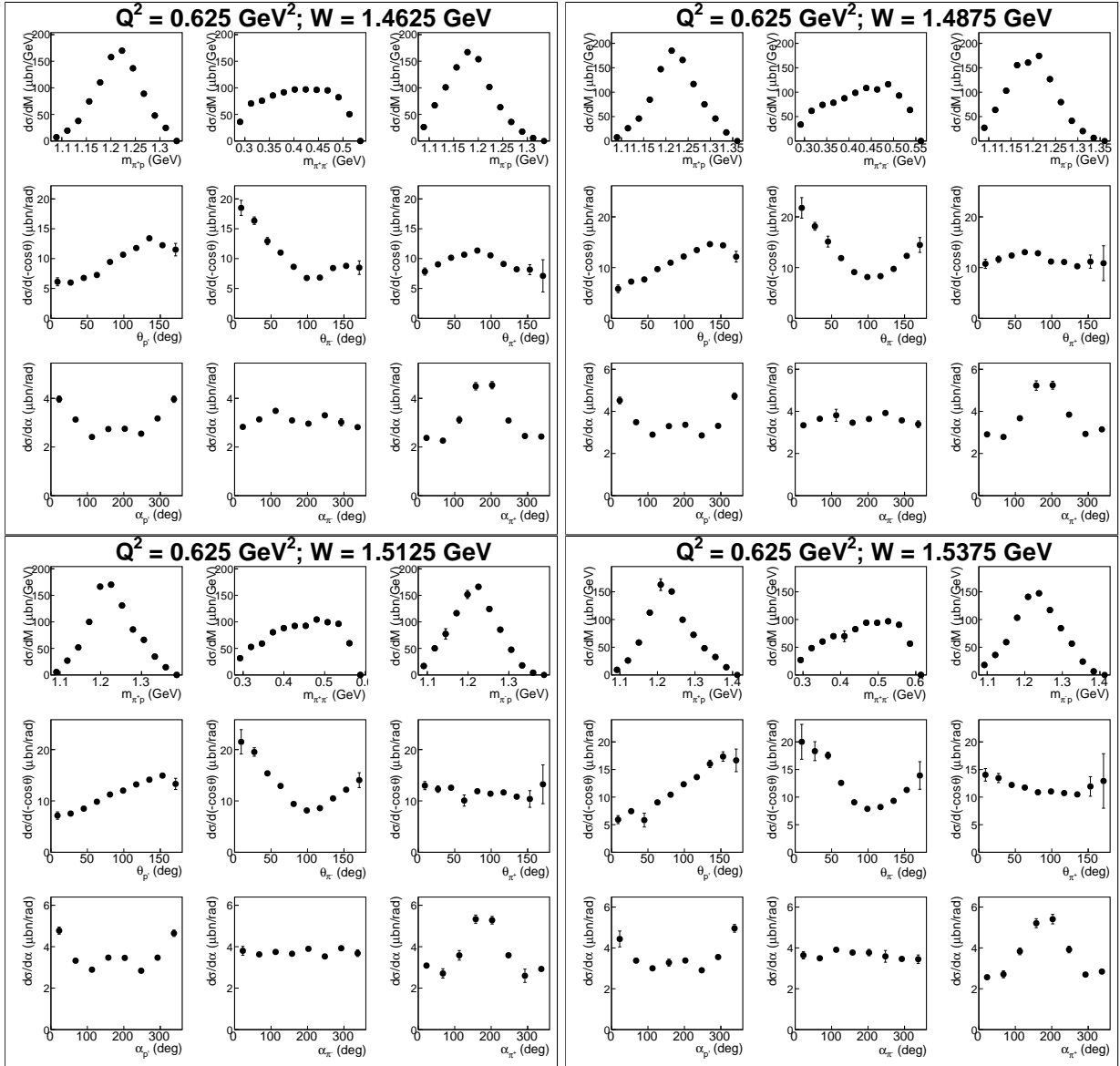


Figure A.20:

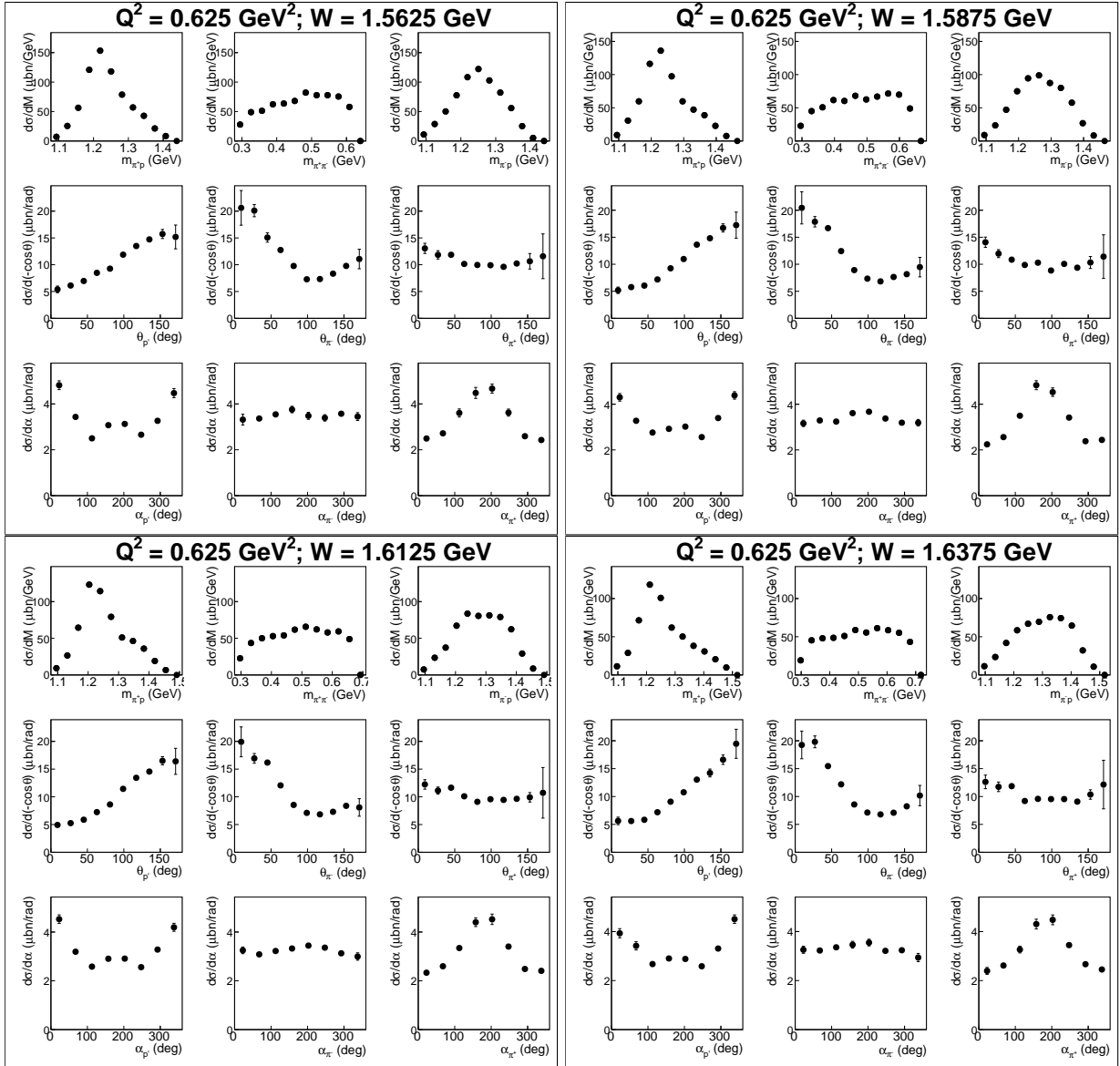


Figure A.21:

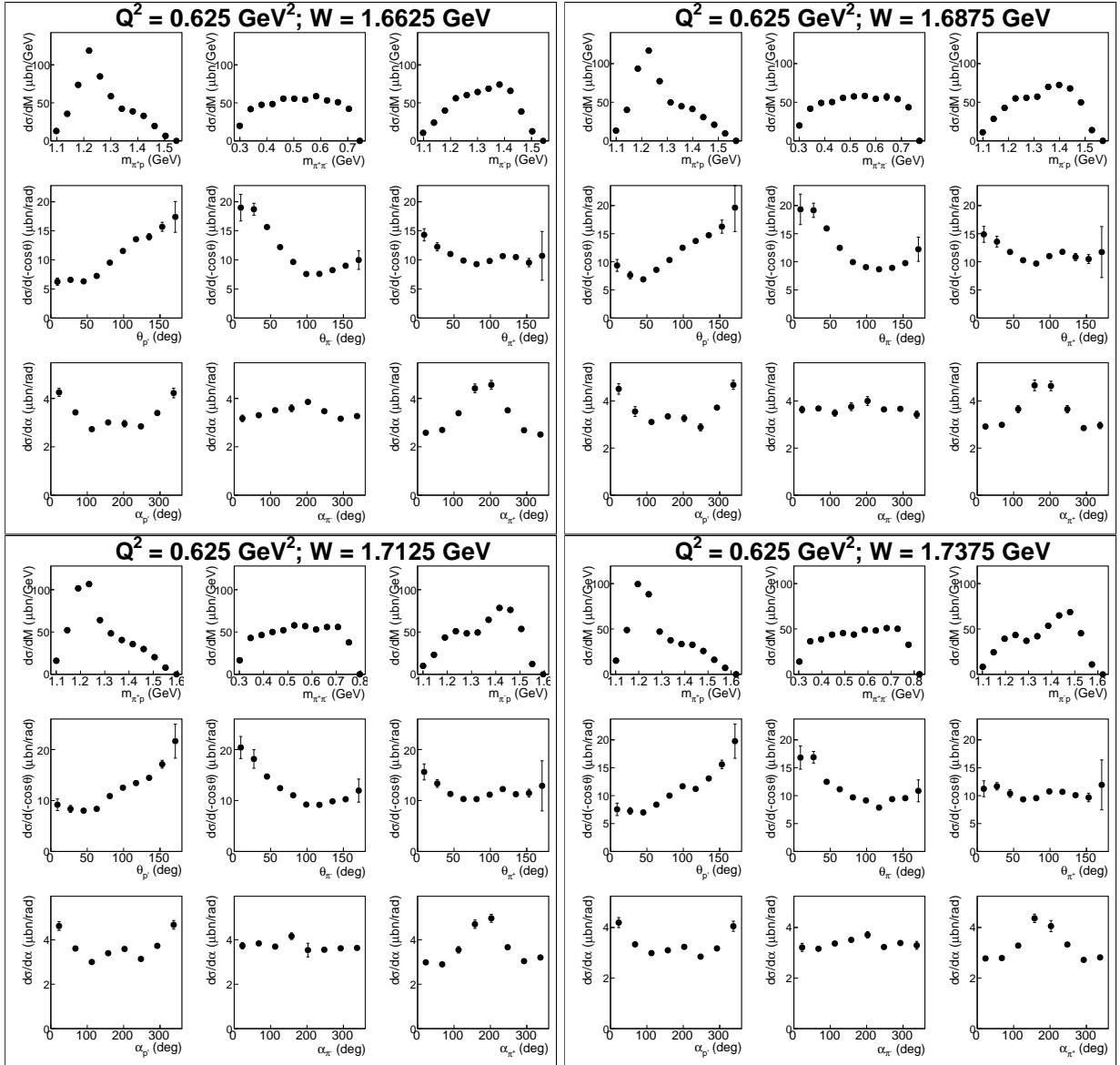


Figure A.22:

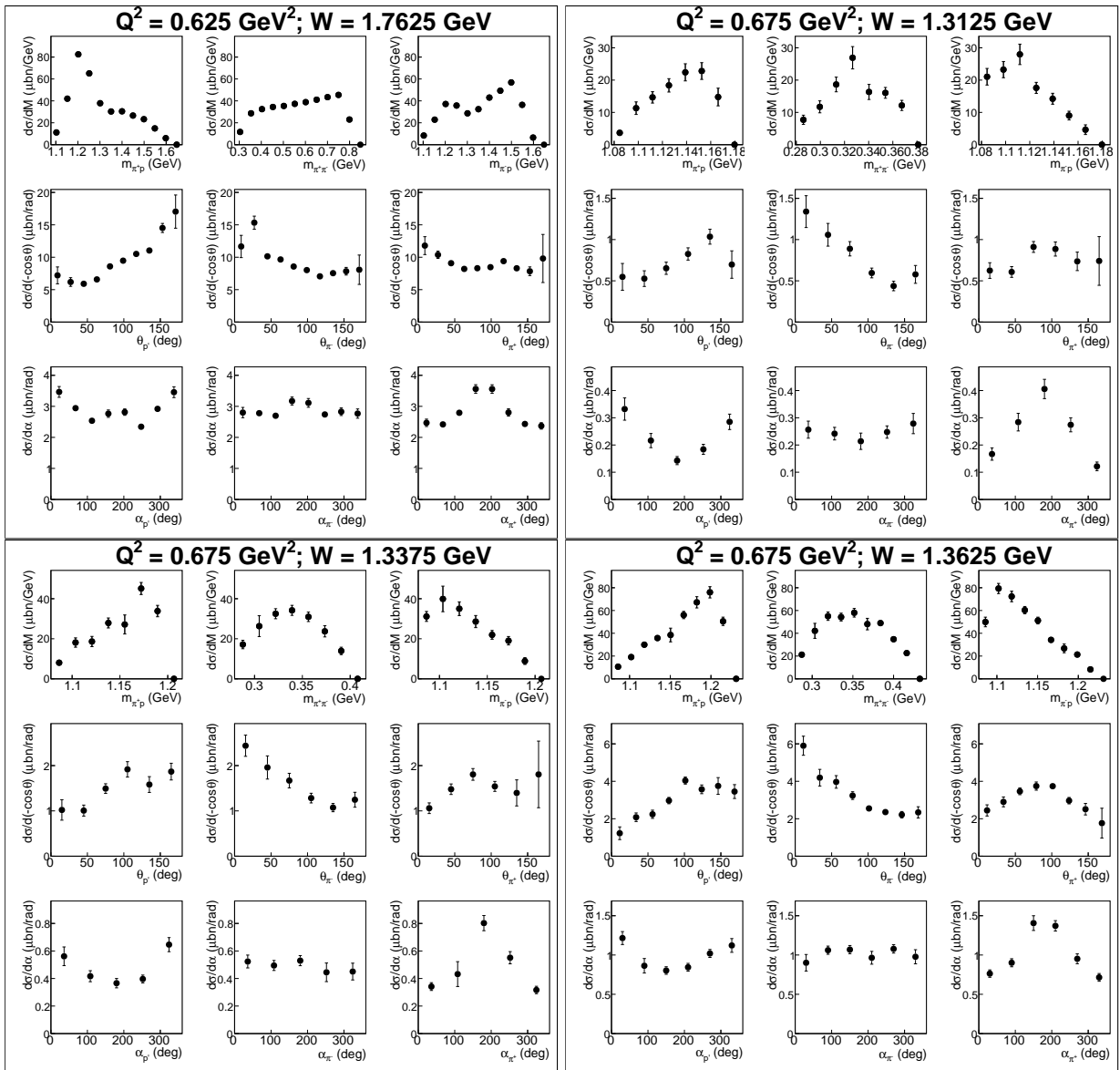


Figure A.23:

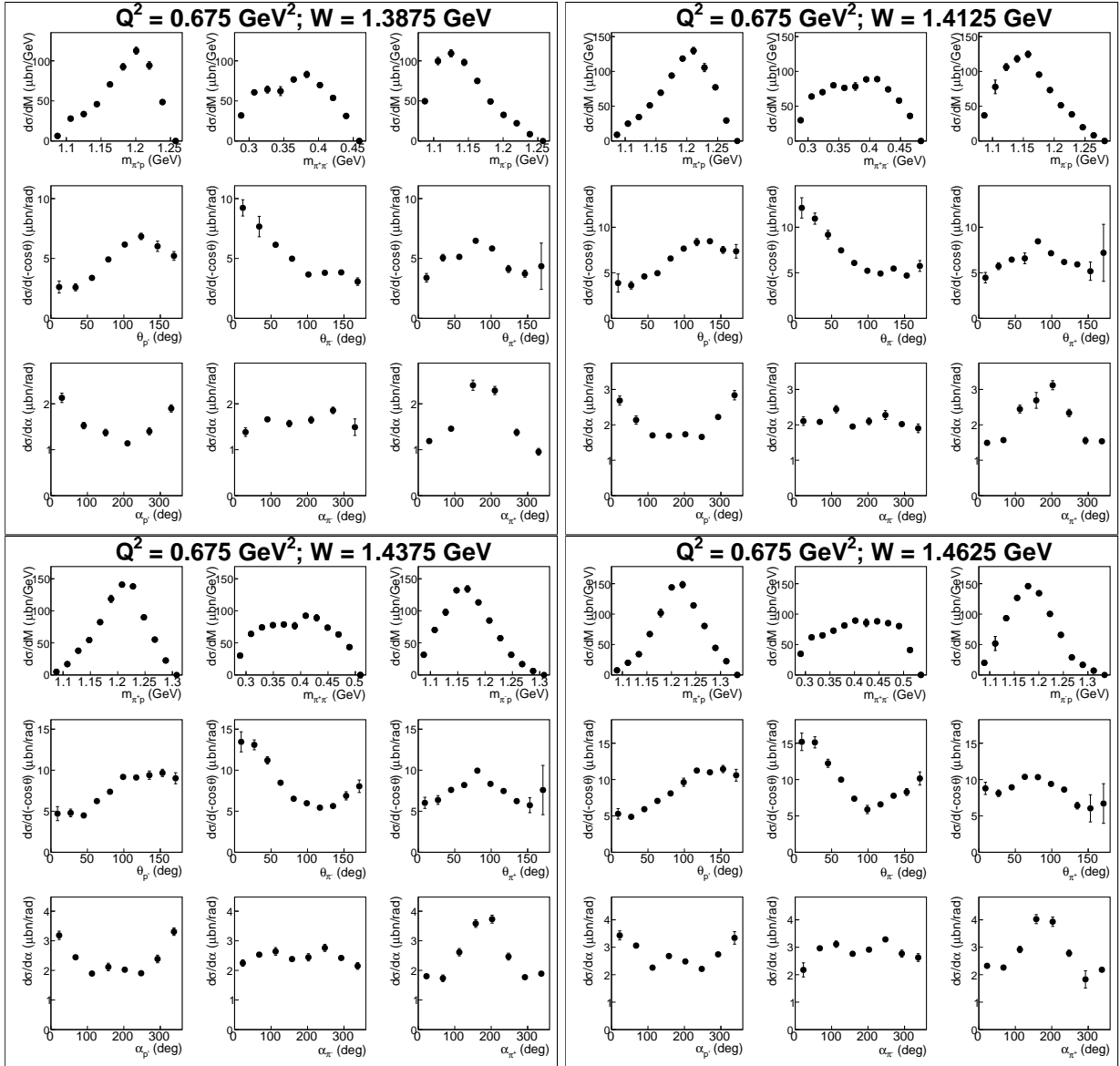


Figure A.24:

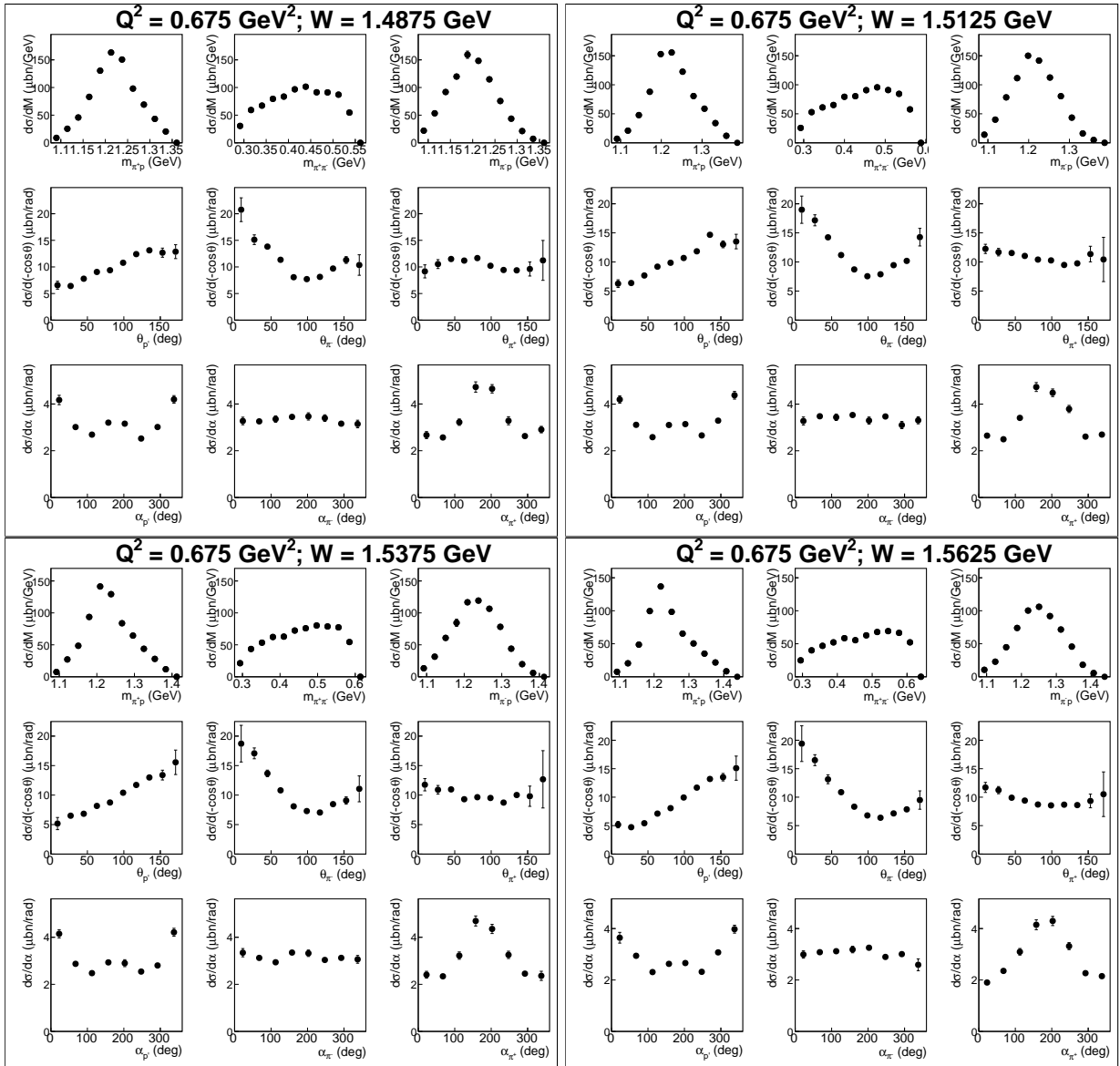


Figure A.25:

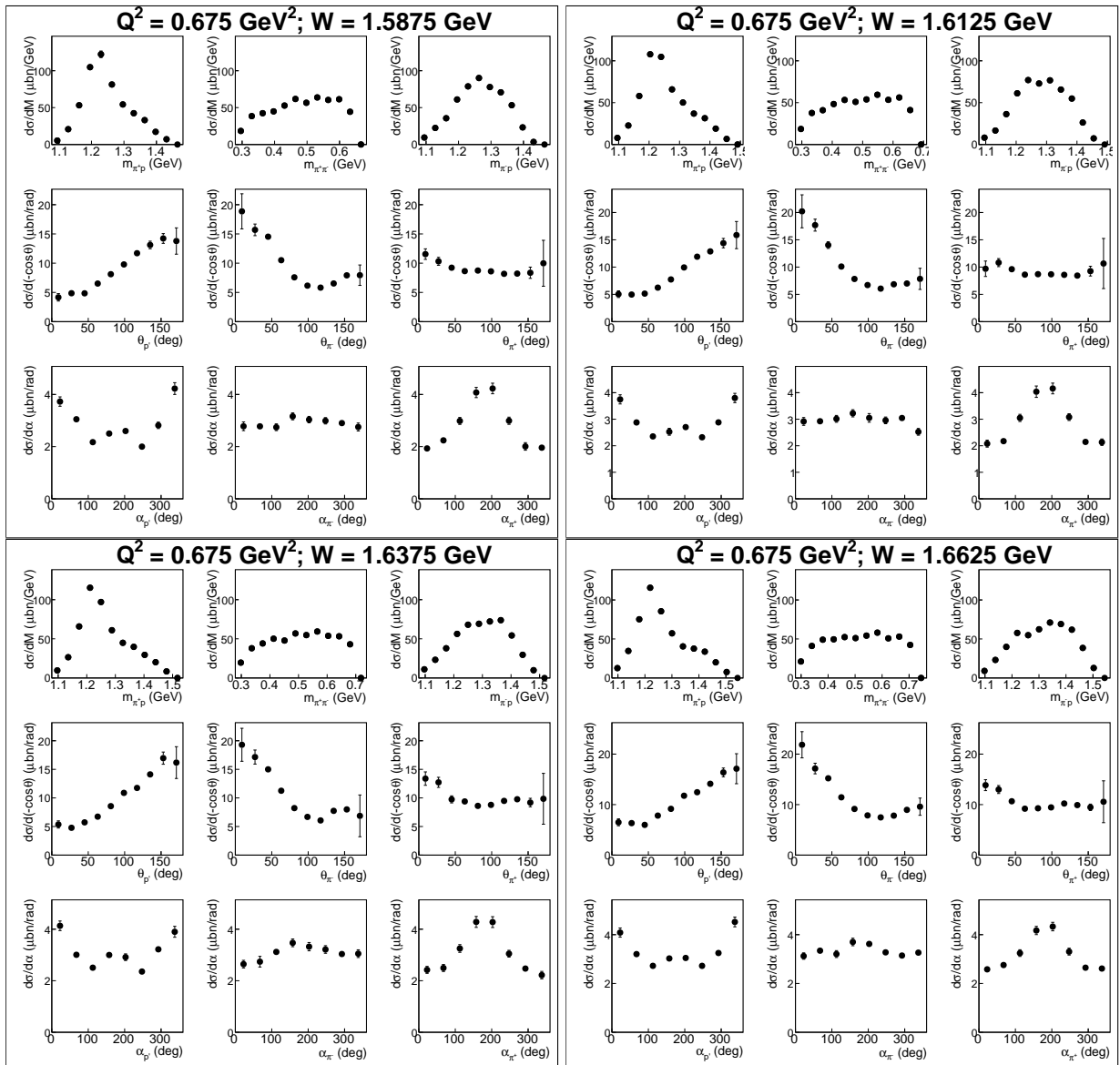


Figure A.26:

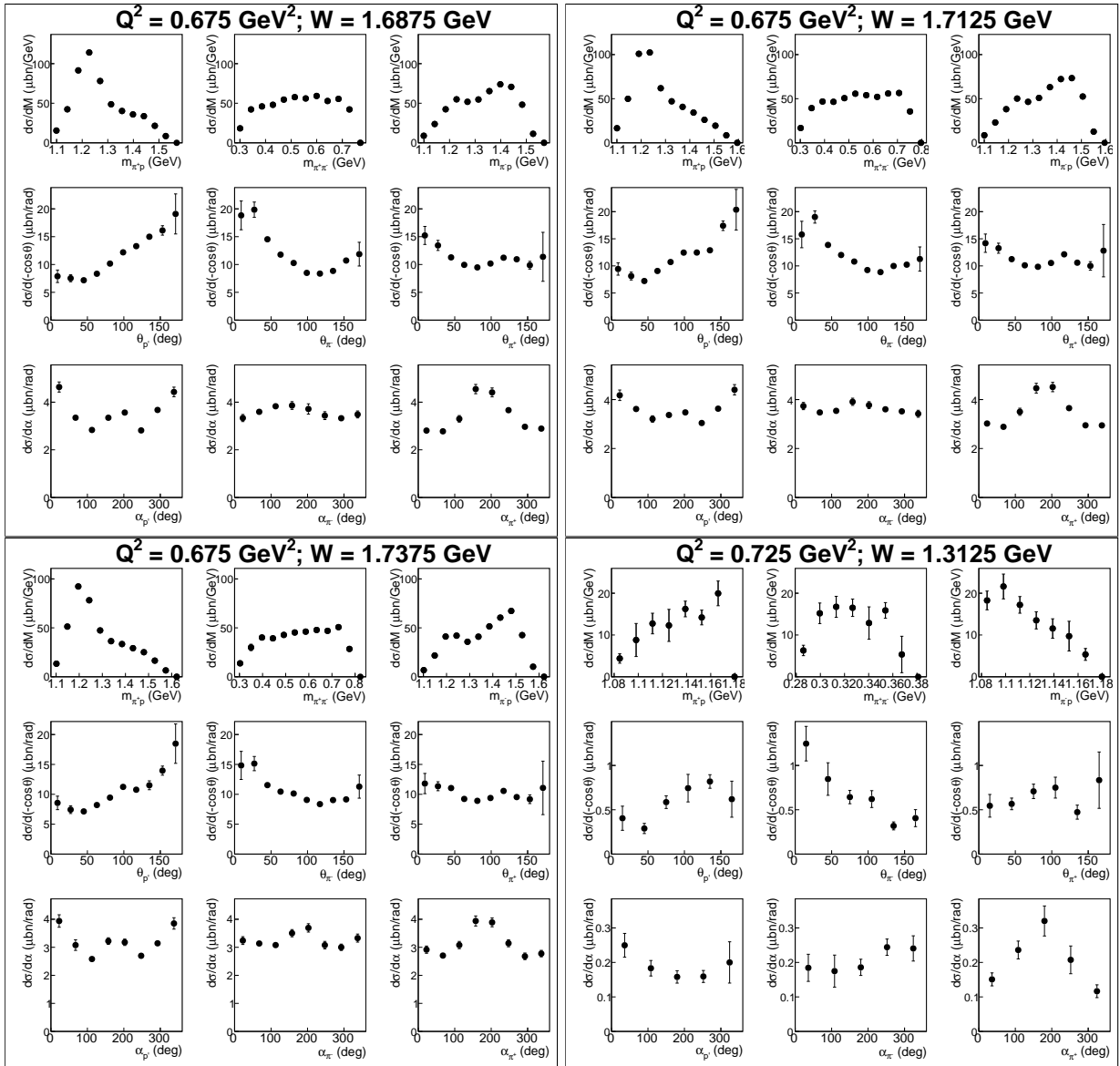


Figure A.27:

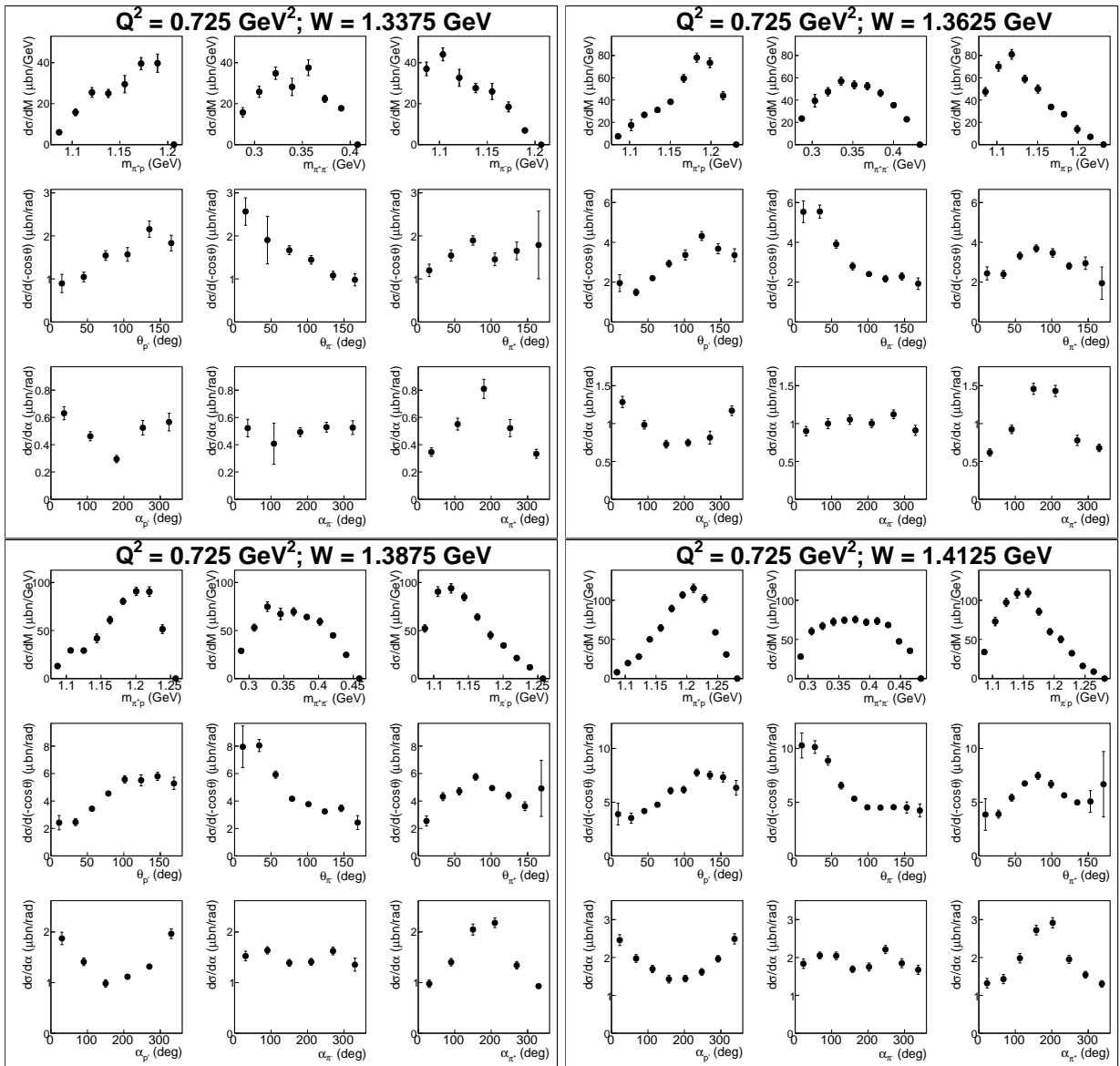


Figure A.28:

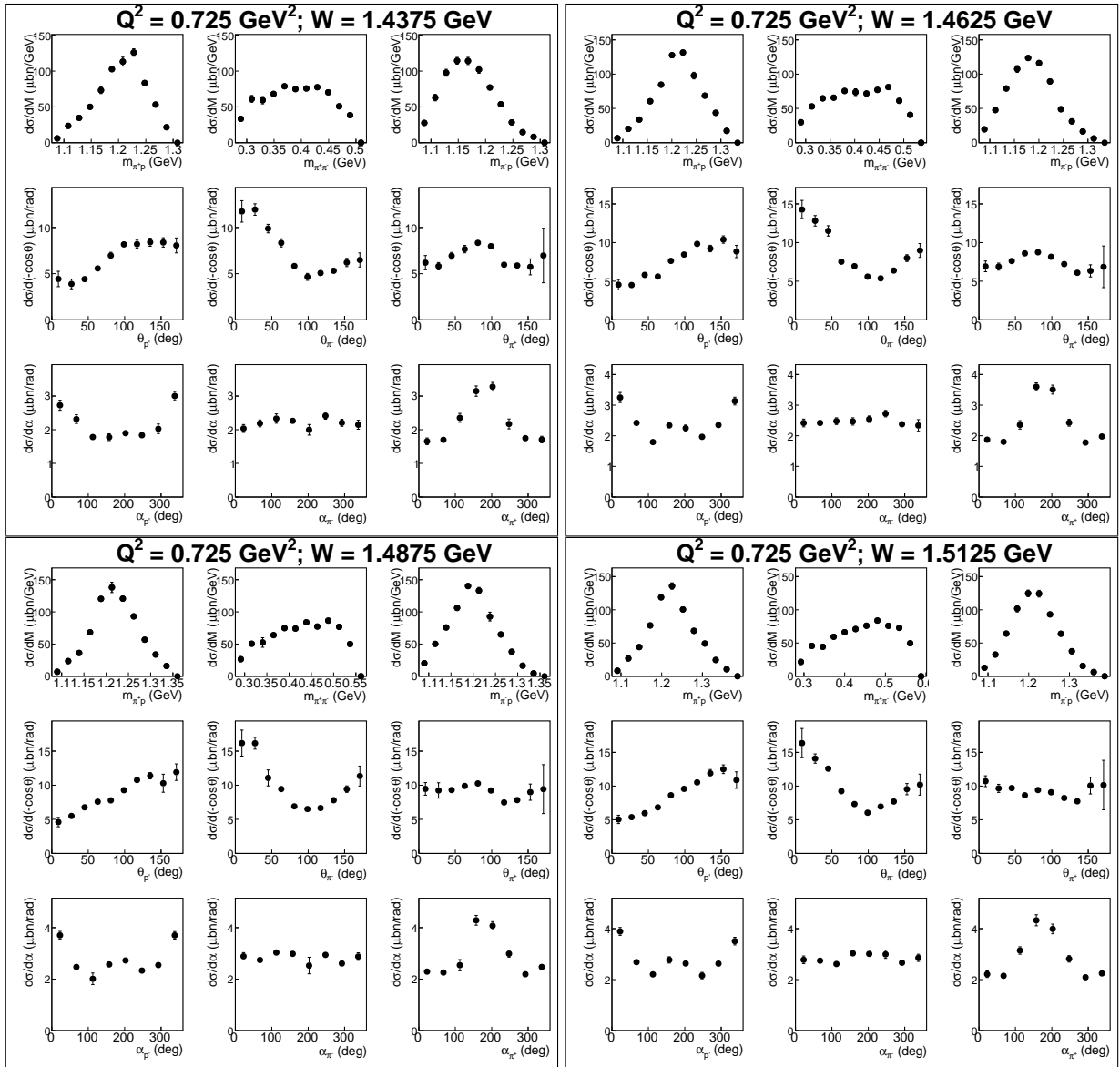


Figure A.29:

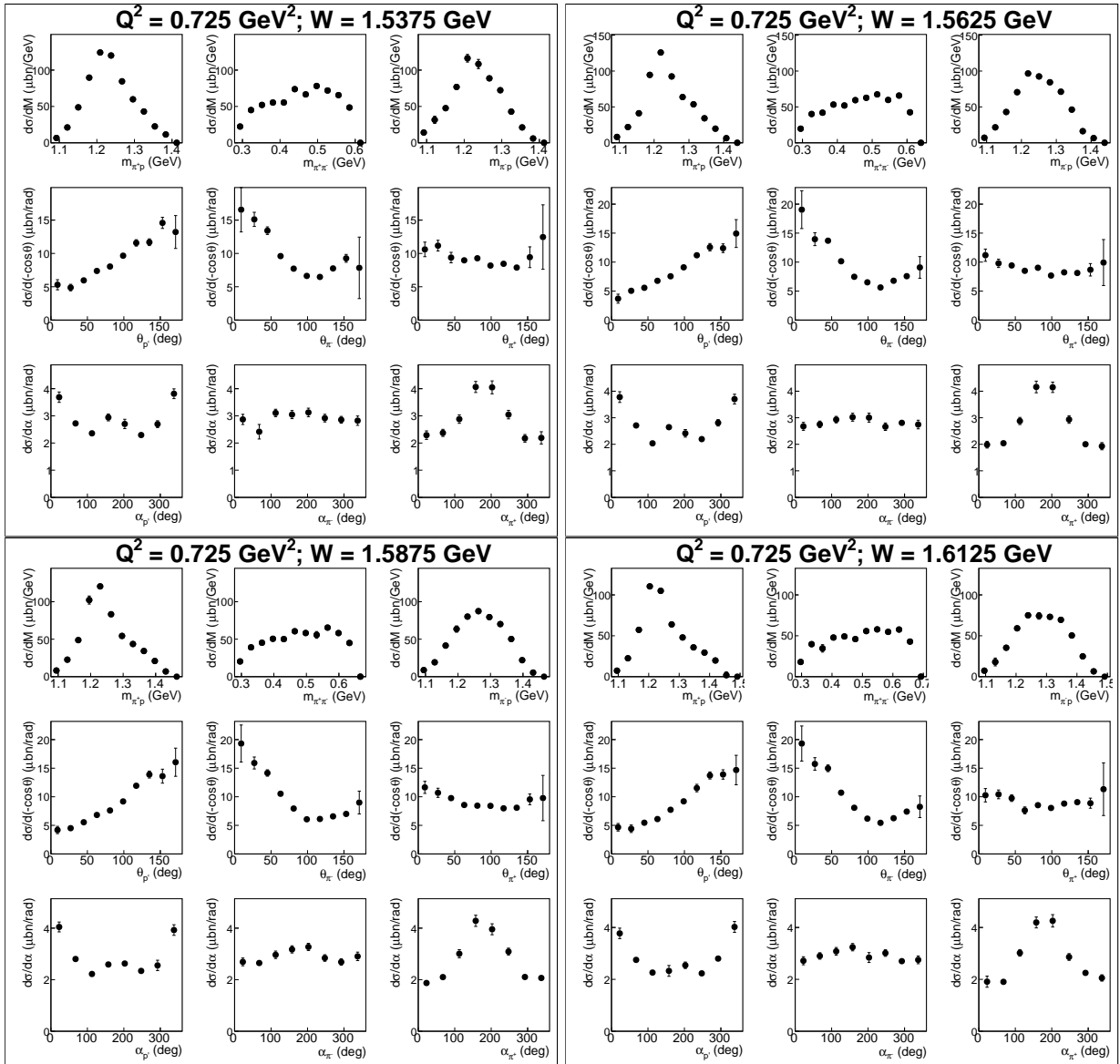


Figure A.30:

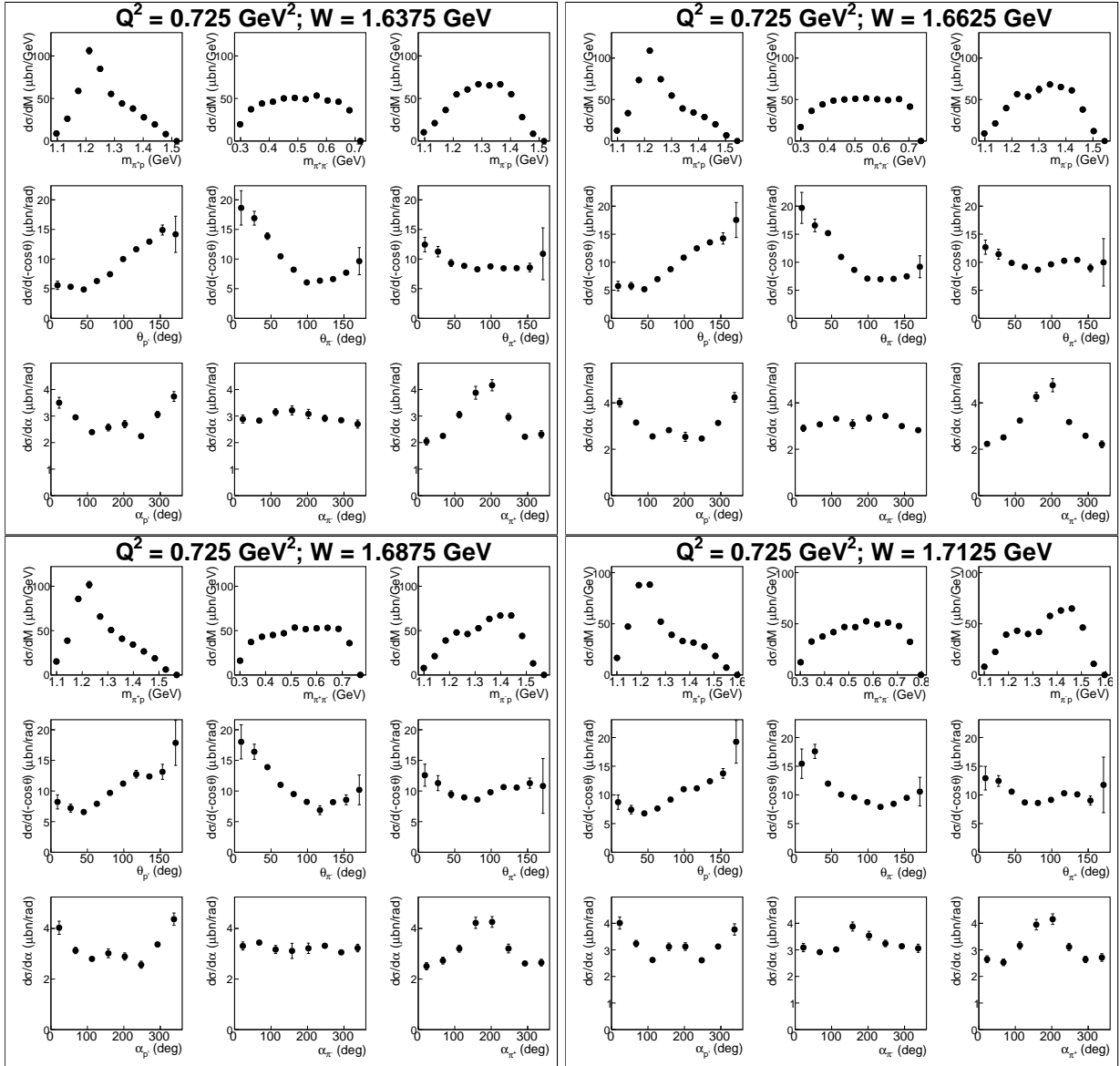


Figure A.31:

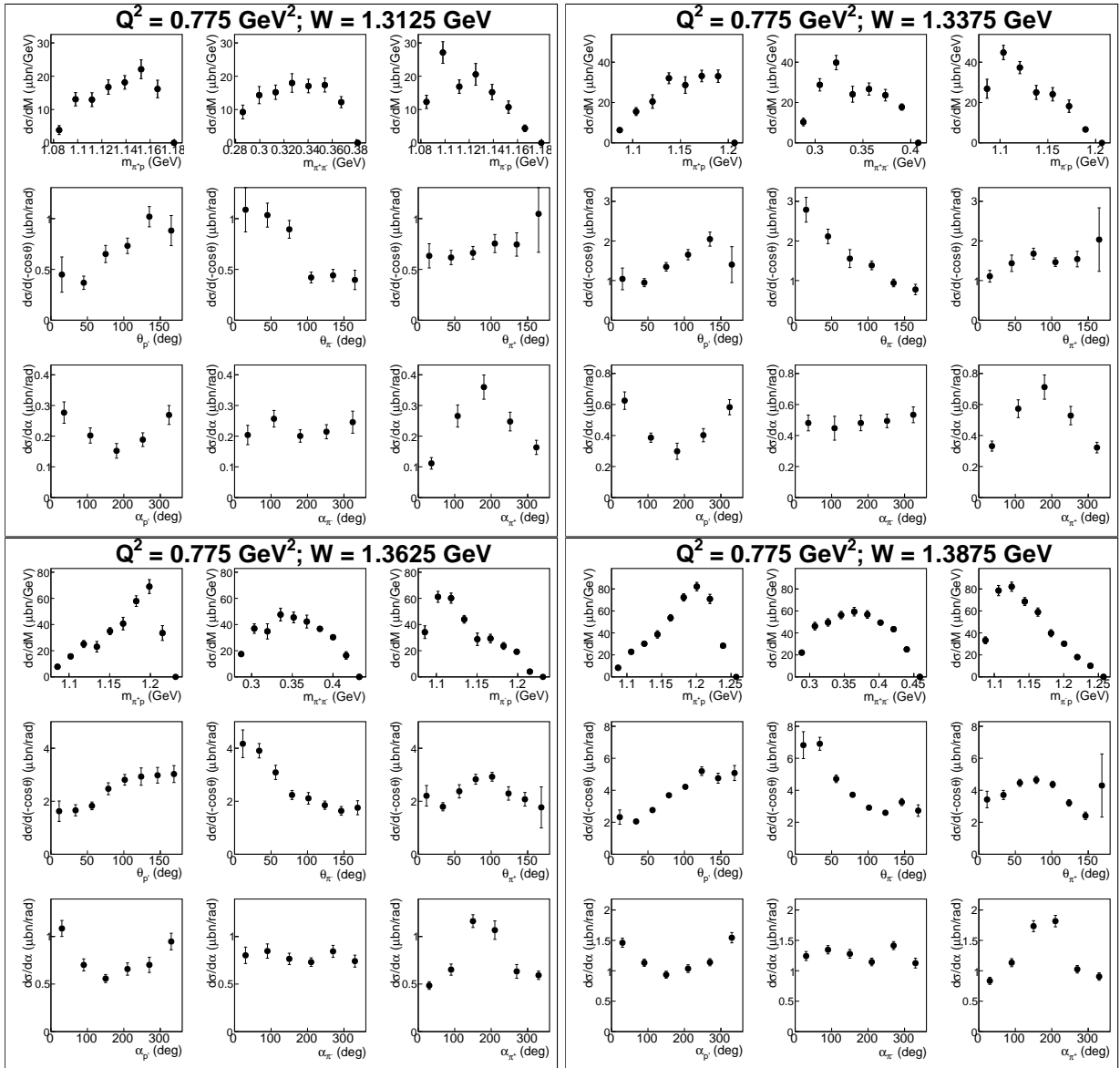


Figure A.32:

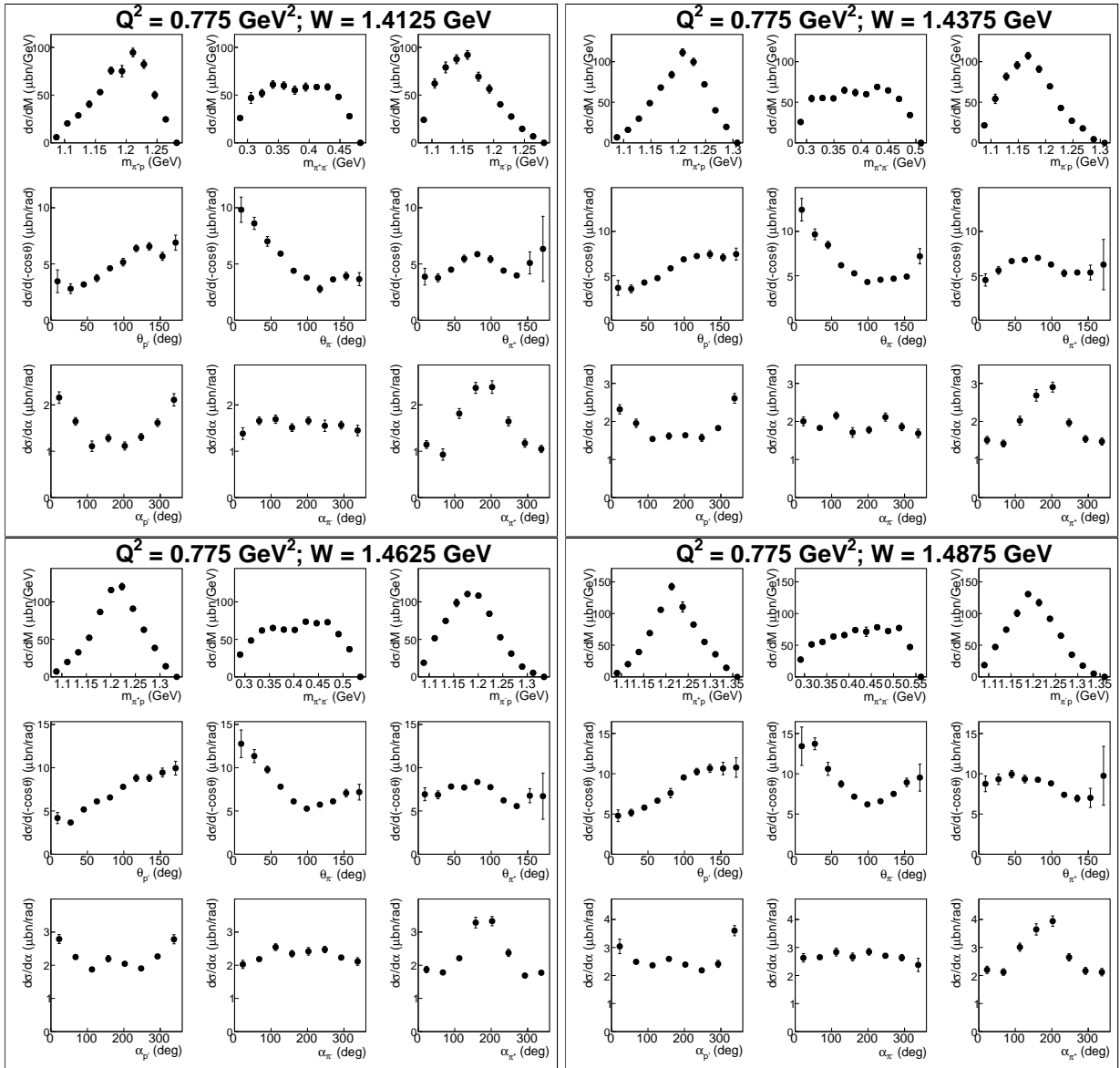


Figure A.33:

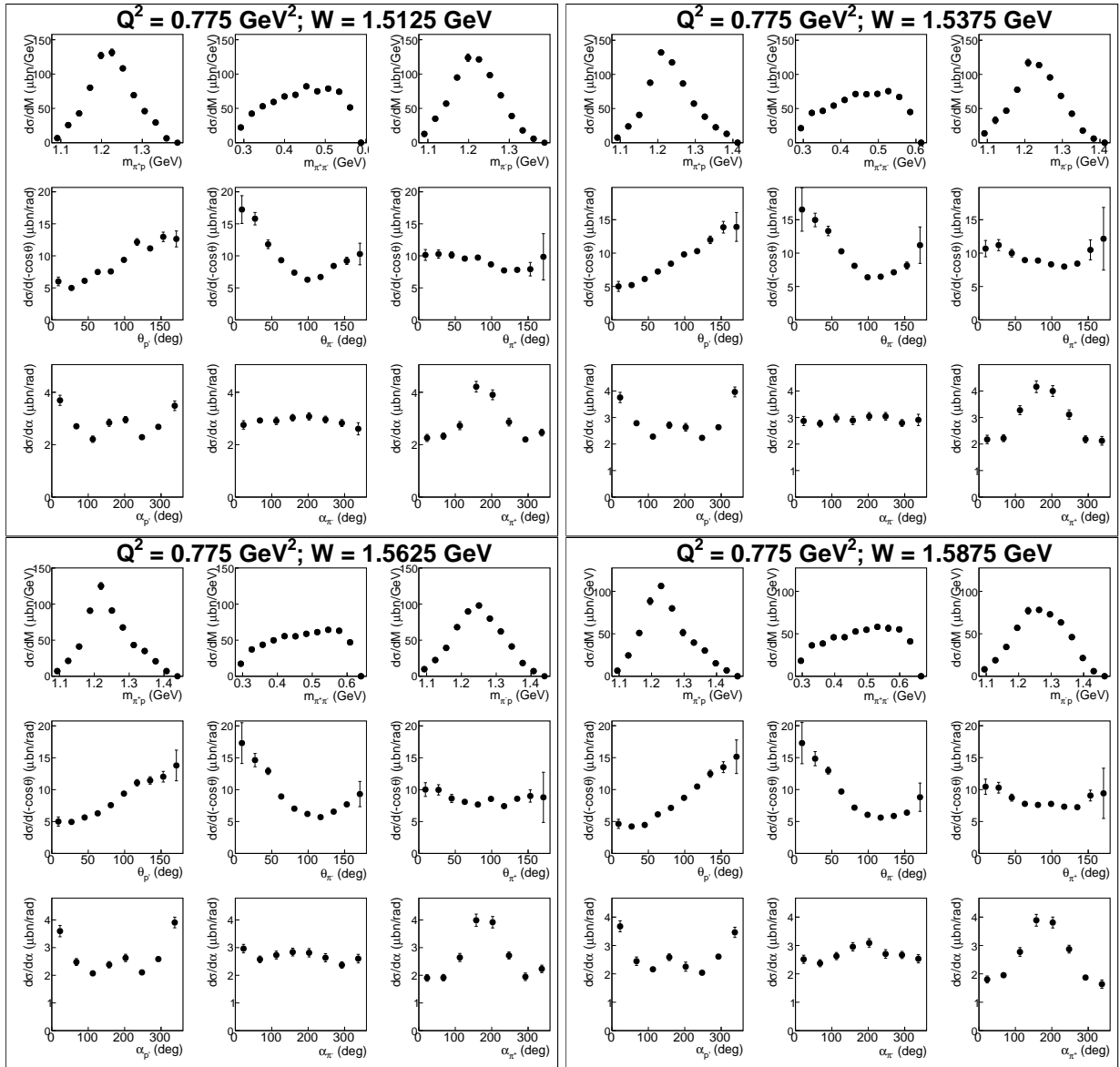


Figure A.34:

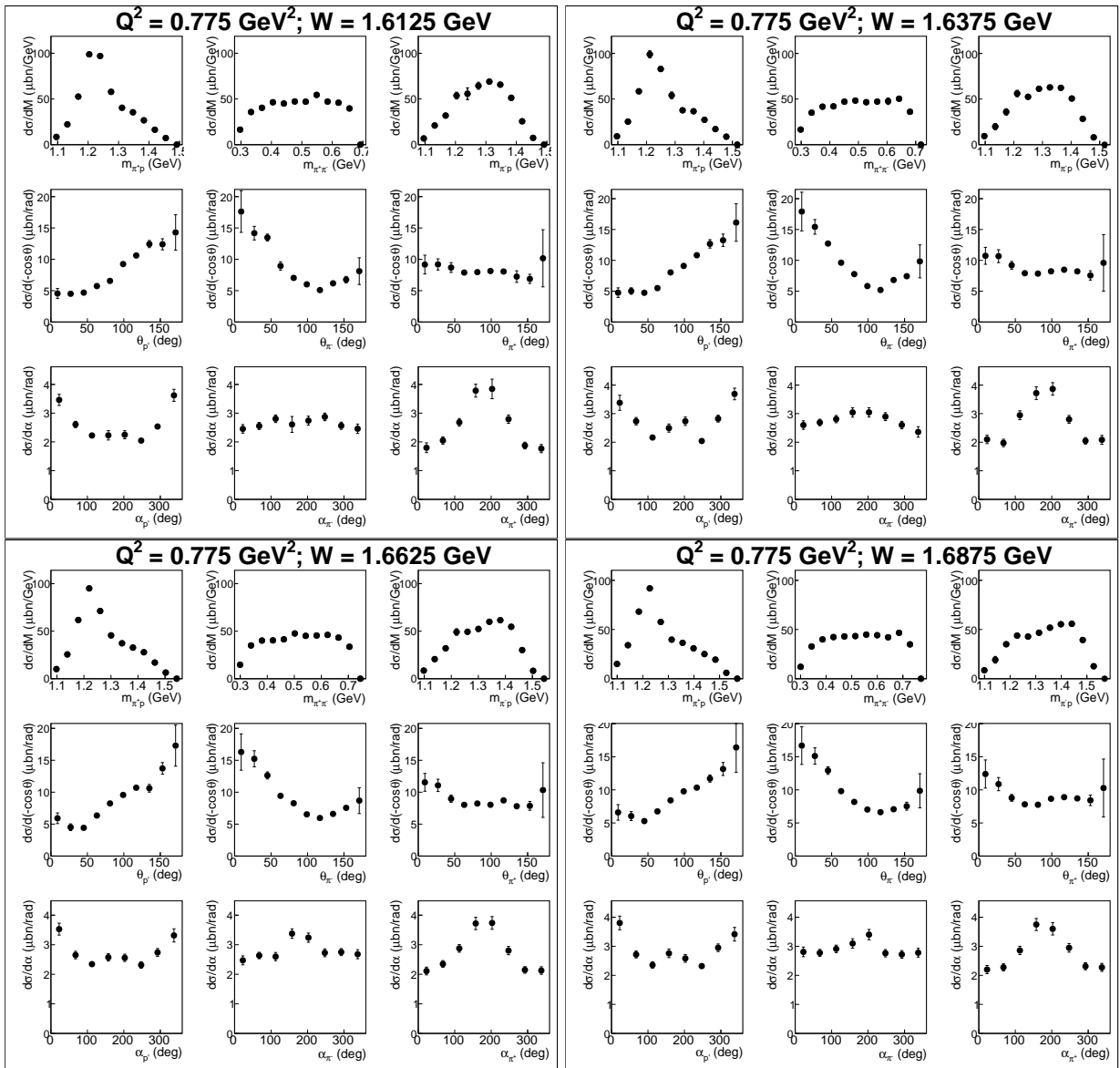


Figure A.35:

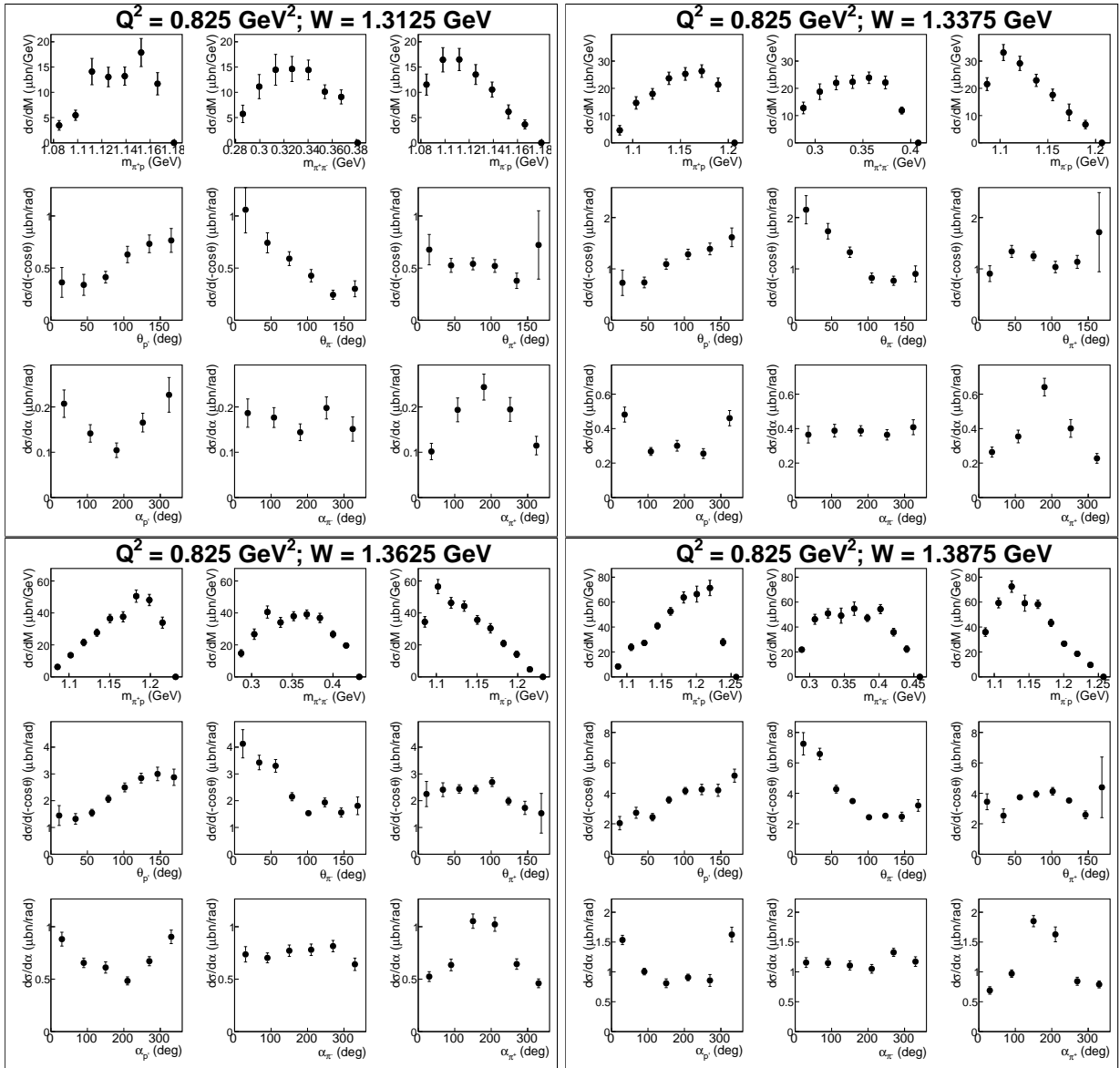


Figure A.36:

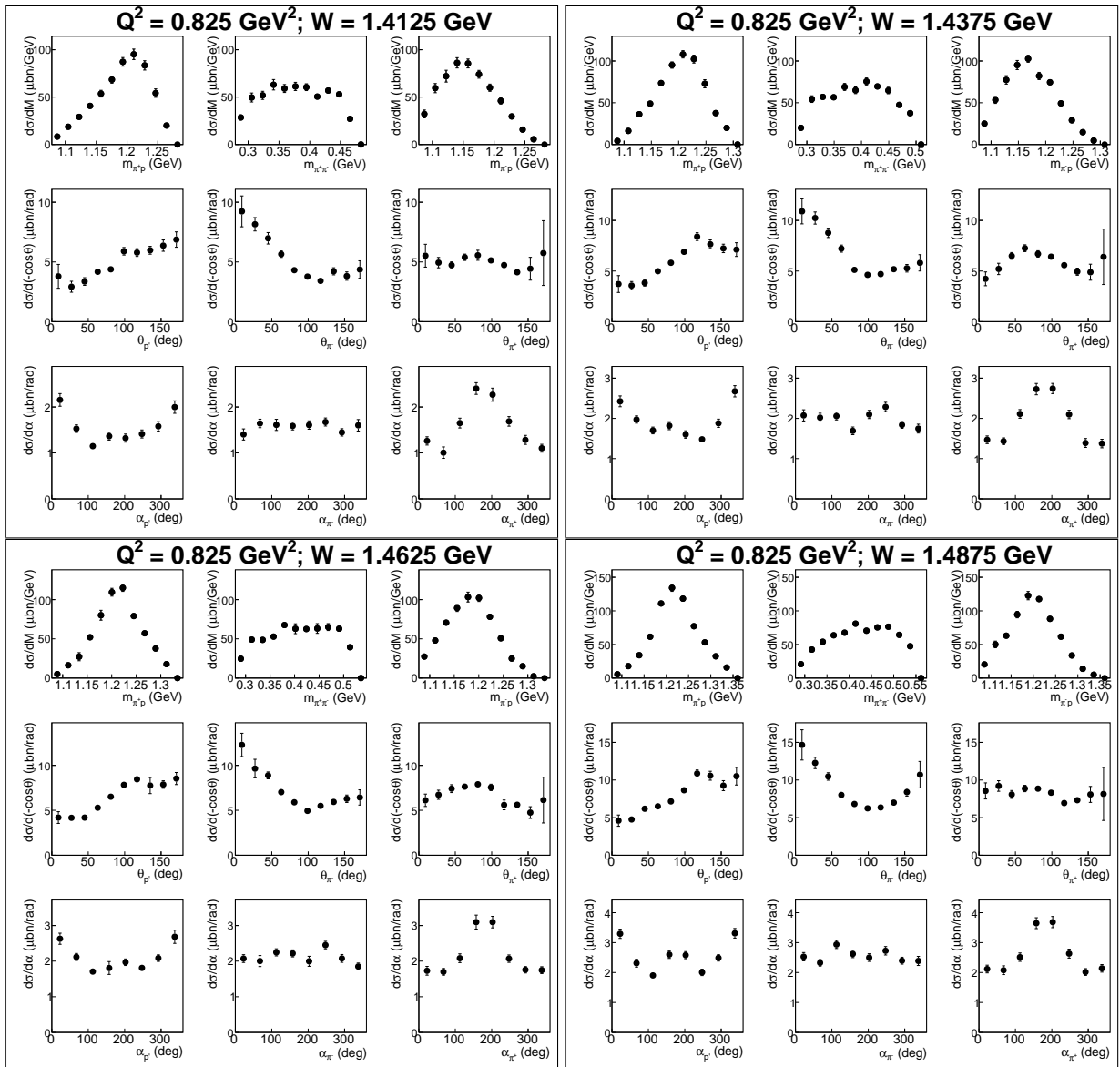


Figure A.37:

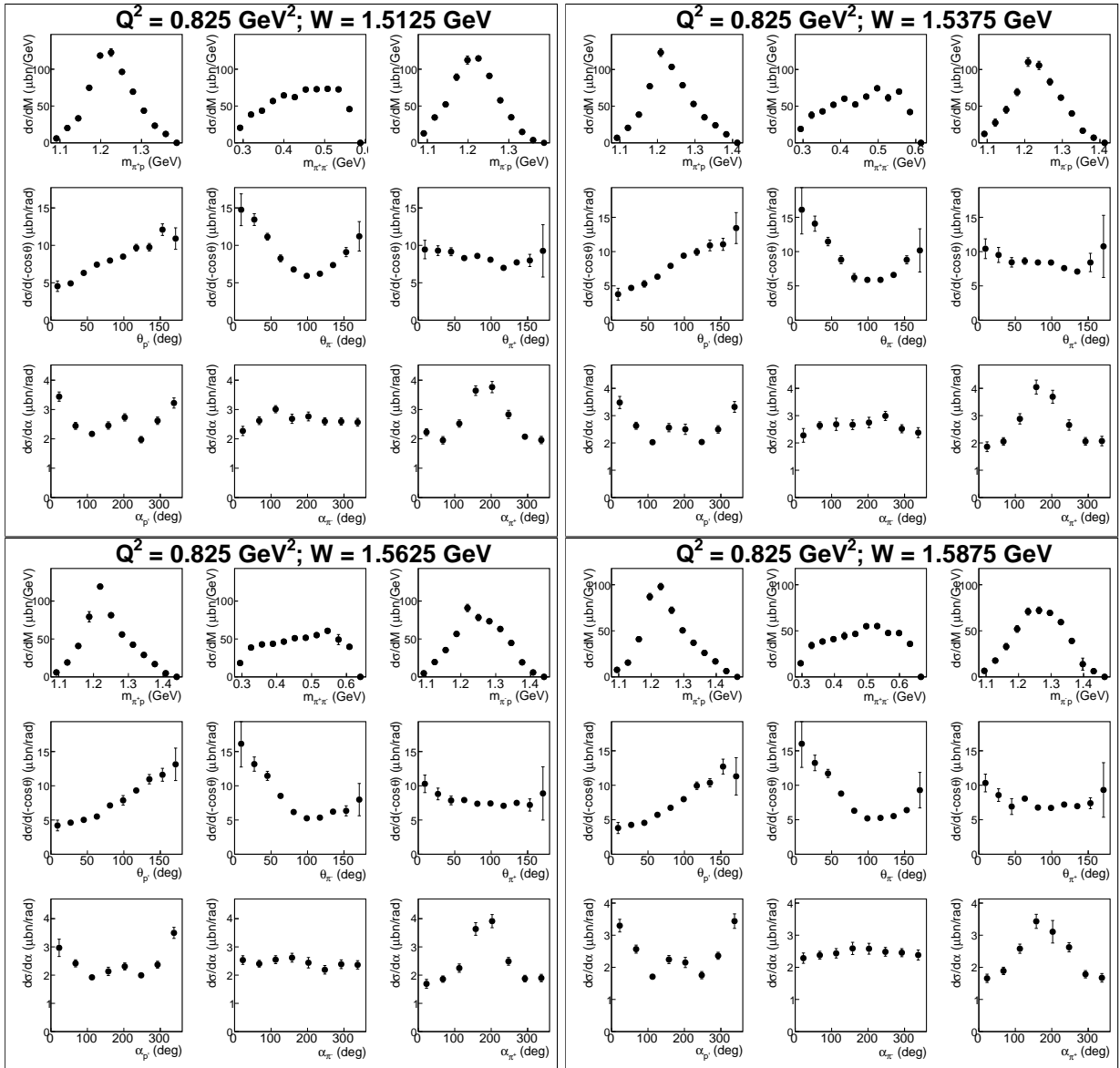


Figure A.38:

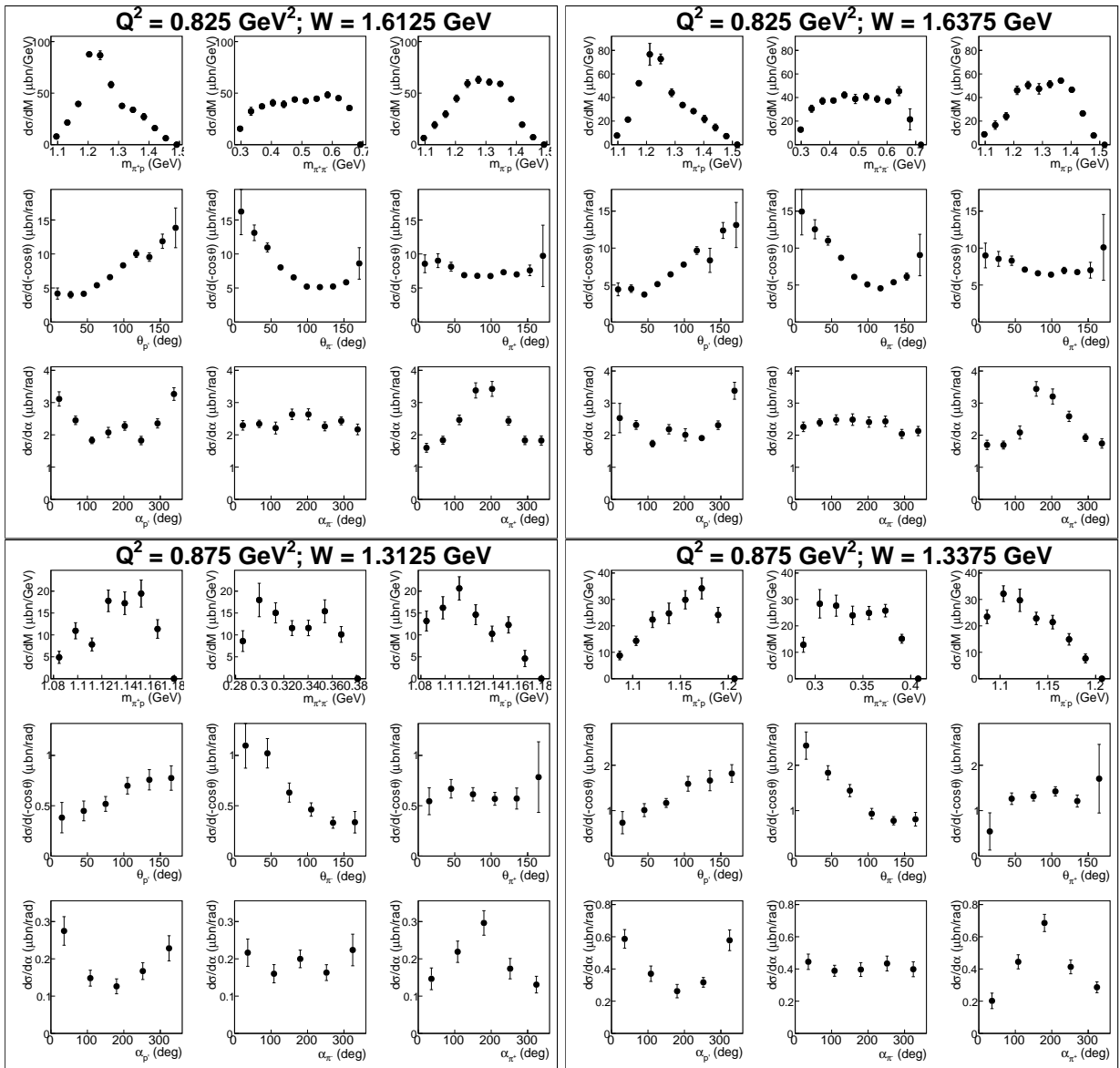


Figure A.39:

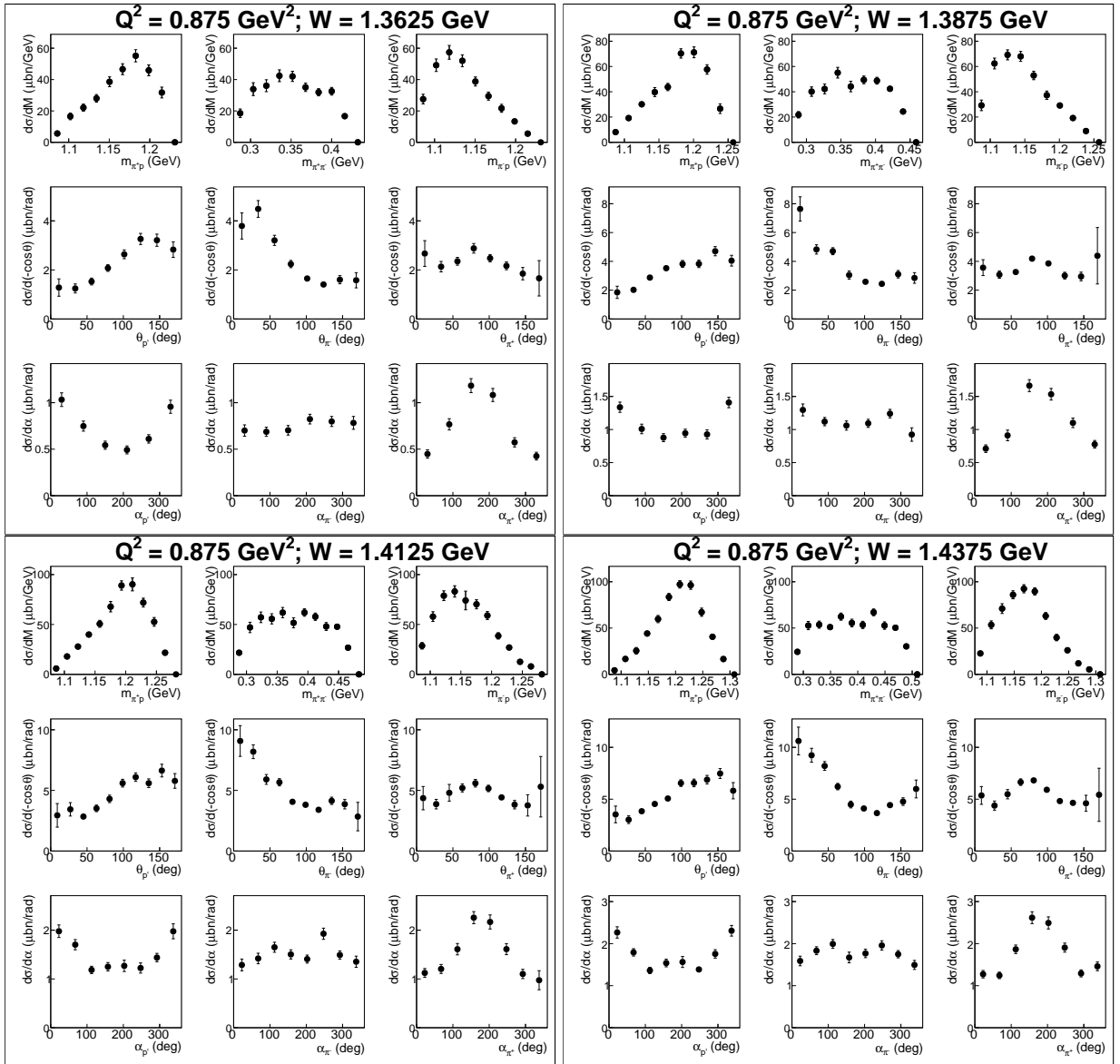


Figure A.40:

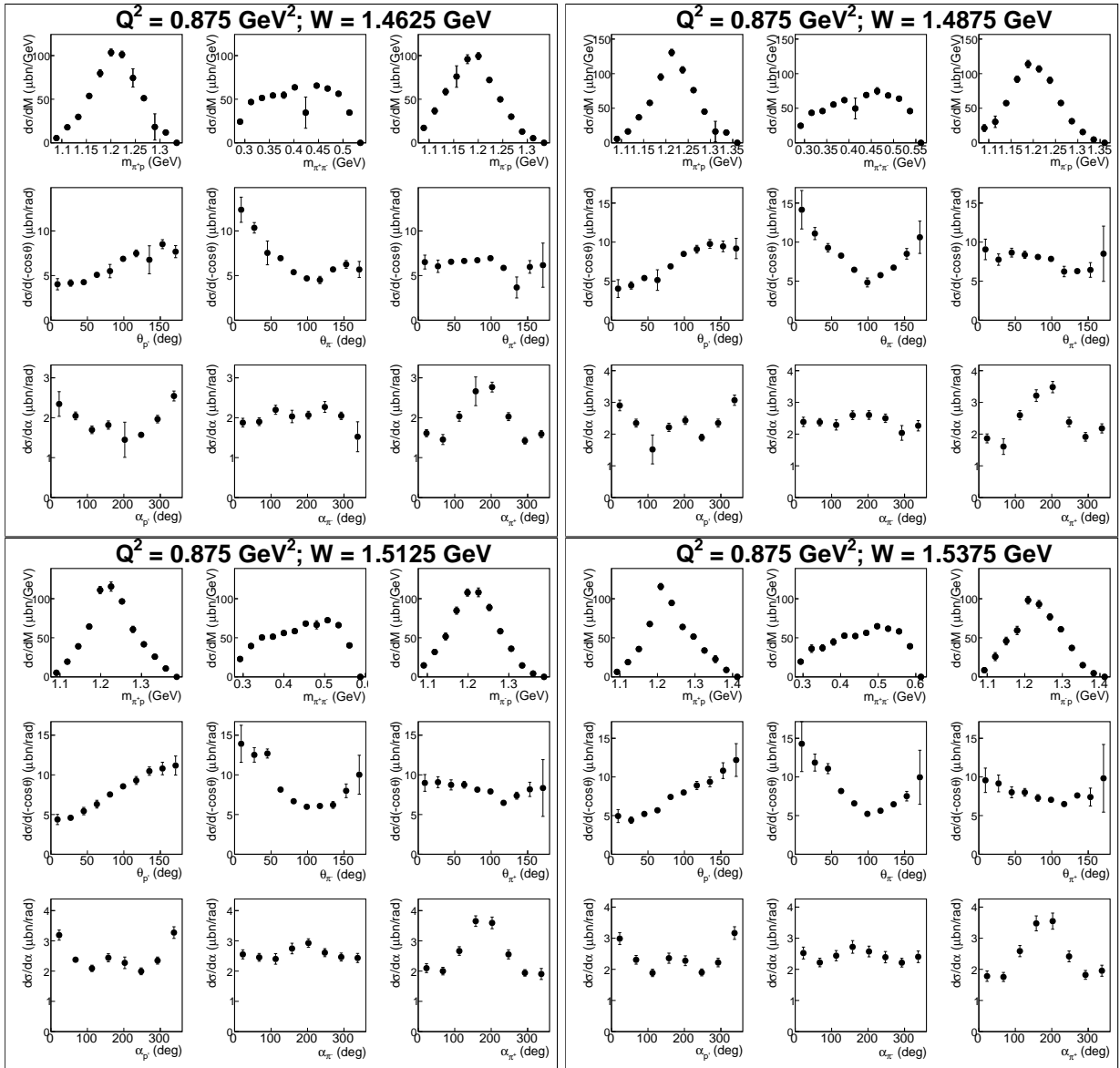


Figure A.41:

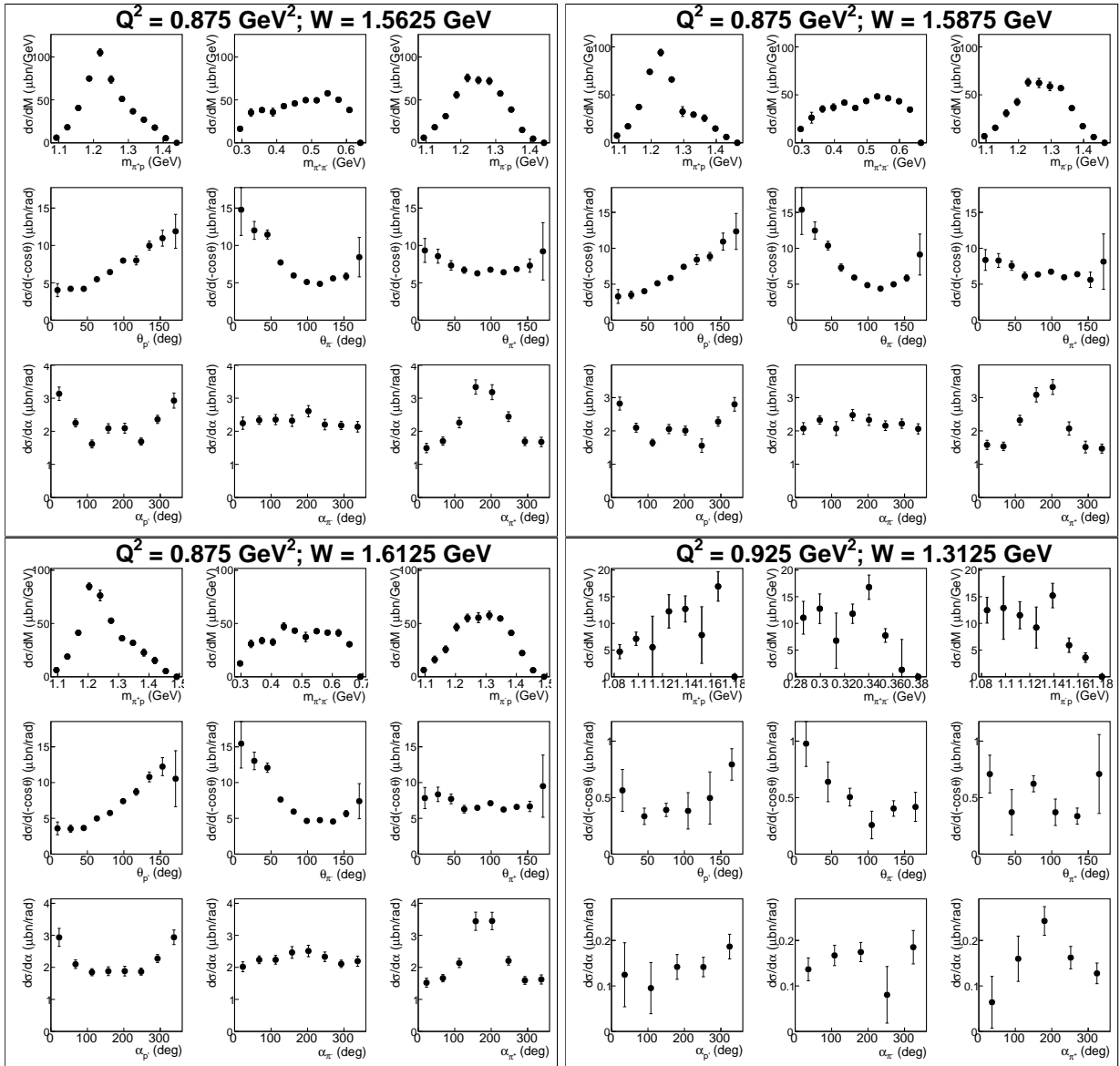


Figure A.42:

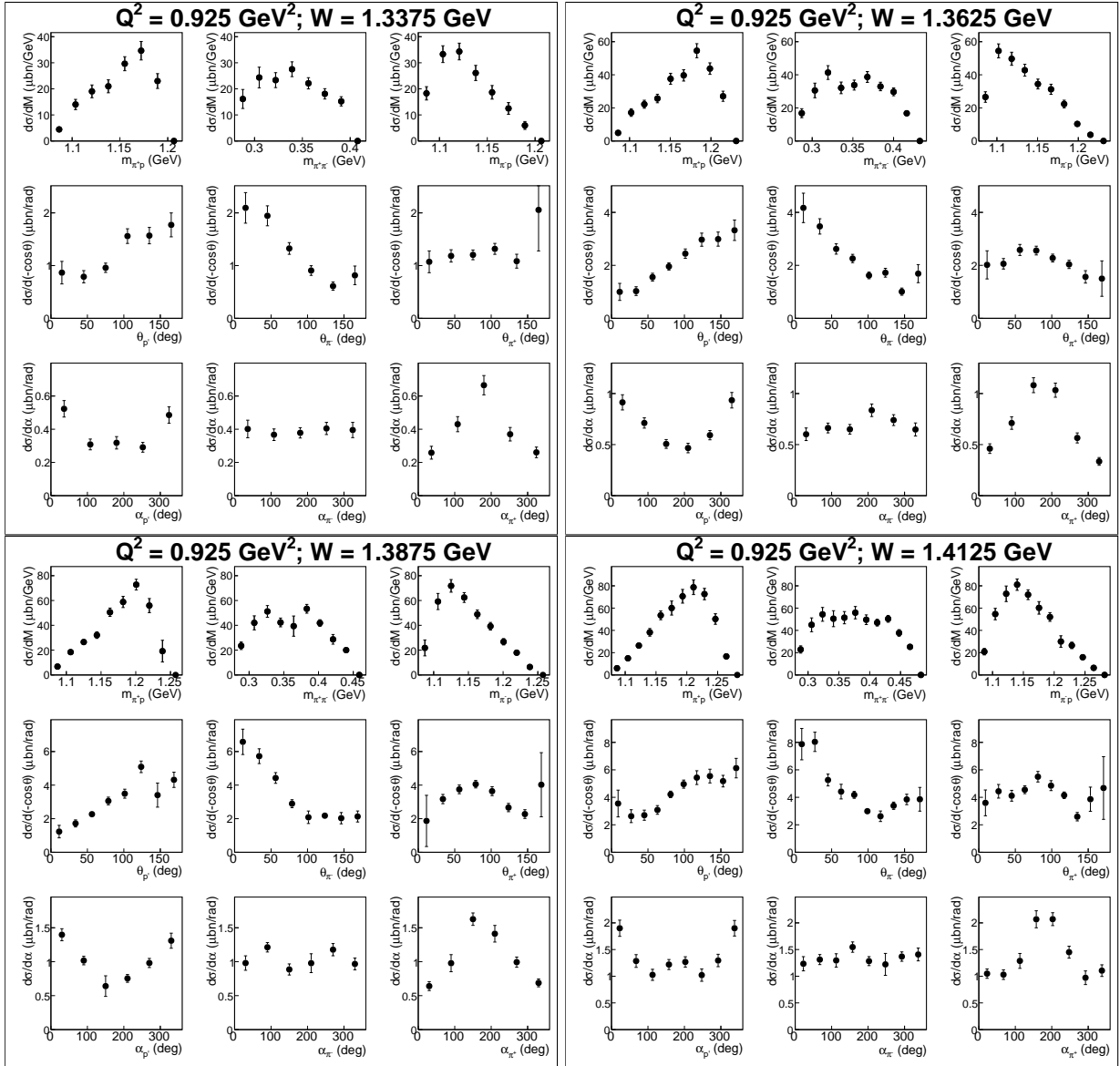


Figure A.43:

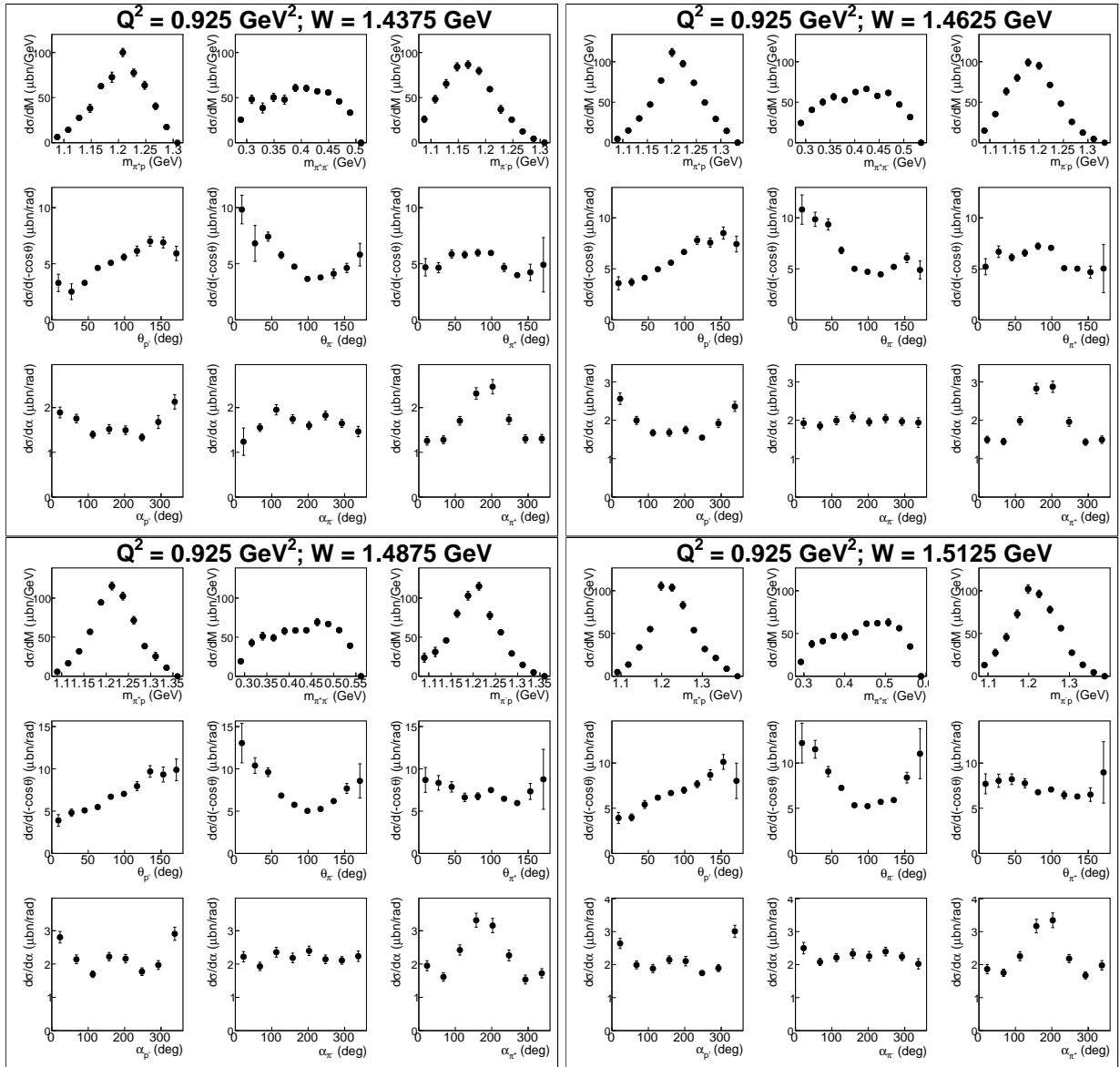


Figure A.44:

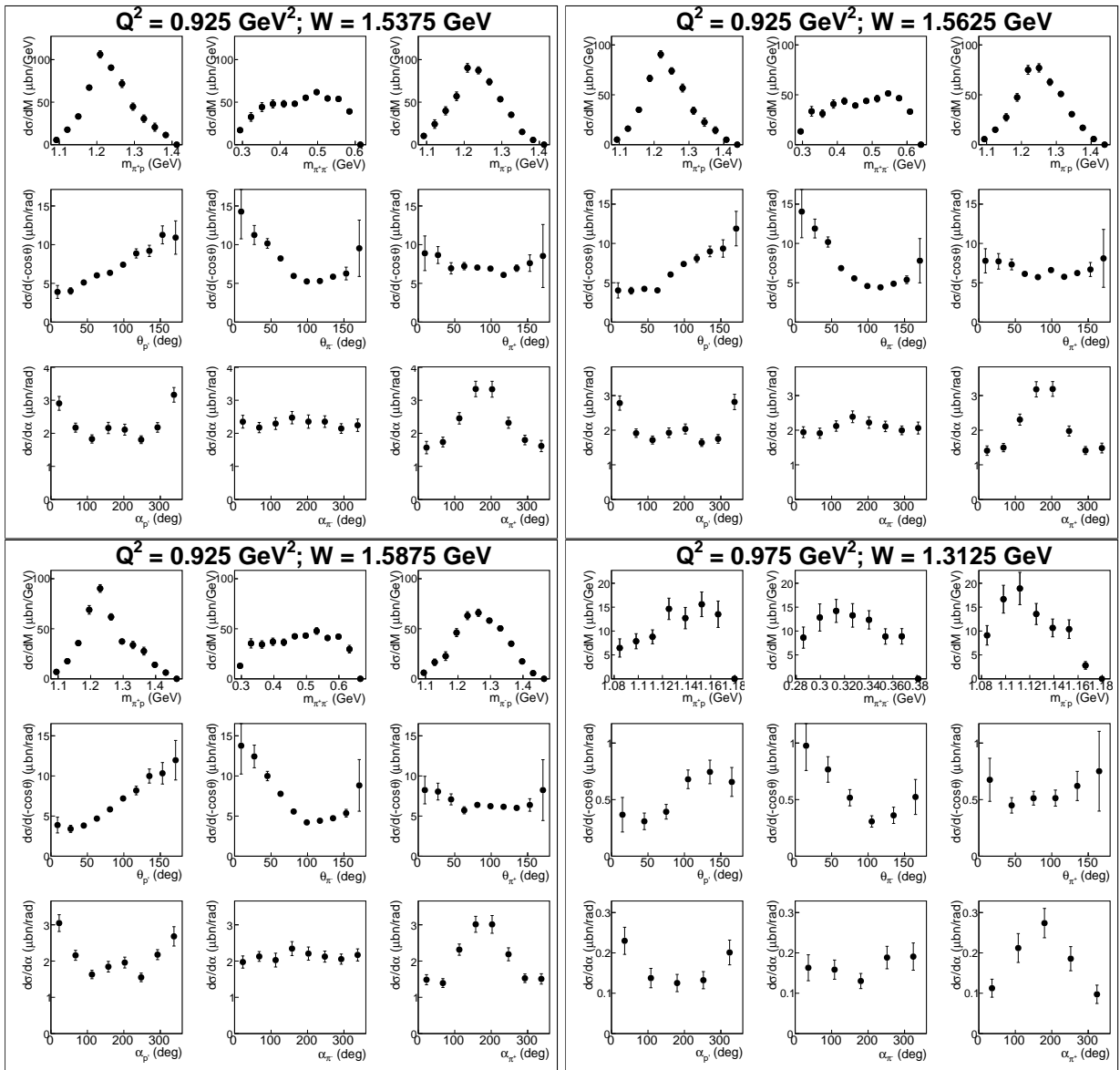


Figure A.45:

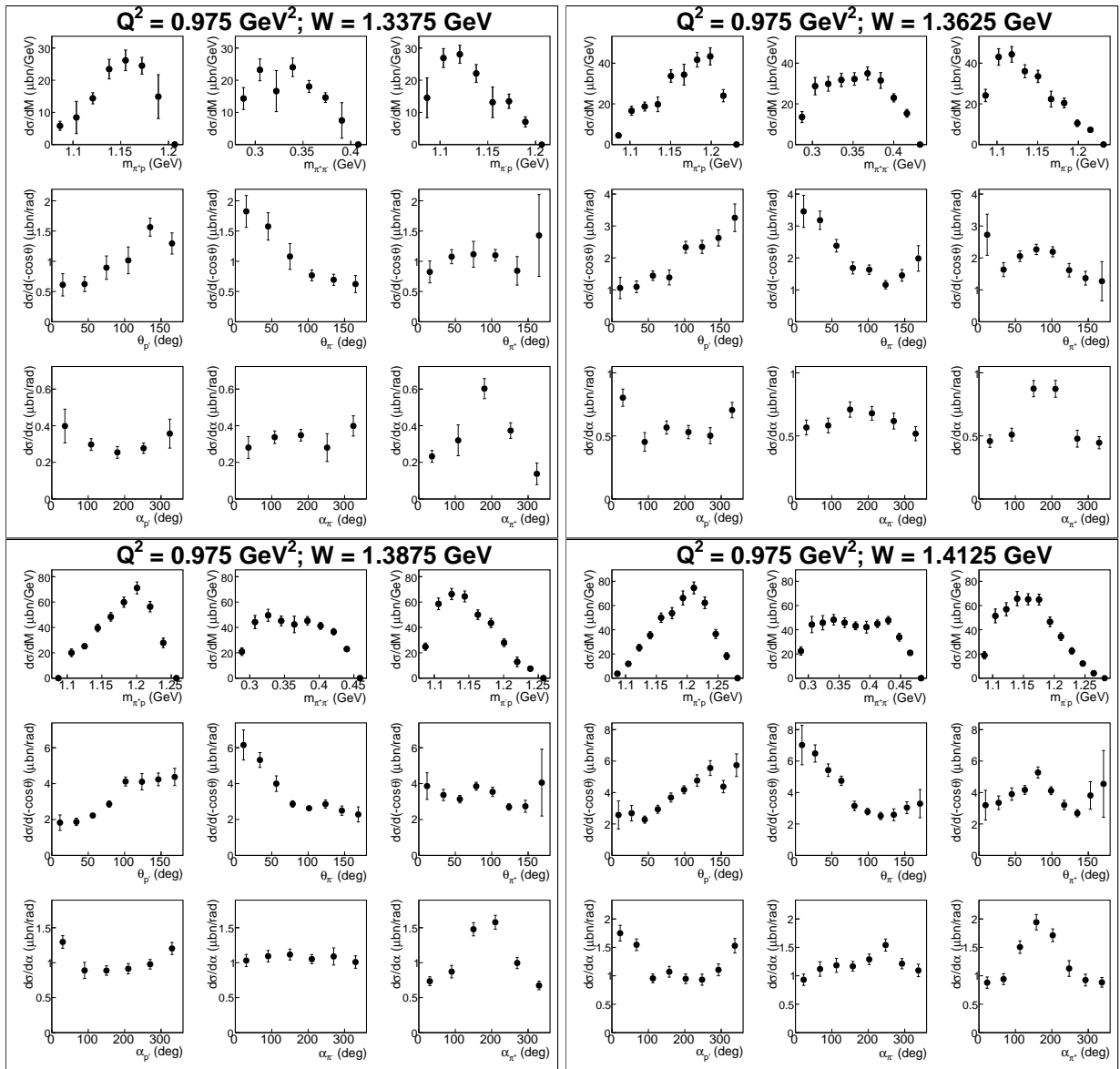


Figure A.46:

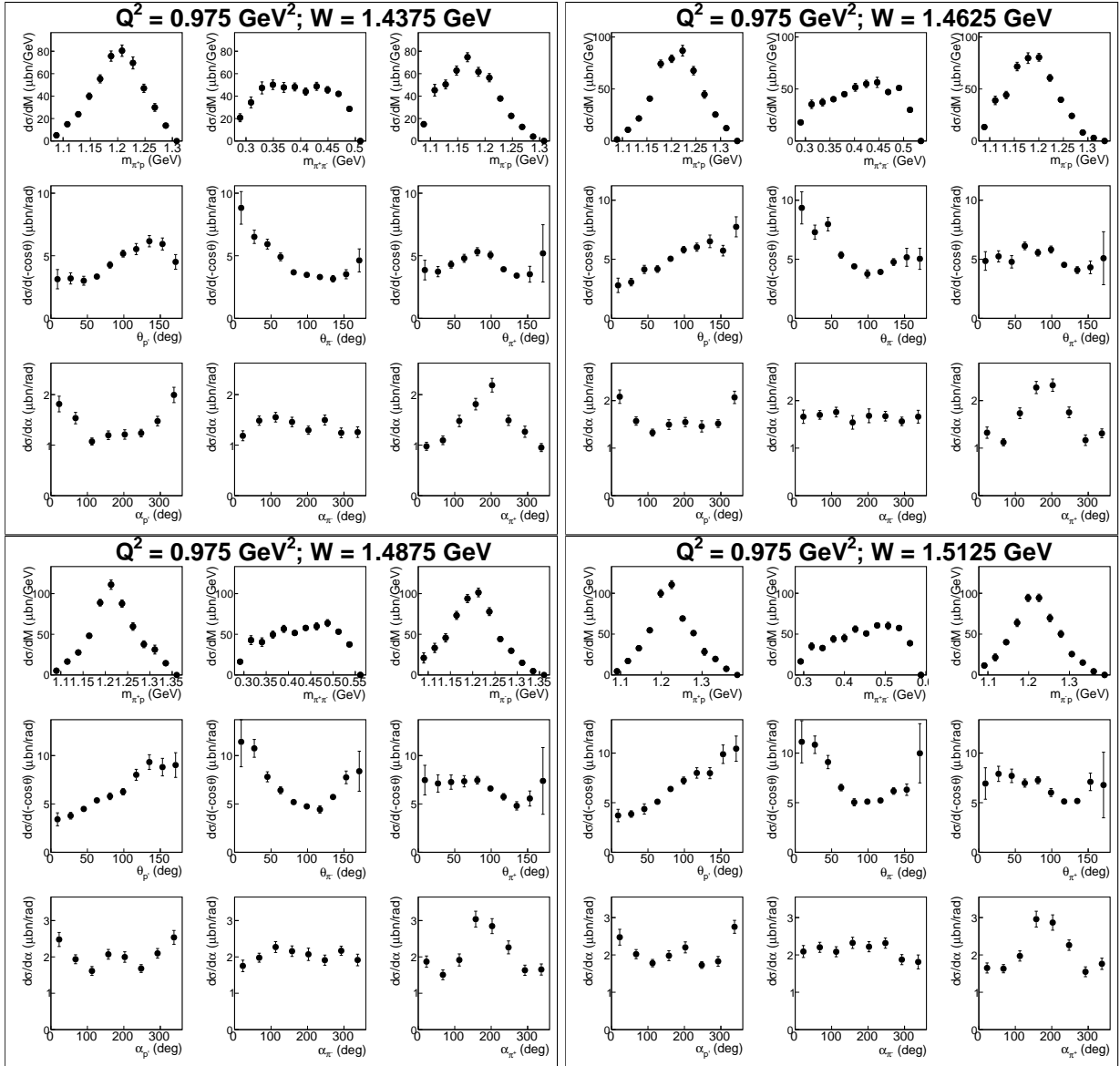


Figure A.47:

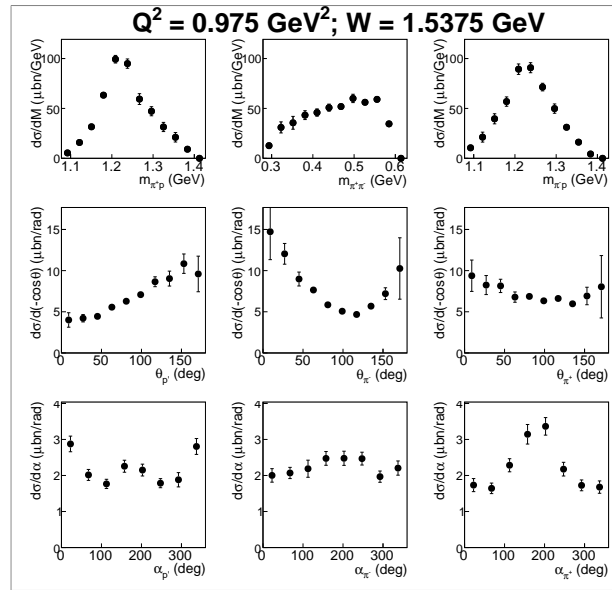


Figure A.48:

Bibliography

- [1] M. Ripani *et al.*, “Measurement of $e p \rightarrow e' \pi^+ \pi^-$ and baryon resonance analysis,” *Phys. Rev. Lett.*, vol. 91, p. 022002, 2003.
- [2] I. G. Aznauryan and V. D. Burkert, “Electroexcitation of nucleon resonances,” *Prog. Part. Nucl. Phys.*, vol. 67, pp. 1–54, 2012.
- [3] I. Aznauryan, V. D. Burkert, T. S. H. Lee, and V. I. Mokeev, “Results from the N* program at JLab,” *J. Phys. Conf. Ser.*, vol. 299, p. 012008, 2011.
- [4] I. G. Aznauryan *et al.*, “Electroexcitation of nucleon resonances from CLAS data on single pion electroproduction,” *Phys. Rev.*, vol. C80, p. 055203, 2009.
- [5] K. Park *et al.*, “Measurements of $ep \rightarrow e' \pi^+ n$ at $W = 1.6 - 2.0$ GeV and extraction of nucleon resonance electrocouplings at CLAS,” *Phys. Rev.*, vol. C91, p. 045203, 2015.
- [6] G. V. Fedotov *et al.*, “Electroproduction of $p \pi^+ \pi^-$ off protons at $0.2 \leq Q^2 \leq 0.6$ -GeV 2 and $1.3 \leq W \leq 1.57$ -GeV with CLAS,” *Phys. Rev.*, vol. C79, p. 015204, 2009.
- [7] V. I. Mokeev *et al.*, “Experimental Study of the $P_{11}(1440)$ and $D_{13}(1520)$ resonances from CLAS data on $ep \rightarrow e' \pi^+ \pi^- p'$,” *Phys. Rev.*, vol. C86, p. 035203, 2012.
- [8] V. I. Mokeev *et al.*, “New Results from the Studies of the $N(1440)1/2^+$, $N(1520)3/2^-$, and $\Delta(1620)1/2^-$ Resonances in Exclusive $ep \rightarrow e' p' \pi^+ \pi^-$ Electroproduction with the CLAS Detector,” *Phys. Rev.*, vol. C93, no. 2, p. 025206, 2016.

- [9] V. I. Mokeev, V. D. Burkert, T.-S. H. Lee, L. Elouadrhiri, G. V. Fedotov, and B. S. Ishkhanov, “Model Analysis of the p pi+ pi- Electroproduction Reaction on the Proton,” *Phys. Rev.*, vol. C80, p. 045212, 2009.
- [10] V. I. Mokeev and I. G. Aznauryan, “Studies of N^* structure from the CLAS meson electroproduction data,” *Int. J. Mod. Phys. Conf. Ser.*, vol. 26, p. 1460080, 2014.
- [11] I. V. Anikin, V. M. Braun, and N. Offen, “Electroproduction of the $N^*(1535)$ nucleon resonance in QCD,” *Phys. Rev.*, vol. D92, no. 1, p. 014018, 2015.
- [12] V. M. Braun, S. Collins, B. Glie, M. Gckeler, A. Schfer, R. W. Schiel, W. Slodner, A. Sternbeck, and P. Wein, “Light-cone Distribution Amplitudes of the Nucleon and Negative Parity Nucleon Resonances from Lattice QCD,” *Phys. Rev.*, vol. D89, p. 094511, 2014.
- [13] J. Segovia, I. C. Cloet, C. D. Roberts, and S. M. Schmidt, “Nucleon and Δ elastic and transition form factors,” *Few Body Syst.*, vol. 55, pp. 1185–1222, 2014.
- [14] D. Binosi, L. Chang, J. Papavassiliou, and C. D. Roberts, “Bridging a gap between continuum-QCD and ab initio predictions of hadron observables,” *Phys. Lett.*, vol. B742, pp. 183–188, 2015.
- [15] J. Segovia, B. El-Bennich, E. Rojas, I. C. Cloet, C. D. Roberts, S.-S. Xu, and H.-S. Zong, “Completing the picture of the Roper resonance,” *Phys. Rev. Lett.*, vol. 115, no. 17, p. 171801, 2015.
- [16] I. C. Cloet, C. D. Roberts, and A. W. Thomas, “Revealing dressed-quarks via the proton’s charge distribution,” *Phys. Rev. Lett.*, vol. 111, p. 101803, 2013.
- [17] I. C. Cloet and C. D. Roberts, “Explanation and Prediction of Observables using Continuum Strong QCD,” *Prog. Part. Nucl. Phys.*, vol. 77, pp. 1–69, 2014.

- [18] B. Julia-Diaz, T. S. H. Lee, A. Matsuyama, T. Sato, and L. C. Smith, “Dynamical coupled-channels effects on pion photoproduction,” *Phys. Rev.*, vol. C77, p. 045205, 2008.
- [19] E. Santopinto and M. M. Giannini, “Systematic study of longitudinal and transverse helicity amplitudes in the hypercentral constituent quark model,” *Phys. Rev.*, vol. C86, p. 065202, 2012.
- [20] I. G. Aznauryan and V. D. Burkert, “Extracting meson-baryon contributions to the electroexcitation of the $N(1675)\frac{5}{2}^-$ nucleon resonance,” *Phys. Rev.*, vol. C92, no. 1, p. 015203, 2015.
- [21] D. S. Carman, “Nucleon Resonance Structure Studies Via Exclusive KY Electroproduction,” 2016.
- [22] V. I. Mokeev, I. Aznauryan, V. Burkert, and R. Gothe, “Recent results on the nucleon resonance spectrum and structure from the CLAS detector,” *EPJ Web Conf.*, vol. 113, p. 01013, 2016.
- [23] <http://clasweb.jlab.org/bos/browsebos.php>.
- [24] K. Egian *et al.*, “Determination of electron energy cut due to the CLAS EC threshoul,” *CLAS-NOTE-99-007*, 1999.
- [25] M. Osipenko, A. Vlassov, and M. Taiuti, “Matching between the electron cndidate track and Cherenkov counter hit,” *CLAS-NOTE-2004-020*, 2004.
- [26] P. K. Khetarpal, “NEAR THRESHOLD NEUTRAL PION ELECTROPRODUCTION AT HIGH MOMENTUM TRANSFERS ,” *Ph. D. Thesis*, 2010.
- [27] K. Park, V. Burkert, L. Elouadrhiri, and W. Kim, “Kinematics Corrections for CLAS,” *CLAS-Note 2003-012*, 2003.

- [28] M. Ripani *et al.*, “A Phenomenological description of $\pi^- \Delta^{++}$ photoproduction and electroproduction in nucleon resonance region,” *Nucl. Phys.*, vol. A672, pp. 220–248, 2000.
- [29] I. G. Aznauryan, V. D. Burkert, G. V. Fedotov, B. S. Ishkhanov, and V. I. Mokeev, “Electroexcitation of nucleon resonances at $Q^2 = 0.65$ (GeV/c) 2 from a combined analysis of single- and double-pion electroproduction data,” *Phys. Rev.*, vol. C72, p. 045201, 2005.
- [30] V. I. Mokeev, V. D. Burkert, L. Elouadrhiri, A. A. Boluchevsky, G. V. Fedotov, E. L. Isupov, B. S. Ishkhanov, and N. V. Shvedunov, “Phenomenological analysis of the clas data on double charged pion photo and electro-production,” in *Proceedings, 5th International Workshop on Physics of excited nucleons (NSTAR 2005)*, pp. 47–56, 2005.
- [31] L. W. Mo and Y.-S. Tsai, “Radiative Corrections to Elastic and Inelastic e p and mu p Scattering,” *Rev.Mod.Phys.*, vol. 41, pp. 205–235, 1969.
- [32] C. Wu *et al.*, “Photoproduction of ρ^0 mesons and Delta-baryons in the reaction $\gamma p \rightarrow p\pi^+\pi^-$ at energies up to $s^{1/2} = 2.6$ GeV,” *Eur. Phys. J.*, vol. A23, pp. 317–344, 2005.
- [33] I. Skorodumina, G. V. Fedotov, V. D. Burkert, E. Golovach, R. W. Gothe, and V. Mokeev, “TWOPEG: An Event Generator for Charged Double Pion Electroproduction off Proton (<https://misportal.jlab.org/mis/physics/clas12/viewFile.cfm/2017-001.pdf?documentId=36>),” *CLAS12-NOTE-2017-001*, 2017.
- [34] E. Byckling and K. Kajantie, *Particle Kinematics*. Jyvaskyla, Finland: University of Jyvaskyla, 1971.
- [35] B. Laforge and L. Schoeffel, “Elements of statistical methods in high-energy physics analyses,” *Nucl. Instrum. Meth.*, vol. A394, pp. 115–120, 1997.
- [36] *PHENOMENOLOGICAL ANALYSIS OF THE CLAS DATA ON DOUBLE CHARGED PION PHOTO AND ELECTRO-PRODUCTION*, 10-15 Oct 2005 2005.

- [37] “Photoproduction of meson and baryon resonances at energies up to 5.8-GeV,” *Phys. Rev.*, vol. 175, pp. 1669–1696, 1968.
- [38] R. Erbe *et al.*, “Multipion and strange-particle photoproduction on protons at energies up to 5.8-GeV,” *Phys. Rev.*, vol. 188, pp. 2060–2077, 1969.
- [39] N. Markov, “Single π^0 Electroproduction off the Proton in the Resonance region (https://www.jlab.org/Hall-B/general/thesis/Markov_thesis.pdf),” 2012.
- [40] E. Golovach, “Clas g11a experiment. clas analysis note. (under review),”
- [41] E. Isupov, “Double-pion electroproduction from clas e1-6 experiment clas analysis note.,”
- [42] P. E. Bosted, “An Empirical fit to the nucleon electromagnetic form-factors,” *Phys. Rev.*, vol. C51, pp. 409–411, 1995.